

178
122

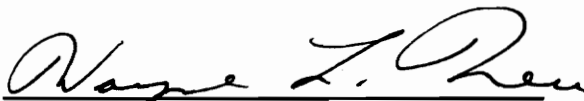
Evaluation of The Dynamic Characteristics of the K-Gill Anemometer

by

CHUNGHWA WEI

Thesis submitted to the Faculty of the
Virginia Polytechnic Institute and State University
in partial fulfillment of the requirements for the degree of
Master of Science
in
Aerospace Engineering

APPROVED:


WAYNE L. NEU, CHAIRMAN


WILLIAM J. DEVENPORT


STERGIOS LIAPIS

MARCH, 1990
Blacksburg, Virginia

c.2

LD

3655

Y85

1990

W45

c.2

Evaluation of the Dynamic Characteristics of the K-Gill Anemometer

by

CHUNGHWA WEI

WAYNE L. NEU, CHAIRMAN

Aerospace Engineering

(ABSTRACT)

The dynamic characteristics of the K-Gill anemometer were evaluated by comparing the anemometer with a hot wire system in a field test, after the static characteristics of the anemometer had been evaluated in a wind tunnel test. The wind tunnel test showed a non-linear and a non-cosine behavior, as shown in previous studies (Ataktürk, 1988; Pond *et al.*, 1979). The turbulence energy spectra from the field test revealed that the propeller anemometer behaves like a single-pole low-pass RC filter, as suggested in previous studies (Ataktürk, 1988; Pond *et al.*, 1979; MacCready and Jex, 1964). The test results showed that mean wind velocity components can be measured with an error of 2%. To determine the Reynolds stress values, uw covariance and friction velocity from different methods were compared. When the stability conditions were unknown, the resulting Reynolds stress estimations have 15% relative differences between different methods.

Acknowledgements

The author would like to express his deep appreciation to his advisor, Dr. Wayne L. Neu who gave invaluable guidance and assistance throughout this study. Without his encouragement, support and guidance, it would have been difficult to accomplish this work.

He also would like to thank Dr. Stergios Liapis and Dr. William J. Devenport for serving on the Advisory Committee and for their helpful comments and suggestions on this study.

He wishes to thank Dr. H.W. Tieleman and Dr. D.A. Walker of Engineering Science Mechanics Department for their help and suggestions.

He also wishes to thank his fellow graduate students who shared their time in many ways.

Finally, a very special thanks are to his parents and his best friend, Chi, for their help and patience during this study.

Table of Contents

Chapter 1. Introduction	1
Chapter 2. Literature review	4
2.1 Atmospheric turbulence	4
2.2 Characteristics of the propeller vane anemometer	6
2.3 Methods proposed for this study	8
Chapter 3. Evaluation of the static characteristics of the K-Gill anemometer	10
3.1 Test facility and instruments	10
3.2 Results and discussion	12
Chapter 4. Evaluation of the dynamic characteristics of the K-Gill anemometer	15
4.1 Apparatus and instrumentation	17
4.1.1 Test set-up and data acquisition system	17
4.1.2 Hot wire jig	18
4.2 Results and discussion	21
4.2.1 Data reduction	21

4.2.2 Spectral analysis	23
4.2.3 Frequency response estimation	25
Chapter 5. Evaluation of the K-Gill anemometer in the measurement of Reynolds stress	30
5.1 Methods of u_w covariance estimation	31
5.2 Results of Reynolds stress estimation	36
5.3 Comparison of the spectra	44
Chapter 6. Conclusions and Recommendations	46
References	48
Appendix A. Calibration of the hot-wire system	51
A1.1 Test facilities and equipments	55
A1.2 Calibration process	56
A1.3 Result	56
Appendix B. Uncertainty analysis of the hot-wire calibration results	58
Appendix C. Dissipation method	61
Figures	64
Tables	120

List of illustrations

- Figure 1. K-Gill propeller vane anemometer (left) and hot-wire jig (right)
- Figure 2. The u spectrum from Kaimal *et al.* , (1972)
- Figure 3. The uw cospectrum from Kaimal *et al.* , (1972)
- Figure 4. The calibration traverse system of the K-Gill anemometer
- Figure 5. The output voltage of the upper propeller anemometer at different speeds and angles
- Figure 6. The output voltage of the lower propeller anemometer at different speeds and angles
- Figure 7. Comparisons of the angular response at different speeds
- Figure 8. The set-up of the field test
- Figure 9. Hot-wire jig coordinate system and probe arrangement
- Figure 10. Comparison of the u components from both hot-wire and K-Gill anemometer when the wind angle was close to 0 degrees

Figure 11. Comparison of the v components from both hot-wire and K-Gill anemometer when the wind angle was close to 0 degrees

Figure 12. Comparison of the w components from both hot-wire and K-Gill anemometer when the wind angle was close to 0 degrees

Figure 13. Comparison of the u components from both hot-wire and K-Gill anemometer when the wind angle was about 30 degrees

Figure 14. Comparison of the v components from both hot-wire and K-Gill anemometer when the wind angle was about 30 degrees

Figure 15. Comparison of the w components from both hot-wire and K-Gill anemometer when the wind angle was about 30 degrees

Figure 16. idealized frequency response of the K-Gill anemometer at different speeds

Figure 17. Comparison of the u spectra from different instruments and the corrected result for data set #1

Figure 18. Comparison of the u spectra from different instruments and the corrected result for data set #2

Figure 19. Comparison of the u spectra from different instruments and the corrected result for data set #3

Figure 20. Comparison of the w spectra from different instruments and the corrected result for data set #1

Figure 21. Comparison of the w spectra from different instruments and the corrected result for data set #2

- Figure 22. Comparison of the w spectra from different instruments and the corrected result for data set #3
- Figure 23. The uw cospectra from both hot-wire and K-Gill anemometers
- Figure 24. Comparison of the uw cospectra from the K-Gill anemometer and the corrected result for data set #1
- Figure 25. Comparison of the uw cospectra from the K-Gill anemometer and the corrected result for data set #2
- Figure 26. Comparison of the uw cospectra from the K-Gill anemometer and the corrected result for data set #3
- Figure 27. The fractional response of the u variance from the K-Gill anemometer at different speeds
- Figure 28. The fractional response of the w variance from the K-Gill anemometer at different speeds
- Figure 29. The fractional response of the uw covariance from the K-Gill anemometer at different speeds
- Figure 30. Comparison of the normalized cospectra at different stability conditions and Kaimal's result for data set #1
- Figure 31. Comparison of the normalized cospectra at different stability conditions and Kaimal's result for data set #2
- Figure 32. Comparison of the normalized cospectra at different stability conditions and Kaimal's result for data set #3
- Figure 33. Comparison of the cospectrum, quad spectrum, magnitude of the cross spectrum, and phase angle for data set #1

- Figure 34. Comparison of the cospectrum, quadspectrum, magnitude of the cross spectrum, and phase angle for data set #2
- Figure 35. Comparison of the cospectrum, quadspectrum, magnitude of the cross spectrum, and phase angle for data set #3
- Figure 36. Comparison of the corrected normalized cospectra at different stability conditions and Kaimal's result for data set #1
- Figure 37. Comparison of the corrected normalized cospectra at different stability conditions and Kaimal's result for data set #2
- Figure 38. Comparison of the corrected normalized cospectra at different stability conditions and Kaimal's result for data set #3
- Figure 39. Comparison of the corrected normalized cospectra at different stability conditions and Kaimal's result for data set #1 with u^* equals 0.0257
- Figure 40. Comparison of the u spectra from measurement and from Kaimal *et al.* (1972) for data set #1
- Figure 41. Comparison of the u spectra from measurement and from Kaimal *et al.* (1972) for data set #2
- Figure 42. Comparison of the u spectra from measurement and from Kaimal *et al.* (1972) for data set #3
- Figure 43. Comparison of the w spectra from measurement and from Kaimal *et al.* (1972) for data set #1
- Figure 44. Comparison of the w spectra from measurement and from Kaimal *et al.* (1972) for data set #2

Figure 45. Comparison of the w spectra from measurement and from Kaimal *et al.* (1972) for data set #3

Figure 46. Comparison of the v spectra from measurement and from Kaimal *et al.* (1972) for data set #1

Figure 47. Comparison of the v spectra from measurement and from Kaimal *et al.* (1972) for data set #2

Figure 48. Comparison of the v spectra from measurement and from Kaimal *et al.* (1972) for data set #3

Figure 49. Comparison of the uw cospectra from measurement and from Kaimal *et al.* (1972) for data set #1

Figure 50. Comparison of the uw cospectra from measurement and from Kaimal *et al.* (1972) for data set #2

Figure 51. Comparison of the uw cospectra from measurement and from Kaimal *et al.* (1972) for data set #3

Figure A1. The calibrations of a hot-wire probe at different temperature

Figure A2. The temperature correction results of different calibration data

Figure A3. The wire coordinate system

Figure A4. Frequency Response of the four pole Bessel low pass filters

List of Tables

Table 1. Error analysis of the K-Gill interpolation Table

Table 2. Calibration accuracy in voltage and velocity components

Table 3. Mean wind vector for different time segments

Table 4. Distance constant for different time segments

Table 5. Estimation of u^2

Table A1. Calibration result of the hot-wire jig

Table A2. Calibration uncertainty in U components

Table A3. Calibration uncertainty in V components

Table A4. Calibration uncertainty in W components

Table A5. Error estimation for the angular offset

List of Symbols

A	hot wire calibration constant
A_0	hot wire calibration constant at 0° C
a	The universal constant defined in Kolmogorov's law
a_k	calibration constant for yaw factor
α	angle of attack
α_j	angle of attack in hot wire jig coordinate system
α_p	angle of attack in probe coordinate system
B	hot wire calibration constant
B_0	hot wire calibration constant at 0° C
b_k	calibration constant for yaw factor
$C(f)$	cospectrum function
$CR(f)$	cross spectrum function
E	output voltage of the hot wire system
e	water vapor pressure

ε_tnon-dimensional temperature difference
 εturbulence dissipation
 ffrequency in Hz
 f_1frequency constant of K-Gill anemometer
 $G(z/L)$ non-dimensional function defined in Kaimal *et.al.* (1972)
 H relative humidity
 $h(f)$frequency response function of the K-Gill anemometer
 $H(f)$ frequency response function of the K-Gill anemometer in energy spectra
 k wave number in the mean wind direction
 k_1 pitch factor
 k_0 yaw factor
 κ The von Karman constant , which equals 0.4.
 LMonin-Obukhov length
 l distance constant
 l_odistance constant at 0 degree angle of attack
 l_adistance constant at some angle of attack
 N non-dimensional frequency
 N_0non-dimensional frequency constant
 n hot wire calibration constant
 p atmospheric pressure in mb
 p_0 reference atmospheric pressure in mb
 ϕ_εnondimensional dissipation

Q corrected wind velocity m/s
 $Q(f)$quadspectrum function
 Q_e effective velocity m/s
 Rfractional response
 R_iRichardson Number
 γ_t rotating angle of the turn table
 γ_jyaw angle in the hot wire jig coordinate system
 γ_pyaw angle in the probe coordinate system
 $S(f)$ energy spectrum
 σ variance
 T_0 temperature at 0° C
 T_gtemperature of the flow
 T_whot wire working temperature
 θ calibration stand angle
 $\theta(f)$phase angle
 θ_pangle between the propeller axis and the wind vector
 τ time constant of K-Gill anemometer
 U wind vector horizontal component in the mean wind direction in
m/s
 V wind vector horizontal component normal to the mean wind
direction in m/s
 W wind vector vertical omponents in m/s
 $U_j V_j W_j$velocity components in the hot wire jig coordinate system in m/s

$U_p V_p W_p$velocity components in the probe coordinate system in m/s

$U_w V_w W_w$velocity components in the wire coordinate system in m/s

$u v w$fluctuation parts of the wind vector in m/s

U_m mean wind velocity in m/s

U_{prp} velocity components along the propeller axis in m/s

u_* friction velocity

t time, second

z height above the surface

SE577E INVALID NUMBER IN EXPRESSION.

OM395I 'VTHFCAP' LINE 360: .se @fig# = A1 + 1

OM397I 'VTHFCAP' WAS IMBEDDED AT LINE 194 OF 'WFIGS'

OM397I 'WFIGS' WAS IMBEDDED AT LINE 42 OF 'WT1'

SE577E INVALID NUMBER IN EXPRESSION.

OM395I 'VTHFCAP' LINE 360: .se @fig# = A2 + 1

OM397I 'VTHFCAP' WAS IMBEDDED AT LINE 198 OF 'WFIGS'

OM397I 'WFIGS' WAS IMBEDDED AT LINE 42 OF 'WT1'

SE577E INVALID NUMBER IN EXPRESSION.

OM395I 'VTHFCAP' LINE 360: .se @fig# = A3 + 1

OM397I 'VTHFCAP' WAS IMBEDDED AT LINE 202 OF 'WFIGS'

OM397I 'WFIGS' WAS IMBEDDED AT LINE 42 OF 'WT1'

SE577E INVALID NUMBER IN EXPRESSION.

OM395I 'VTHFCAP' LINE 360: .se @fig# = A4 + 1

OM397I 'VTHFCAP' WAS IMBEDDED AT LINE 206 OF 'WFIGS'

OM397I 'WFIGS' WAS IMBEDDED AT LINE 42 OF 'WT1'

Chapter 1. Introduction

Turbulent shear stress in the mean wind direction over the sea surface is the major contributor to the wind wave generation mechanism. This Reynolds shear stress ($-\rho\overline{uw}$) may be measured from velocity fluctuations in the surface layer of the planetary boundary layer (PBL).

Several instruments can be used to measure the velocity components in the atmosphere: the sonic anemometer, the hot-wire anemometer, and the propeller anemometer. The sonic anemometer responds quickly to changes in wind velocity. The hot-wire anemometer also responds quickly to changes in wind velocity, but is very fragile. The propeller anemometer responds more slowly to changes in wind velocity, but is robust and requires little or no power to operate.

In the open sea environment, an instrument for Reynolds stress measurement should be rugged enough to operate for a long period of time without maintenance, be very sensitive to wind fluctuations, and have low power

consumption. Considering all these factors, the propeller anemometer is a better choice, because the other two need more power to operate and are easily damaged by the environment.

A K-Gill propeller vane anemometer produced by R. M. Young Co. was investigated in this study. This anemometer was originally developed at the University of British Columbia, and later improved at the University of Washington. A brief description of the development history can be found in Ataktürk (1988).

Fig. 1 is a picture of the K-Gill anemometer (left) and a hot-wire jig (right). The K-Gill anemometer consists of two Gill propeller anemometers [two 22 cm x 30 cm polystyrene propellers (No. 08247)] positioned at angles of ± 45 degrees to the horizontal plane. These are mounted on a 30 cm x 30 cm wind vane, so that they will always be in the wind direction. The output of the upper and lower propeller anemometers are used to estimate the U and W components of the wind vector. The V component is measured by using the wind vane. In this study, U, V, and, W represent velocity components, and u, v, and w stand for the fluctuating parts of the wind velocity.

In measuring the Reynolds stress using the K-Gill anemometer, the slow response characteristic of the propeller anemometer must be considered. Therefore, the objectives of this study were to evaluate the dynamic

characteristics of the K-Gill anemometer and apply this evaluation result to estimate Reynolds stress.

This study is organized in the following order: Chapter 2 is a survey of some characteristics of atmospheric turbulence and previous studies on the propeller anemometer. Chapter 3 is a description of the static calibration of the K-Gill anemometer in a wind tunnel. Chapter 4 is a evaluation of the dynamic characteristics of the K-Gill anemometer in a field test. In Chapter 5, different methods applying the dynamic evaluation results to estimate the Reynolds stress are compared. In Chapter 6, conclusions and recommendations are made.

Chapter 2. Literature review

In order to use the K-Gill anemometer to measure Reynolds stress, the characteristics of the turbulence in planetary boundary layer (PBL) and the characteristics of the propeller vane anemometer must be considered. In this chapter, characteristics of the atmospheric turbulence and those of the propeller vane anemometer from previous studies are reviewed. Methods proposed for the present study are shown at the end of this chapter.

2.1 Atmospheric turbulence

Within the surface layer of PBL, the shear stress varies so little that it is considered a constant. Figs. 2 & 3 show typical normalized energy spectra for the u fluctuation component and uw correlation in the PBL surface layer from the Kansas test (Kaimal *et al.* 1972) . The Kansas test was a

micro-meteorological field experiment on the PBL performed by the Air Force Cambridge Research Laboratory in 1968. Sonic anemometer was used to measure the velocity fluctuations in this test. Regression formulas of the turbulence energy spectra at different stability conditions were established in this test.

The vertical axes in Figs. 2 & 3 are non-dimensional energy spectra and cospectra. The horizontal axes represent non-dimensional frequencies. Spectra for several different stability conditions (z/L) are plotted on each figure.

The meaning of the stability index (z/L) shown in Figs. 2 & 3, is very similar to that of the Richardson number Ri . Under stable conditions, z/L is positive. The heat flux is downward, and the turbulence is damped by temperature stratification. This condition can usually be found in the night time with light wind. For the neutral condition, z/L equals 0, and the turbulence becomes stronger. This condition occurs on cloudy days with strong wind. Negative z/L occurs under unstable conditions. The heat flux is upward; thus heat convection is the major contributor to the turbulence. This condition typically occurs at noon on a sunny day.

Kolmogorov proposed that these spectra can be divided into three portions (see Panofsky and Dutton, 1984). The first is the energy-containing subrange where most of the energy input occurs. The length scales in this range are typically tens of meters to several kilometers, and the time scale varies between

tens of seconds and tens of minutes. The low frequency end of the spectra (Figs. 2 & 3) is in this range. Second, for wave lengths less than the height above surface, but larger than the Kolmogorov microscale, there is the inertial subrange. In this range energy neither enters nor dissipates from the system. The length scale here is in meters and the time scale in seconds. The slope of the spectral curves over this range is constant; this is called $-5/3$ range. The third is the dissipation subrange. Within this range, energy is dissipated, the time scale is in milliseconds, and the length scale is less than the Kolmogorov microscale. In Figs.1 & 2, this range is absent because the frequency is too high. The Kolmogorov microscale is the length scale in which the turbulence dissipation happens and is only a function of molecular viscosity and dissipation (Panofsky and Dutton, 1984).

From Figs. 2 & 3, it is clear that as the non-dimensional frequency increases, all spectral lines collapse to a straight line in the inertial subrange. The greatest differences in energy distribution for various stability conditions happen at low frequencies, which is the energy-containing subrange.

2.2 Characteristics of the propeller vane anemometer

Previous work on the propeller vane anemometer (Ataktürk, 1988; Pond *et al.*, 1979; MacCready and Jex, 1964) has revealed some of its dynamic

characteristics. The dynamic characteristic of the propeller anemometer is analogous to a single pole RC low pass filter with a cutoff frequency that is a function of wind velocity. This function is most easily described in terms of a distance constant, defined as the product of wind speed and the inverse of the cutoff frequency times 2π . Physically, it is the length of air flow causing the propeller to respond to about 70% of a step input (Hicks 1972). Based on the manufacturer's specifications, the distance constant (63% recovery) for the propeller of the K-Gill anemometer is approximately 1 meter. The effective distance constant for non-axial wind increases with the angle of attack (Gill 1975). Since the propellers in the K-Gill anemometer are ± 45 degrees to the horizontal plane, the effective distance constant would be expected to be larger than that in the axial wind conditions. A two-pole system is suggested for the wind vane (MacCready and Jex 1964). This system is characterized by a damping ratio and a natural frequency. The damping ratio is not a function of wind speed, but the natural frequency is a function of wind speed. An undamped wave length is defined as the wind speed divided by the natural frequency and is a constant independent of wind velocity (MacCready and Jex, 1964). Ataktürk (1988) evaluated the characteristics of a wind vane for a similar instrument in a wind tunnel test. He found a damping ratio of 0.4, a natural frequency of 0.92 Hz , an undamped natural wavelength of 7 m, and a delay distance (50% recovery) of 1.4 m.

Two static characteristics of the propeller type anemometer have been shown in previous studies (Ataktürk, 1988; Pond *et al.*, 1979). They are a non-linear

behavior at low wind speed conditions, and a non-cosine behavior when the wind vector has an angle of attack with the propeller axis. Non-cosine behavior here means that the response of the propeller anemometer is not proportional to the component of the wind vector along the propeller axis.

Since measuring the Reynolds stress in mean wind direction ($-\rho\overline{uw}$) was the major concern in this study, measurements were focused on the u and w fluctuations. Therefore, the dynamic characteristics of the propeller anemometer were considered more important than those of the wind vane.

2.3 Methods proposed for this study

In order to evaluate the dynamic characteristics of the K-Gill anemometer and apply this anemometer to measure Reynolds stress following procedure was proposed.

- The first was to evaluate the static characteristics of the K-Gill anemometer in a wind tunnel. This is a prerequisite of the dynamic-characteristics evaluation.
- The second was to evaluate the dynamic characteristics of the propeller anemometer in a field test by using a hot-wire system as a reference, because

the hot-wire anemometer responds much more quickly than the propeller anemometer. Spectra from both instruments' output were compared to estimate the frequency response of the K-Gill anemometer.

- The third was to evaluate the ability of the K-Gill anemometer to measure the Reynolds stress. As in Pond *et al.* (1979), friction velocity from the dissipation method was compared with the measured uw covariance ($-\overline{uw}$). Regression formulas for the energy spectra from the Kansas test (Kaimal *et al.*, 1972) served as a reference for different stability considerations in the Reynolds stress estimation process.

Chapter 3. Evaluation of the static characteristics of the K-Gill anemometer

To evaluate its static characteristics, the K-Gill anemometer was calibrated in a wind tunnel at different velocities and angles of attack.

3.1 Test facility and instruments

The VPI stability wind tunnel was used. This tunnel has a section of 6'x 6'. Turbulence intensity is about 0.03% at low speeds. Fig. 4 is a schematic of the calibration equipment. The K-Gill anemometer was mounted on an angled stand, fixed on a turntable of the wind tunnel. Rotating the turntable placed the anemometer at different angles of attack, the angular relationship between the turntable and the K-Gill being:

$$\sin(\alpha) = \sin(\theta) \sin(\gamma_t) \quad (1)$$

In this equation α is the angle of attack of the K-Gill anemometer, θ is the stand angle with respect to vertical direction (in this case it was set at 30 degrees), and γ_t is the rotation angle of the turntable. As the turntable rotates from 90 degrees to -90 degrees, the angle of attack α changes from 30 to -30 degrees.

The data acquisition system used for this calibration was a *COMPAQ* portable computer and a *Data Translation* DT-2801 12-bit analogue to digital (A/D) converter. The voltage range set for the A/D converter was 0 to 5 volts. The output signal of the propeller anemometer contains a ripple voltage caused by the individual segments of the commutator of the d.c. generator. A 1000 mF capacitor (suggested by the manufacturer of the K-Gill anemometer) was used as a low pass filter to eliminate this oscillation¹. The wind velocity was calculated from the dynamic pressure in the wind tunnel measured by using a Pitot static tube and a electronic manometer. A single hot-wire probe was also used to measure the wind speed. For data acquisition, the sampling rate was 100 Hz, and 500 observations were recorded. The output voltages from the upper and the lower propeller of K-Gill anemometer, the electronic manometer, and the hot wire anemometer were acquired through the A/D converter. The turntable angles were entered from the keyboard of the computer.

¹ This capacitor was not used in the field test.

3.2 Results and discussion

Output voltages of the two propeller anemometers vs. angle of attack of the K-Gill were recorded at different wind velocities. The speeds tested were approximately 0.7, 1.0, 1.5, 2.0, 3.0, 4.0, 6.0, and 10 m/s. The angles of attack at each speed were changed from 30 to -30 degrees. Some results of this calibration are shown in Figs. 5 and 6. The output at speeds below 2.5 m/s is particularly nonlinear. During the calibration it was observed that when the speed was 0.65 m/s, one of the propellers stopped at an angle of attack near 20 degrees, and the other stopped at an angle of attack near -25 degrees. Hence, there is a threshold velocity at about 0.65 m/s, so this wind anemometer cannot be used at low speeds. When the wind speed is higher than about 2.5 m/s, the output of the wind anemometer becomes linear. This characteristic is used to extrapolate the response to higher velocities.

The "cosine law" was used as a reference to evaluate the angular response of the K-Gill anemometer. The "cosine law" states that the propeller responds to the wind component along the propeller axis. Fig. 7 shows the angular response of the upper propeller anemometer. The vertical axis is the ratio of output voltage and axial velocity components, and the horizontal axis is the angle of attack of the K-Gill anemometer. If the cosine law were valid, then the K-Gill response would be horizontal straight lines. The results show the angular response of the

anemometer to be a function of angle of attack of the propeller and wind velocity, especially at speeds less than 1.5 m/s.

A table interpolation method was used to apply these calibration results. Tables of wind anemometer output voltages from both propeller anemometers at different angles of attack and wind speeds were compiled. After inverting these calibration tables, tables that express the wind speeds and angles of attack as functions of the outputs from both upper and lower wind anemometers were obtained. This table interpolation method is more reliable in the low speed range than the angular response function used by Ataktürk (1988), since the latter depends solely on the angle of attack of the propeller anemometer and does not consider the effects of wind velocity.

There are several sources that could have contributed to the uncertainty of this calibration. The uncertainty due to the position of turntable was less than 0.1 degree. This error corresponds to less than 0.1% uncertainty in velocity. This small error is safely neglected. For the wind tunnel velocity sensor, the Pitot static tube, electronic manometer, and hot-wire anemometer could have contributed 1% uncertainty to wind velocity. The uncertainty in the temperature measurement is about $\pm 1^{\circ}\text{C}$, and this would cause an uncertainty of 0.015%, which is negligible. Table 1 shows the error from the table interpolation method. By using the calibration data as input, the table interpolation method was used to find the velocity and angle of attack. Comparing these values with the calibration velocities and angles, the relative error of this table interpolation

method was evaluated. In this table of error analysis, as the speed drops to less than 1 m/s, the error enlarges, especially when close to the threshold velocity. As the angle of attack decreases to ± 15 degrees, a 1% error still can be achieved at this speed range. As the wind speed increases to the linear range of the anemometer, the interpolation error becomes less than 1% for both U and W components. In most conditions the error is less than 0.5%. From the uncertainties of the traverse system, the wind velocity sensor, and the table interpolation method, the total uncertainty in the mean velocity measurement of the K-Gill anemometer is about 2%.

Chapter 4. Evaluation of the dynamic characteristics of the K-Gill anemometer

The K-Gill anemometer was compared to a hot-wire jig (Fig. 1) in the planetary boundary layer in order to evaluate its dynamic characteristics. The test was done by installing both instruments on a tower in an open field. By comparing their outputs in the frequency domain, the frequency response for the K-Gill anemometer was calculated.

In the design of this test, Figs. 2 & 3 were considered in detail. In these figures, the non-dimensional frequency (N) is defined as frequency times measurement height divided by the mean velocity.

$$N = f \frac{z}{U_m} \quad (2)$$

where f is the frequency in Hz, z is the height above surface, and U_m is the mean wind speed. The non-dimensional energy spectrum is the energy spectral value times the frequency f , then normalized by the friction velocity and the non-dimensional dissipation,

$$\frac{fS(f)}{u_*^2 \phi_\epsilon^{2/3}} \quad (2a)$$

and

$$\frac{-fC(f)}{u_*^2 G\left(\frac{z}{L}\right)} \quad (2b)$$

The non-dimensional dissipation ϕ_ϵ and $G(z/L)$ are functions of stability. In these figures, the stability indices (z/L) change from 0 to -2 in the unstable range and from 0 to 2 in the stable range.

In these figures, as the non-dimensional frequency increases, the spectral curve increases to some peak value, than decreasing linearly. The position of this peak moves to high frequencies as the z/L value increases, but the area under the spectral curve decreases. For different stability conditions, the spectral lines collapse to a straight line in the inertial subrange. Most of the differences among the spectral lines occur in the energy-containing subrange. As the non-dimensional frequency approaches one, most of the spectral curves reach the inertial subrange except the curves under very stable conditions ($z/L = 1$ to 2). Therefore, "N equals one" was set as a criterion in the design of the hot-wire jig.

In order to apply this criterion, the field test cannot be conducted under very stable conditions ($z/L = 1$ to 2), such as at night time with light wind.

4.1 Apparatus and instrumentation

4.1.1 Test set-up and data acquisition system

The field test was performed at the Virginia Tech airport in Blacksburg in November 1989. The test site chosen is a small plateau in a gently rolling field with no major obstacle for several miles in the mean wind direction.

Fig. 8 shows the field test set-up. Using several 3/4" and 1" pipes, a 7 m tower was constructed with stands for both the hot-wire jig and the K-Gill wind anemometer. These two instruments were installed 1.4 m apart to prevent interference. Combining the tower height and the plateau height of about 2 m, the total height was approximately 10 m. This 10 m measurement height is frequently used by oceanographers as a standard, and was suggested by Pond *et al.* (1979) as a minimum height for the propeller type anemometer in measuring Reynolds stress.

The data acquisition system used here was the same set used in the calibration of the K-Gill anemometer, except that 1000 mF smoothing capacitor was not

used. A *DANTEC* constant temperature bridge and anemometer units (No. 56C-17) were used for the hot-wires (see Appendix A). Signals from both K-Gill anemometer and hot-wire system were filtered by four pole Bessel low pass filters. A *TEKTRONIX* (No. 5111) oscilloscope was used to monitor the output signals from both wind instruments. In the data acquisition system, six channels were used: three for the hot-wire system output signals and three for the K-Gill anemometers output. Due to constraints in the hardware and software, the sampling frequency was limited to 20.5 Hz; hence the cutoff frequency of the low pass filters was set at 10 Hz to prevent aliasing. A total of three hours of data was collected in one-hour segments.

The effect of the 10 Hz cutoff frequency on the turbulent energy measurement is small. At $f = 10$ Hz, $z = 10$ m, and $U_m = 10$ m/s for example, Figs. 2 & 3 show spectral values one to two orders of magnitude lower than those in the energy-containing range. Therefore, these measurements could be used to find the Reynolds stress with minimal inaccuracy.

4.1.2 Hot wire jig

The hot-wire jig used three single hot-wire probes to measure the three components of wind velocity. The single-wire probes used here are two TSI 1210 normal wire probes and one TSI 1213 inclined wire probe. Fig. 9 shows the arrangement of the probes in the hot-wire jig and the hot-wire jig coordinate

system. The normal wire probes are installed horizontally and at ± 60 degrees to the x axis of the jig coordinate system. The inclined wire probe is aligned with the x axis of the jig coordinate system, with the wire at 45 degrees to the horizontal plane.

The reason for using a hot-wire jig instead of the usual three-wire probe is that the three-wire probe has a limitation in detecting wind vectors at large angle of attack. With three wires positioned in three orthogonal planes, the wind vector can be measured correctly is restricted in a 70 degrees cone (Gaulier, 1977). In atmospheric conditions, the wind direction fluctuates horizontally over a large range. With two wires at ± 60 degrees in horizontal plane, the hot-wire jig can measure the wind vector in a range of almost 120 degrees in horizontal plane.

As shown in Figs. 2 & 3, the spectral value at $N=10$ is one to two orders of magnitude lower than those in the energy-containing subrange. The turbulent eddies corresponding to $N=1$ are more important than those at $N=10$ or higher in this study. The length scale of the eddy at $N=1$ can be estimated from Eq. 2. With the design criterion of "N=1" and a signal frequency of 10 Hz (cutoff frequency of the filter) at 10 m/s wind, the length scale would be around one meter. In the design of the hot-wire jig, the space among the wires was set at about 5 cm. With this arrangement, the highest frequency measurable would be higher than 10 Hz for 10 m/s wind.

The calibration of the hot-wire system was performed in the 3' x 3' subsonic wind tunnel of Virginia Tech, and is shown in Appendix A. In this calibration, the effects of changes in temperature, pressure, and relative humidity were considered, because the field test conditions were different from the calibration conditions. The results of this calibration are not very satisfactory. Table 2 shows relative errors in velocity components and output voltages. These errors were calculated from the relative differences between the measured data and the predicted data from the calibration equations (see Appendix. B). The error of the velocity components is about 10%, but the corresponding error in voltage is only about 1%. An uncertainty analysis is shown in Appendix B. The result of this analysis shows that the uncertainties of the U velocity component become larger than 10% as the wind azimuth angles become larger than ± 30 degrees or at wind speeds around 3 to 5m/s at 0 degrees. For the V component, the uncertainty is around 10% at speeds less than 5 m/s, and at a wind azimuth angle larger than ± 30 degrees. For the W component, the uncertainty is around 20% if the wind azimuth angle is 30 degrees. In the reduction of the field test data some correction should be made when the wind azimuth angle is larger then 30 degrees or at low wind speed range (3 - 5 m/s).

4.2 Results and discussion

By using the calibration results, all voltage data acquired from the field test were transformed into velocity components. From these components, the mean and fluctuating parts of the velocity vector were calculated. Then, the energy spectrum was estimated from these fluctuation components. From the difference between the hot-wire system output spectra and the K-Gill output spectra, the frequency response of the K-Gill anemometer was estimated.

4.2.1 Data reduction

Because of angular differences in the installations, the values of the mean wind vector were not the same for the two instruments. Therefore, the mean wind vector was calculated for each instrument. From the difference in the mean wind vector, the angular difference in the installation was calculated to be about 7 degrees horizontally. Based on the assumption that both instruments encountered the same wind field, coordinate transformations were made. Rotating the x axes of both instruments' coordinate systems to their own mean wind direction, it was assumed that their results were in the same coordinate system. After the mean values were calculated, the fluctuation terms were determined.

Comparisons of the fluctuating velocity components from both instruments when the wind azimuth angle was close to zero are shown in Figs. 10 to 12. It is evident that the K-Gill anemometer responds more slowly than the hot-wire system does, and that the high frequency fluctuation cannot be found in K-Gill signal. The velocity components when the wind azimuth angle was about 30 degrees are shown in Figs. 13 to 15. The u components for both outputs still follow one another, but the w components show some shift between the two signals. The hot-wire system output is shifted 1 to 2 m/s upward. This is a result of calibration inaccuracy of the hot-wire system, since there was some uncertainty of the W components at the azimuth angle around 30 degrees.

Table 3 shows the mean wind vectors derived from each of the one-hour data sets. The mean wind speed of the hot-wire jig is about 10% higher than the K-Gill output. The reason for this difference is that the calibration of the hot-wire system was inaccurate. As mentioned in the uncertainty analysis of the hot-wire calibration, the uncertainty of the velocity components is not small at speeds of 3 to 5 m/s or if the azimuth angle is larger than ± 30 degrees. During the field test the wind direction changed ± 30 degrees in a period of minutes. This variability caused estimation uncertainty in a period of minutes, which means that there would be a low frequency uncertainty in the hot-wire jig output. The other source contributed to this 10% difference in instrument outputs is that the temperature during the test was about 10°C lower than during the calibration. As shown in Appendix A, although the temperature correction

works well, this temperature change could have affected the velocity measured with the hot-wire jig by as much as 2%.

In order to eliminate the low frequency uncertainty from the changing direction of the wind, a one-minute mean value instead of a one-hour mean value was used, and all spectral values were divided by their own mean velocity squared for both instruments' outputs. Since the frequency range of interest in this study was from 0.1 Hz to 2 Hz, the data length used to calculate the mean value was set at 1024 points. This then translates to about 50 seconds at a sampling frequency of 20 Hz. In effect a 0.02 Hz high pass digital filter was applied.

4.2.2 Spectral analysis

In the spectral calculation a Hamming window with a data length of 512 points was applied to the data to minimize side lobe leakage (Marple, 1984) caused by the finite sample length in each segment. With data segments of 1024 points, one hour of data was divided into 75 segments. Mean spectra were estimated by averaging the magnitude of spectra calculated from these data segments. These were then normalized by the mean velocity squared.

Figs. 17 - 26 show comparisons of the spectra from both instruments. The vertical axis is the product of spectral value and frequency, divided by the mean

velocity squared, and the horizontal axis is the frequency. Hence, in the inertial subrange the slope of the spectral curve would be $-2/3$ instead of $-5/3$. However, in the following descriptions it is called the $-5/3$ range.

The u spectra from these two instruments' outputs are shown in Fig.17-19. The spectral curves of the K-Gill anemometer drop faster than do the hot-wire spectral curves. A $-2/3$ slope suggested by the theory is found in those spectra of the hot wire jig output. For data set one, with corresponding mean wind velocity of about 3.5 m/s, the uncorrected K-Gill curve deviates at about 0.07 Hz. For other data sets the K-Gill curves deviates at about 0.2 Hz, mainly because the mean wind speed was around 6.5 m/s, and the frequency response of the K-Gill is a function of speed.

For the w spectra (Figs. 20 to 22), there were some differences at low frequencies, because of uncertainty in the hot-wire jig calibration. Since the correction factor for the w component may not be the same as for the u component, the mean speed normalization technique may not be correct for these w spectra.

From the definition of co-spectrum, the uw cospectrum is the real part of the Fourier transformation of $u w$ cross correlation. This cospectrum is affected by both energy and phase relation of u and w fluctuations. If there is some error in the calculation of either component, the correlation between u and w may be changed. This effect will cause the covariance value (\overline{uw}) to become very small.

The uw cospectra for both instruments are shown in Fig. 23. The hot-wire system spectral curve is lower than the K-Gill output, mainly because the u and w components of the hot-wire system lost their correlation during some time periods, causing the spectral value to become smaller after all the one-minute segments were averaged. Hence, those curves from the hot-wire system were not used to compare with the K-Gill output. The uw spectra for different sets of data are shown in Figs 24 to 26. The slope in the inertial subrange is unclear because the spectral curves become uncertain above 0.3 Hz. There are several reasons for the oscillation. The first is that insufficient data sets have been averaged. The second is the effect of noise in the data acquisition system. Since the spectral value of the uw cospectrum is about one order of magnitude smaller than the u spectrum, the noise to signal ratio is important for the uw cospectrum estimation. The third reason is the effect of the interaction between the dynamic behavior of the propellers and that of the wind vane.

4.2.3 Frequency response estimation

The frequency response estimation of the K-Gill starts from the comparison of the spectral curves of both instruments. Following the method suggested in Horst (1973), the frequency response of a propeller anemometer can be represented as a single pole system. This can be written as:

$$\tau \frac{dU_i}{dt} = U_{prp} - U_i \quad (3)$$

where τ is the time constant for the system, U_i is the indicated wind velocity, and U_{pp} is the wind component sensed by the propeller. The corresponding frequency response can be shown to be:

$$h(f) = [1 + (\frac{f}{f_1})^2]^{-1/2} \quad (4a)$$

For energy spectra, this frequency response would be squared.

$$H(f) = [1 + (\frac{f}{f_1})^2]^{-1} \quad (4b)$$

Here, the constant f_1 is a cutoff frequency (1/2 power point), the relation between the time constant and the frequency constant being

$$\tau = \frac{1}{2\pi f_1} \quad (5)$$

In describing the characteristics of propeller anemometers, it is common to define a distance constant l as

$$l = \tau U_m \quad (6)$$

where U_m is the mean wind speed. The propeller responds in such a way that the frequency response (time constant) is a function of wind speed but the distance constant is not.

By using the least squares method to minimize the difference between the hot-wire spectral curve and the K-Gill spectral curve, and using the spectral values between 0.2 Hz and 1.0 Hz as input data, the value of f_1 was estimated. The distance constant was found by substituting f_1 into Eqs. 5 and 6. Table 4 lists the results for different segments. The distance constant for all three data sets is about 1.34 m. This distance constant is defined for the K-Gill anemometer.

From Ataktürk (1988), there is an angular dependence of $\cos^{-0.5}\theta_p$ (θ_p is the angle of attack of the propeller anemometer) for the distance constant of the propeller anemometer. Considering the geometry of the K-Gill anemometer, in which the propellers are at ± 45 degrees to the x axis of the K-Gill coordinate system, and the axial distance constant of a similar propeller (Catalog No.21281, 23 cm diameter, 1.1 m distance constant) (Ataktürk, 1988), the distance constant for the K-Gill anemometer should be about 1.31 m. This result is similar to the distance constant calculated from the field test.

It is important to note that the definition of the distance constant for the K-Gill anemometer is different from the one defined for the propeller anemometer by Gill (1975) or Brook (1977). The wind component in the axial direction of the propeller anemometer was used to define the angular distance constant. Eq. 6a and 6b below give their definition of the distance constant for non-axial wind.

$$\tau = \frac{l_a}{(U_m \cos \theta_p)} \quad (6a)$$

$$l_a = l_o \cos^{0.5} \theta_p \quad (6b)$$

In this equation l_o is the axial distance constant, l_a is an angular distance constant, and the θ_p is the angle of attack of the propeller anemometer. Comparing Eq. 6a with Eq. 6, we get:

$$l_a = l \cos \theta_p \quad (6c)$$

Applying this relation to Eq. 6b, the relation between the axial distance constant and the non-axial distance constant is found.

$$l = \frac{l_o}{\cos^{0.5} \theta_p} \quad (6d)$$

From this equation, the angular dependence of $\cos^{-0.5} \theta_p$ for the distance constant of the propeller anemometer is shown.

Using the distance constant and Eqs. 4, 5, and 6, the idealized frequency response curve of the K-Gill was calculated. Fig. 16 shows the frequency response curve at different speeds when l is equal to 1.34 m. By dividing the estimated frequency response function (Eq. 4b), the K-Gill output spectra were adjusted. Figs. 17 - 26 also show the results of this frequency response correction. For the u and w spectra (Figs. 17 to 22), the results of this frequency response

correction are satisfactory. The spectral curves in the inertial subrange agree with the hot-wire curves well. For the uw cospectra (Figs. 24 to 26), the effect of this correction is limited, because this correction in the energy-containing subrange is small.

In addition to the estimation of the spectra, the 95% confidence limits for several frequencies in the inertial subrange were calculated. These estimations are based on spectral values of the K-Gill anemometer output corrected for frequency response.

Chapter 5. Evaluation of the K-Gill anemometer in the measurement of Reynolds stress

In the surface layer of PBL, the shear stress is nearly a constant throughout the layer. The shear stress at the boundary is nearly equal to the Reynolds shear stress in this surface layer. Therefore, the friction velocity squared is equal to the Reynolds stress divided by density ρ . That is

$$u_*^2 = -\overline{uw} \quad (7)$$

Hence, the estimation of the uw covariance ($-\overline{uw}$) is the same as that of the friction velocity (u_*^2), and the estimation of Reynolds stress was simplified to $-\overline{uw}$ or u_*^2 in the following analysis, because the density is a constant.

In the evaluation process, the neutral weather condition was first assumed, because the weather conditions were not measured. Using the regression formulas of Kaimal *et al.* (1972), different stability conditions were considered.

An iteration process, which minimized the difference between the measured uw cospectrum and the spectrum from Kaimal *et al.* (1972), was used to estimate the weather conditions and the corresponding $-\overline{uw}$.

5.1 Methods of uw covariance estimation

Several methods were used to evaluate $-\overline{uw}$ or u_*^2 . The first method uses u and w components to calculate $-\overline{uw}$. The second was the dissipation method, which uses the spectral values in the inertial subrange to calculate friction velocity (u_*^2). The third method uses an empirical relation between the standard deviation of the w component and friction velocity.

The most direct method to determine the Reynolds stress is calculated from the covariance of the u and w components. There are two major ways to estimate this covariance. The first uses the measured wind velocity components directly. After the mean values of the velocity components are calculated, the fluctuation parts are used to calculate the variance or covariance. The second way estimates the covariance from the area under the spectral curve of the uw cospectrum.

Because of the effect of the low pass filter behavior of the propeller anemometer, the area under the spectral curve of the K-Gill anemometer is smaller than that given by the hot-wire system. This situation is shown in Figs. 17 to 22, and implies that the variance and the covariance calculated from the

K-Gill output are under-estimated. In order to correct this problem, the ratio of the variances and covariance between the K-Gill output and values from the spectral curve of Kaimal *et al.* (1972) was calculated, and this value was given as the fractional response.

The fractional responses of the variances and the covariance (σ_u , σ_v , σ_w , and \overline{uw}) were estimated at different speeds and different stability conditions. Following a similar procedure used by Horst (1973), and using the spectral formulas from Kaimal *et al.* (1972) for stable air ($z/L > 0$), the fractional responses were calculated. Kaimal's equations are shown below:

$$f \frac{S_a(f)}{\sigma_a^2} = \frac{0.164 \left(\frac{N}{N_0} \right)}{\left[1 + 0.164 \left(\frac{N}{N_0} \right)^{\frac{5}{3}} \right]}$$

$$-f \frac{C_{uw}(f)}{u_*^2} = \frac{0.88 \left(\frac{N}{N_0} \right)}{\left[1 + 1.5 \left(\frac{N}{N_0} \right)^{2.1} \right]} \quad (8)$$

where a stands for u, v , and w , and

$$(N_0)_u = 0.5 Ri$$

$$(N_0)_v = 1.5 Ri$$

$$(N_0)_w = 2.8 Ri$$

$$(N_0)_{uw} = 3.1 Ri$$

Ri is the gradient Richardson number, which represents the ratio of relative importance of convective to mechanical turbulence. The relation between Ri and the stability index z/L for the stable condition can be represented by Eq. (6.7.2) in Panofsky and Dutton (1984):

$$Ri = \frac{\frac{z}{L}}{(1 + 5 \frac{z}{L})} \quad (9)$$

After multiplying the frequency response function of the K-Gill anemometer (Eq. 4b) by Eq. 8, simulated output spectra at different stability conditions were obtained for the K-Gill. By integrating the area under these spectral curves and comparing to the area from the original spectra (Eq. 8), tables of fractional response for the variances and covariance were obtained.

$$R = \frac{\int_0^{\infty} S(f) [1 + (\frac{f}{f_1})^2]^{-1} df}{\int_0^{\infty} S(f) df} \quad (10)$$

In this equation, R is the fractional response. Because f_1 is a function both of the distance constant and of mean wind speed, the table of fractional response also depends on wind speed. In addition, the frequency response correction applies only to the u and w components, since the quantity of interest is the Reynolds

stress in the mean wind direction. The frequency response of the wind vane was not evaluated in this study; therefore the fractional response of the v variance was not evaluated.

The fractional responses calculated for different speeds at various stability conditions are shown in Figs. 27 to 29. For stable air, the value of the fractional response correction curves approaches some fixed value as z/L increases for each speed. Consider Figs. 2 & 3, in which the spectral curves become closer and closer as the stability index z/L increases. A comparison of the amounts required to correct the variance shows that the uw covariance needs the smallest correction, the u variance requires a modest correction, and the w variance needs the largest correction.

These figures are useful when the stability condition (z/L) is known. Dividing the measured $-\overline{uw}$ by the fractional correction factor at the corresponding z/L allows the frequency response corrected value of $-\overline{uw}$ to be estimated.

For unstable conditions, the spectral estimation is more complicated. Boundary layer thickness is required for u spectrum estimation in the formulas suggested by Kaimal (1978) and Højstrup (1981, 1982). Under unstable conditions, there is no equation for the uw cospectrum at energy-containing subrange. Because the difference between the spectral curves of the neutral condition and the unstable conditions in the energy-containing range is small (Figs. 2 & 3), the covariance values from the neutral condition and the unstable

condition are similar (Panofsky and Dutton 1984). Furthermore, the spectral curves for unstable and stable conditions collapse to a line at the inertial subrange, the area under the spectral curve in this range must be the same for both stable and unstable conditions. In the low frequency range, the areas under the unstable and neutral spectral curves are higher than in the stable cases, indicating that the fractional response correction for unstable conditions is closer to 1 than in the stable conditions. Hence, the fractional response for the unstable condition was not evaluated. In following analysis, the fractional response values of the neutral condition were used for unstable conditions.

After the fractional responses had been calculated, the frequency response corrected uw covariance – \overline{uw} could be estimated. In Figs. 24 - 26, the oscillating behavior of the uw cospectra causes uncertainties in area calculations. So the value of the covariance – \overline{uw} was calculated directly from the velocity components with the fractional response correction applied. Due to the under-estimation of the uw cospectrum by the hot-wire system (Fig. 23), the covariance values from the hot-wire system output were not used in this Reynolds stress estimation.

The second method to estimate – \overline{uw} is the dissipation method. This method is based on several assumptions. The major assumption is the equilibrium of turbulence production and dissipation in the inertial subrange. By using spectral values in the inertia subrange of u spectrum, the friction velocity can be estimated. The resulting equation is:

$$u_*^2 = \frac{1}{0.3N^{-2/3}} \frac{fS_u(f)}{\phi_\varepsilon^{2/3}} \quad (11)$$

The derivation of this equation is shown in Appendix C.

The third method uses the data in Table 7.1 in Panofsky and Dutton (1984). This table shows the ratio between the standard deviation of the velocity components and the friction velocity at the neutral condition from different studies. The value of $\frac{\sigma_w}{u_*}$ is almost a constant (1.25) for uniform or rolling terrain. Using σ_w from the measurements and dividing by 1.25, the frictional velocity was calculated as $u_* = 1.25\sigma_w$. This method was used as a reference, since it is only for the neutral condition.

5.2 Results of Reynolds stress estimation

In evaluating the ability of the K-Gill anemometer to measure Reynolds stress, weather conditions are important. For the first set of data, the weather was clear with light wind; the test time was about 4 p.m. The stability conditions ranged from approximately neutral to stable. Weather conditions during the second and the third data sets were windy and cloudy, the time was from 10 to 12 a.m., and stability varied from neutral to unstable.

The u_*^2 or $-\overline{uw}$ estimation process started with the neutral condition assumption of z/L equals 0, since the stability index was an unknown. From this assumption the non-dimensional dissipation ϕ_ε is equal to one.

The results are shown in Table 5a. It is evident that $-\overline{uw}$ or u_*^2 from different methods do not agree, and the values of the measured uw covariance are always lower than the others. One reason is that the data sets have been chopped into one-minute segments; hence fluctuation periods longer than one minute were not considered, and the $-\overline{uw}$ was under-estimated.

Once the stable condition results were compared, the effect of different stability conditions was considered. The equations from Kaimal *et al.* (1972) for the neutral condition were used as a reference, and the stability correction suggested in the same paper was added in these equations.

$$\begin{aligned}\frac{fS_u(f)}{u_*^2\phi_\varepsilon^{2/3}} &= \frac{105f}{(1+33f)^{5/3}} \\ \frac{fS_v(f)}{u_*^2\phi_\varepsilon^{2/3}} &= \frac{17f}{(1+9.5f)^{5/3}} \\ \frac{fS_w(f)}{u_*^2\phi_\varepsilon^{2/3}} &= \frac{2f}{(1+5.3f)^{5/3}} \\ \frac{-fC_{uw}(f)}{u_*^2G(\frac{z}{L})} &= \frac{14f}{(1+9.6f)^{2.4}}\end{aligned}\tag{12}$$

where ϕ_ϵ is non-dimensional dissipation, and $G(z/L)$ is a function of vertical velocity gradient and dissipation. Both ϕ_ϵ and $G(z/L)$ are functions of stability. The empirical formulas for these values in terms of the stability condition are

$$\phi_\epsilon = 1 - \frac{z}{L} \quad (12a)$$

$$G\left(\frac{z}{L}\right) = 1 \quad (12b)$$

for unstable conditions. For stable conditions these equations are

$$\phi_\epsilon = \left(1 + 2.5\left(\frac{z}{L}\right)^{0.6}\right)^{1.5} \quad (12c)$$

$$G\left(\frac{z}{L}\right) = 1 + 7.9 \frac{z}{L} \quad (12d)$$

Under unstable conditions, the $G(z/L)$ value of one (Eq. 12b) indicates that the unstable cospectra will collapse to the neutral condition spectrum. In the estimation of u_*^2 , the dissipation method was also applied to non-neutral conditions. This correction comes from the non-dimensional dissipation (Eqs. 12a and 12c). Based on the value of u_*^2 for the neutral condition, the u_*^2 at different stability conditions was calculated by the division of $\phi_\epsilon^{2/3}$ (Eq. 11). From this value and the corresponding value of z/L , the spectra and cospectra were normalized to the neutral condition level by using Eqs. 2a, 2b, and 12a to 12d. Comparing the left-hand side of Eq. 12 and the vertical axis of Figs. 1 and 2 (Eqs. 2a & 2b) shows that the way to normalize the spectrum and the method used in

the estimation of the u_z^2 are based on the same theory. In Eq. 2a, the spectrum is normalized by u_z^2 and $\phi_\varepsilon^{2/3}$, and the stability-corrected u_z^2 is derived from the division of $\phi_\varepsilon^{2/3}$ (Eq. 11). These give identical normalized spectra for all stability assumptions. The situation is different for the cospectrum. In Eq. 2b, the cospectrum is normalized by u_z^2 and the G function, but the stability-corrected u_z^2 comes from the division of $\phi_\varepsilon^{2/3}$. This procedure causes different normalized spectral values for various stability assumptions.

After a comparison of the cospectrum from Kaimal *et al.* (1972) (Eq. 10) with the normalized cospectrum at different stability conditions, an iteration procedure was used to estimate the value of z/L . The other way to explain this procedure is to find a z/L that causes the normalized cospectrum to agree with the Kaimal neutral condition curve in the inertial subrange.

The reason for using the inertial subrange as a target for the iteration process can be explained by Eq. 12b, in which the G function under the unstable conditions is always equal to one. The spectral curve collapses to the neutral condition curve in the inertial subrange under unstable conditions. In the energy-containing range the spectral curves are different, as shown in Figs. 2 & 3. Therefore, the spectral curve in the inertial subrange is important in the iteration process. Under stable conditions, the situation is different. The spectral curve in the low frequencies is also important, since the cospectra of the stable conditions are well defined in Kaimal's result (Eq. 8). So, the uw cospectrum of Eq. 8 was used instead of that from Eq. 12.

For the first set of data, weather was neutral to stable. The iteration started with Eq. 12b and 12d. For the second and third sets of data, weather was unstable; hence the iteration process started with Eqs. 12a and 12c.

This iteration process uses a minimization technique to find a minimum difference between Kaimal's cospectrum and the normalized cospectrum in the inertial subrange. The oscillating behavior of the uw cospectra required that only a small range of the spectra could be used for this iteration procedure. Hence, the spectral values at the non-dimensional frequency (N), ranging from 0.5 to 2.0, were used in the minimization process.

Estimations of u_*^2 for various z/L assumptions using this method are shown in Table 5b. The reason for using different z/L instead of considering only the minimum difference condition was the oscillating behavior of the uw cospectra, which caused some difficulties in estimating friction velocity. Hence, a $\pm 10\%$ range was used for the friction velocity calculation. Comparisons of Kaimal's results and the normalized cospectra for different stability assumptions are shown in Figs. 30-32. It is difficult to decide which stability assumption agrees better in these figures. Fig. 30 shows the results of the first data set. Since the formula for the stable condition (Eq. 8) was used, the spectral curve of $z/L = 0.03$ is reasonably similar to that of Kaimal's cospectrum. In the unstable cases, the second and the third data sets, the low frequency part of the uw cospectra in the unstable case is higher than that in the neutral case (Figs. 31 to 32). Since Eq. 12 was used, the low frequency part of the normalized cospectra was not focal to

the iteration process; hence the iteration was accomplished in the inertia subrange. A comparison of the dissipation method results in Table 5b with the measured $-\overline{uw}$ and the empirical equation results (Table 5a) indicates that the u_*^2 estimated from the present iteration method may be over-estimated for the first data set, but under-estimated for the second and third data sets. There are several reasons for these results. One is that the dissipation method is based on an assumption of equilibrium between turbulence production and dissipation, but this assumption may not be always correct. The second reason is that the value of the universal constant "a" in the dissipation method (Appendix C.) is not a definite constant. According to Champagne *et al.* (1977), this constant scatters between 0.5 ± 0.05 , which gives a 10% uncertainty for the u_*^2 . The third reason is that the assumption of the constant stress layer may also be wrong, since the terrain is not flat.

Another source of uncertainty in the iteration process is the accuracy of the uw cospectrum. In the cross-spectrum, the cospectrum is the real part and the quadspectrum is the imaginary part. Considering the relationship between the real part and the imaginary part, the following equations are introduced.

$$CR(f) = |CR(f)| e^{-j\theta(f)} \quad (13a)$$

$$|CR(f)| = [C^2(f) + Q^2(f)]^{0.5} \quad (13b)$$

$$\theta(f) = \tan^{-1} \left[\frac{Q(f)}{C(f)} \right] \quad (13c)$$

In these equations, $CR(f)$ is the cross-spectrum, $|CR(f)|$ is the magnitude of the cross-spectrum, $C(f)$ is the cospectrum, $Q(f)$ is the quadspectrum, and θ is the phase angle.

Theoretically, the quadspectrum will not affect the magnitude of the cross correlation when the time delay equals zero (in the present case it is \overline{uw}). Zero is often used in the atmospheric boundary layer as the spectral value of the quadspectrum. Thus there is no phase difference between u and w components. In the present test, for all three data sets none of the quadspectra is zero. Figs. 33 to 35 compare cospectra, quadspectra, and the magnitude of cross-spectra. For all three data sets the cospectrum is approximately twice the quadspectrum at low frequency, a condition which relates to a phase difference of 30 degrees. This phase difference could be caused by the dynamic characteristics of the propeller anemometer. To match the zero phase difference assumption, the cospectrum was replaced by the corresponding magnitude of the cross-spectrum in the following analysis.

The iteration process for the stability index z/L was repeated. Table 5c and Figs. 36 to 38 show the results. Compared to Table 5a, the friction velocity (u_*^2) for the first data set is still too high. Better agreement is found in the other two sets of data.

Compared to the measured $-\overline{uw}$ and the empirical relationship of $\frac{\sigma_w}{u_*}$ for the first set of data in Table 5a, values predicted by the dissipation method

appear over-estimated; therefore the dissipation method appears unsuitable for this case. Because the weather conditions during the first set of data are neutral to stable, the empirical formula $\frac{\sigma_w}{u_*}$ may be applicable in this condition. The z/L estimation results at u_*^2 equals 0.0257 are shown in Table 5c and Fig. 39. Compared with Fig. 36, Fig. 39 shows a better agreement with Kaimal's curves in low frequencies, with the values of z/L ranging from 0.05 to 0.09. As expected these z/L values are close to the neutral condition.

Comparing these u_*^2 estimation results from the dissipation method ² with the measured $-\overline{uw}$, for the first data set the relative difference is 50%; for the second and the third data sets, the relative differences are 15% and 2%. Since the one-minute mean value was used, the value of $-\overline{uw}$ was under-estimated. The relative differences for the second and the third data sets are reasonable. For the first data set, the dissipation method might not be applicable. Comparing the results from the empirical formula ($\frac{\sigma_w}{u_*} = 1.25$) and the measured $-\overline{uw}$, for the first data set, the relative difference is 14%; for the second and the third data sets, the relative differences are 50% and 40%. Since the empirical formula is only used for the neutral conditions and the second and the third data sets are not close to neutral conditions, the 50% and 40% relative differences can be explained.

To sum up, a relative difference of about 15% could be obtained, when an appropriate method was used. An uncertainty of $\pm 10\%$ can be expected in the z/L estimation process when using Kaimal's curves as references. Increased

² These are values corresponding to the minimum difference condition of the z/L estimation process.

accuracy will require longer data segments and a better understanding of stability conditions.

5.3 Comparison of the spectra

In the following analysis, the friction velocities derived in the previous section were used to normalize the spectra. The value of u_*^2 used are the minimum difference value in the z/L estimation process, which are 0.0257, 0.1358, and 0.1432 for three data sets. The ratio of the mean velocities of both instruments were used to adjust the spectra of the hot-wire system to the same level as the spectra derived from K-Gill output.

Figs. 40 to 51 compare these results with spectral curves from Eq. 10. The spectra in these figures are plotted non-dimensionally. The horizontal axis is the non-dimensional frequency (N), defined in Eq. 1. The vertical axis is the non-dimensional spectrum defined in Eq. 1a and 1b. Considering the u spectra in Fig. 40, 41, and 42, the high frequencies closely agree with Kaimal's curve, but there are discrepancies in the low frequencies. As for the unstable conditions, the curves from Eq. 12 are inaccurate in the low frequency range, but in the inertial subrange they must agree with each other, because the dissipation method used this portion to estimate the friction velocity. In these figures, the low frequency

end of the spectral curves decreases quickly, which is caused by the use of one-minute mean value.

The situation is similar for the w spectra (Figs. 43, 44, and 45). The low frequency parts of the spectral curves of the second and third data sets resemble the u spectra case. The measured spectra in the inertial subrange have a slope a little larger than $-5/3$. Both the hot-wire and the K-Gill have similar trends in this range. The reason for this deviation is not clear. The effect of aliasing might have a contribution to this slope. The rolling terrain might also cause this effect, but more sets of data are required to analyze this problem.

The v spectra are plotted from Figs. 46 to 48. Since the frequency response of the wind vane was not estimated in this study, the frequency response correction of the propeller anemometer was used instead. It is clear that the frequency response characteristics of the wind vane are different from those of the propeller anemometers, and an over-shoot behavior of the wind vane occurs at N equals 0.8. As with the w spectra the slope in the inertial subrange is not the same as in the theoretical prediction.

The uw cospectra were replaced by the magnitude of cross spectra (Figs. 49, 50, and 51). Since they were the origin of these analyses, they fit fairly well. But the oscillation of the spectral curves still needs evaluation.

Chapter 6. Conclusions and Recommendations

The static and dynamic characteristics of the K-Gill anemometer were evaluated. Considering the effect of non-linear and non-cosine behavior, the K-Gill anemometer is capable of measuring mean velocity components with an error of 2%. The dynamic characteristic of the propeller anemometer has been shown to be analogous to a single-pole low-pass filter. The distance constant for this single pole system was found to be 1.34 m. With the table of fractional responses and the known stability conditions, the Reynolds stress can be calculated either by the uw covariance or by the friction velocity from the dissipation method. The empirical relation of $\frac{\sigma_w}{u^2}$ can also be used under neutral conditions. The relative difference between u^2 estimations is about 15% when suitable method was used. As the stability was unknown, the z/L estimation process using the Kansas test results as reference showed an uncertainty of $\pm 10\%$. Higher accuracy can be achieved if the stability conditions are known and longer data segments are acquired.

In the future, the oscillation of the uw cospectrum should be evaluated. A longer data set and a better spectral estimation technique are needed. The effect of the quadspectrum and the interaction between the dynamic response of the propeller anemometer and the dynamic response of the wind vane are important subjects to study. If the hot wire jig system is used as a reference, a better wind tunnel and a better traverse system will be required.

References

- Ataktürk, S.S. , 1988. "K-Gill an improved twin propeller-vane anemometer for measurement of atmospheric turbulence," M. S. Thesis, University of Washington, Seattle Washington
- Brook, R.R., 1977. "Effective dynamic response of paired Gill anemometer," *Bound.-Layer Meteor.*, 11,33-37.
- Bruun, H.H., and C. Tropea, 1985 "The calibration of inclined hot wire probes," *J. Phys. E: Sci. Instrum.* Vol. 18, 405-413.
- Champagne, C.A. Friehe, J.C. LaRue, and J.C. Wyngaard, 1977. "Flux measurement, flux estimation techniques, and fine-scale turbulence measurements in the unstable surface over land," *J. Atmos. Sci.* 34,515-530.
- Fabris G., 1978. " Probe and method for simultaneous measurement of "true" instantaneous temperature and three velocity components in turbulent flow," *Rev. Sci. Instrum.* 9(5), 654-664.
- Gaulier, C., 1977. "Measurement of air velocity by means of a triple probe," *DISA Information* April 1977 ,No. 21, 16-20.
- Gill, G.C., 1975. "Development and use of the UVW Anemometer ," *Bound. Layer Meteor.* 8, 475-495.
- Højstrup, Jorgen, 1981 "A simple model for the adjustment of velocity spectra in unstable conditions downstream of an abrupt change in roughness and heat flux," *Bound. Layer Meteorol.* 21, 341-356.

- Højstrup, Jorgen, 1982. "Velocity spectra in the unstable boundary layer" *J. Atmos. Sci.* 39, 2239-2248.
- Hicks, B.B., 1972. "Propeller as sensor of atmospheric turbulence," *Bound. Layer Meteor.* 3, 802-804.
- Horst, T.W., 1973. "Corrections for response errors in a three component-propeller anemometer," *J. Applied Meteor.*, 12, 716-725.
- Jørgensen, F.E., 1971 "Directional sensitivity of wire and fiber-film probes" *DISA Information*, May 1971, 11, 31-37.
- Kaimal, J.C., 1973. "Turbulence spectra, length scales and structure parameters in the stable surface layer," *Bound. Layer Meteor.*, 4, 289-309.
- Kaimal, J.C., J.C. Wingarrd, Y. Izumi, and O.R. Cote, 1972. "Spectral characteristics of surface layer turbulence," *J. Roy. Meteor. Soc.* 98, 563-598.
- Larsen, S.E. and N.E. Busch, 1974. "Hot wire measurement in the atmosphere: part 1 calibration and response characteristics," *DISA Information* July 1974 16, 15-33.
- Larsen, S.E. and N.E. Busch, 1976. "Hot wire measurment in the atmosphere: part 2 A field test on the surface boundary layer," *DISA Information* Sep. 1976 20, 5-21.
- Large, W.G. and S. Pond, 1981. "Open ocean momentum flux in moderate to strong wind," *J. Phys. Oceanogr.* 11, 324-336.
- MacCready, P.B., Jr. and H.R. Jex, 1964. "Response characteristics and meteorological utilization of propeller and vane wind sensors," *J. Applied Meteor.* 3, 182-193.
- Marple, S.Lawrence Jr., 1984. *Digital spectral analysis with applications* Englewood Cliffs, N. J.:Prentice-Hall, Inc.
- Panofsky, H.A., D. Larko, R. Lipschutz, G. Stone, E.F. Bradley, A.J. Bowen, and, J. Højstrup, 1982. "Spectra of velocity components over complex terrain," *Q. J. R. Meteorol. Soc.* 108, 215-230.
- Panofsky, H.A. and J.A. Dutton, 1984. *Atmospheric Turbulence*, New York: John Wiley & Sons, 397pp.
- Pond, S. ,W.G. Large, M. Miyake, R.W. Burling, 1979. "A Gill Twin propeller-vane anemometer for flux measurement during moderate and strong winds," *Bound. Layer Meteor.* 4 , 289-309.

Tennekes and J.L. Lumley, 1972. "A first course in turbulence," Cambridge, Mass.: The MIT Press.

Appendix A. Calibration of the hot-wire system

The most common way to calibrate a hot-wire anemometer is King's law

$$E^2 = A + BU^n \quad (A1)$$

In this equation, E is the output voltage and U is the flow velocity normal to the wire. A, B, and n are constants to be evaluated. In this formula, the effects of changes in temperature, pressure and relative humidity are not considered. Since these changes are important in the field test, corrections for the constants (A, B, n) were therefore introduced, using the equations suggested by Larsen and Busch (1974). The relationship between the constants from King's law and the corrected constants is:

$$E^2 = A + BQ^n$$

where

$$A = A_0(1 - 0.83\varepsilon_t)(1 + 1.34 \frac{e}{p})$$

$$B = B_0(1 - 1.02\varepsilon_t)(1 - 0.63 \frac{e}{p}) \quad (A2)$$

$$Q = (U \frac{p}{p_0})$$

$$\varepsilon_t = \frac{T_g - T_0}{T_w - T_0}$$

$$\frac{e}{p} = (0.006 + 0.000965 \exp^{(.0512T-1)}) \frac{h}{100}$$

In these equations ε_t is the non-dimensional temperature difference, e is the water vapor pressure, p is the ambient pressure, Q is the effective velocity after pressure correction, T_g is the gas temperature, and T_w is the wire temperature.

The subscript 0 in these equations indicates the reference level, which was taken to be 0° C. The value of T_0 is equal to 0. The effectiveness of this temperature correction was evaluated during the calibration. Fig. A1 shows the results of two different calibrations for the same probe. One calibration was performed at 25° C, and the other at 9° C. Fig. A2 shows the correction, using the constants from the 25° C calibration for the the 9° C data set and

vice versa. Compared with the original calibration curve, the result is very good. The root mean squared voltage error is about 0.2%.

The angular response of the hot wire, using Jørgensen's formula (1971) for the effective velocity can be written as:

$$Q_e^2 = U_w^2 + K_0^2 V_w^2 + K_1^2 W_w^2 \quad (A3)$$

In this equation Q_e is effective velocity, and U_w , V_w , W_w are the velocities along the axis of the wire coordinate system. The wire coordinate system is shown in Fig. A3. The constants K_0 and K_1 are the yaw and pitch factors. K_1 is usually approximately 1. K_0 is between 0.1 and 0.2 but varies with the flow velocity and angle (Jørgensen, 1971; Bruun & Tropea, 1985). Because of this characteristic, the velocity along the wire was used to express the effects of flow velocity and angle. Assuming a linear relation between the yaw factor and flow velocity along the wire, the following equation is the formulation for effective velocity.

$$K_0 = a_K + b_K |V_w| \quad (A4)$$

In this equation a_K and b_K are constants.

The velocity vector was transformed to the wire coordinate system of each probe. This transformation has two steps: the jig coordinate transformation, and the probe coordinate transformation. The order of these two

transformations should not be reversed. The equations for these transformations are listed below:

$$\begin{aligned}
 U_j &= U_o \cos \alpha_j \cos \gamma_j \\
 V_j &= -U_o \sin \gamma_j
 \end{aligned}
 \tag{A5}$$

$$W_j = U_o \sin \alpha_j \cos \gamma_j$$

where U_o is the wind velocity, α_j is the pitch angle of the hot-wire jig in the jig coordinate system, and γ_j is the yaw angle in the jig coordinate system. Next is the probe coordinate system transformation.

$$\begin{aligned}
 U_p &= U_j \cos \gamma_p \cos \alpha_p + V_j \sin \gamma_p - W_j \cos \gamma_p \cos \alpha_p \\
 V_p &= -U_j \sin \gamma_p \cos \alpha_p + V_j \cos \gamma_p + W_j \sin \gamma_p \sin \alpha_p
 \end{aligned}
 \tag{A6}$$

$$W_p = -U_j \sin \alpha_p + W_j \cos \alpha_p$$

In these equations, the γ_p is the yaw angle of the hot-wire probe in the probe coordinate system, and α_p is the probe pitch angle. The probes' arrangement has the normal wires in the horizontal plane and the inclined wire probe in the vertical plane. Therefore, the γ_p is ± 30 degrees for the normal wire probes and zero for the inclined wire probe, and α_p is zero for the normal wire probes and 45 degrees for the inclined wire probe. The wire coordinate system is basically the same as the probe coordinate system for the normal

wire probes. But, for the inclined wire probe, V_w is equal to W_p and W_w is equal to V_p . By using Eq. A1 to Eq. A6, the relationship of the output voltages and the wind velocity components can be analyzed. An IMSL routine was used to minimize the error between the calculated voltage and the measured voltage. At the minimum error condition, the corresponding values of A_0 , B_0 , n , a_k , b_k , and K_1 , are calibration results that can be used to calculate the wind vector in the field test.

A1.1 Test facilities and equipments

The hot wire jig was calibrated at the VPI 3'x 3' subsonic wind tunnel. Although this wind tunnel has about 3% turbulence intensity in high speeds range, the turbulence intensity of the speeds less than 15 m/s was found to be less than 0.3%. Calibration equipment included a *DANTEC* constant temperature bridge and anemometer (No. 56C-17) and a manually adjusted traverse stand. Additionally, the four-pole low pass Bessel filters used in the field test with a cutoff frequency of 10 Hz and a gain of 1.94, were used in every hot-wire probes output. The frequency response of this filter is shown in Fig. A4. The data acquisition portion of this calibration included a *COMPAQ* portable personal computer and a DT-2801 A/D board from *Data Translation*.

A1.2 Calibration process

Calibration was divided into two steps: first the yaw angle test, then the pitch angle test. The calibration speeds ranged from 2 m/s to 13 m/s, which was the expected wind speed range. The intervals were from 1 m/s at speeds below 6 m/s to intervals of 2 m/s at higher speeds. Seven speeds were used for calibration. In the yaw angle test, the jig was rotated from -60 degrees to +60 degrees with a 15-degree interval. For the pitch angle test the hot-wire jig was rotated in the vertical plane from -45 degrees to +45 degrees with the same intervals as in the yaw test. In data acquisition part, the sampling speed was 100 Hz. 500 observations were recorded at each position and then the mean value and the turbulence intensity were calculated.

A1.3 Result

The results are shown in Table A1. The values of A_0 and B_0 are approximately twice the values of the calibration result without the filter. The difference in the values of the calibration constants, A_0 and B_0 , can be explained by the gain of the filter being approximately equal to two. The value of K_0 varies from 0.1 to 0.2 depending on the velocity along the wire.

This result is in the same range as results derived by Bruun and Tropea (1985) for the same kind of probe (TSI 1210).

Appendix B. Uncertainty analysis of the hot-wire calibration results

Using the calibration constants and the input velocities and voltages, the uncertainty analysis was performed. The relative velocity error was derived from the difference between input velocity components and those calculated from the input voltages, divided by the input total velocities. The relative voltage error was derived in a similar manner, but using the input voltages as references, and using input velocities to calculate the voltages.

Table 2 shows the root mean squared (rms) calibration error. The rms voltage error is about 1%, but the rms error for each velocity component is much higher, at about 10%. Tables A2 - A4 list the relative error of each velocity component related to total velocity at different jig yaw angles. The U component has an uncertainty of 10% or larger when the jig yaw angle is larger than ± 30 degrees or when wind speed is around 3 to 5 m/s at 0

degrees (Table A2). For the V component, the uncertainty is around 10% at speeds less than 5 m/s, and at the jig yaw angle larger than ± 30 degrees (Table A3). For the W component, the uncertainty is around 20 % at the jig yaw angle of -30 degrees (Table A4). Table A4 shows that as the yaw angle becomes negative the error become negative. In Table A3, the trend is reversed. It reveals some negative correlation between the error of V and W components at different yaw angles (the yaw angle in hot-wire jig calibration is equal to the minus value of the wind azimuth angle).

There are several reasons for this negative correlation. First, there is error in the wind azimuth angle, caused by the non-uniform flow field of the wind tunnel or the yaw angle setting error in the traverse system.

From past experimentation on the flow field of this wind tunnel, the axial velocity changes to 3% at the high speed range (50 m/s). This contributes to the calibration error. Due to the size and angle setting of the hot jig system, the blockage effect causes the tunnel flow velocity to slow down and oscillate in a range of ± 0.003 " of water in the inclined manometer reading. This corresponds to a 3% velocity error. The error caused by the traverse system inaccuracy is about ± 1 degree. The major cause is the initial alignment of the hot-wire jig with the flow.

Second, the position of the normal wire probe might not be in the horizontal plane, or in the vertical plane for the inclined wire probe case.

There is a roll angle offset for each probe. Here an offset of two or three degrees in rolling angle is not easily detectable. Table A5 gives the error caused by these offsets. For one degree off in yaw angle, the error in effective velocity would be 4% when the yaw angle of the jig is around 45 degrees. For one degree off in the roll angle of the probe, the error in the effective velocity would be about 0.3% when the jig yaw angle is about 45 degrees. Although the installation position of each probe was carefully marked, the calibration error in the rolling angle of the probe still influenced the result.

The inclined manometer reading error also contributes to the uncertainty. The smallest scale in the incline manometer is 0.01" of water. The error in the reading was ± 0.002 ", and the effect on the velocity uncertainty was around 2%. Considering these possible errors, the 10% uncertainty in effective velocity is reasonable.

Appendix C. Dissipation method

The dissipation method is based on two assumptions. First, that in the surface layer the turbulence dissipation is equal to the production. And, second that the stress in this region is constant. From Kolmogorov's law for the inertial subrange,

$$S(k) = a\epsilon^{2/3}k^{5/3} \quad (A7)$$

where $S(k)$ is the wave number spectrum, a is the so-called universal constant [in Panofsky *et al.* (1982) for complex terrain a equals 0.55 was used], ϵ is the dissipation, and k is the wave number in the wind direction. Then assume that Taylor's hypothesis is correct that the turbulence eddy convects along with the wind without changing its shape. Then the relation between the wave number, frequency, and wind speed can be expressed as:

$$k = \frac{2\pi f}{Um} \quad (A8)$$

Based on this hypothesis, the wave number spectrum relates to the frequency spectrum by the following equation:

$$kS(k) = fS(f) \quad (A9)$$

Assuming that dissipation equals production under the neutral condition, the relationship is:

$$\varepsilon = -\overline{uw} \frac{\partial U}{\partial z} \quad (A10)$$

where the velocity gradient in the vertical direction $\frac{\partial U}{\partial z}$ in the log region of the boundary layer is:

$$\frac{\partial U}{\partial z} = \frac{u_*}{\kappa z}$$

In this equation κ is the von Karman constant, which is equal to 0.4. A non-dimensional dissipation function ϕ_ε was used

$$\phi_\varepsilon = \varepsilon \frac{\kappa z}{u_*^3} \quad (A11)$$

Combining Eqs. A7 through A11, and defining the non-dimensional frequency as ($N = \frac{fz}{Um}$), the normalized spectrum is derived.

$$\frac{fS_u(f)}{u_*^2 \phi_\varepsilon^{2/3}} = a(\kappa 2\pi)^{-2/3} N^{-2/3} \quad (A12)$$

Substituting the values of κ and α , this equation becomes

$$\frac{fS_u(f)}{u_*^2 \phi_\varepsilon^{2/3}} = 0.3N^{-2/3} \quad (A13)$$

Using Eq. A13 and the spectral values in the inertial subrange of the u spectrum, the friction velocity was estimated.

Figures



Figure 1. K-Gill propeller vane anemometer (left) and hot-wire jig system (right).

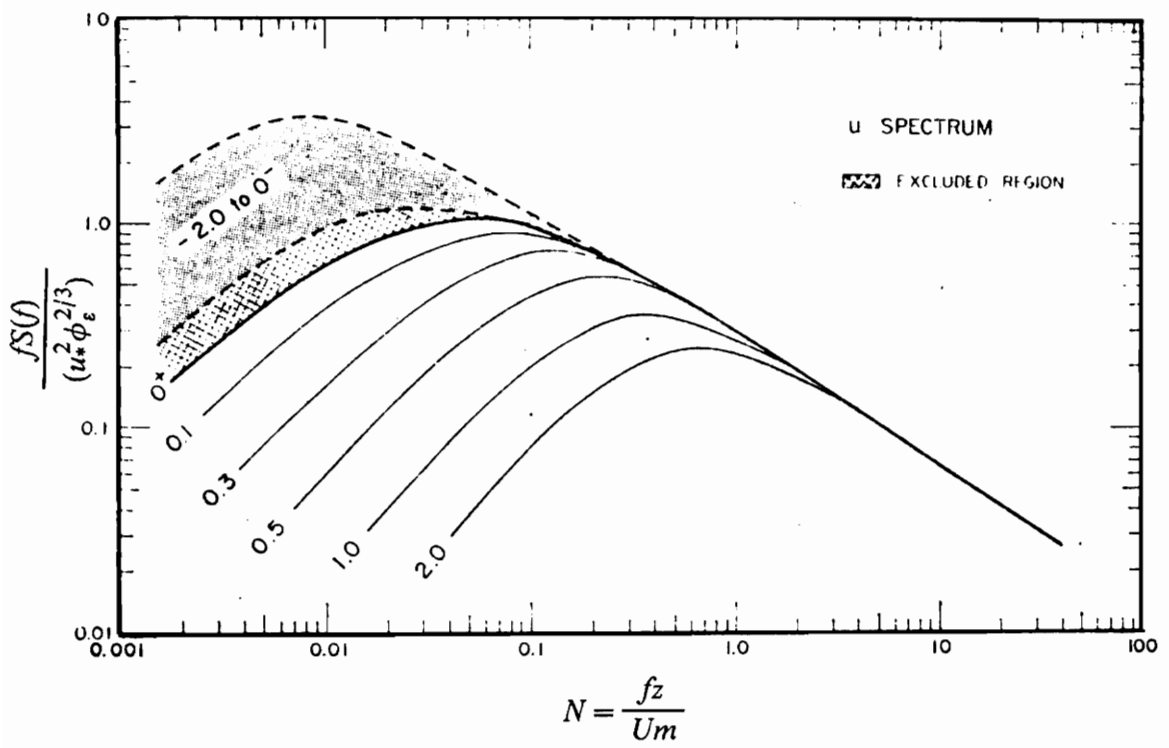


Figure 2. The u spectrum from Kaimal *et al.* (1972).

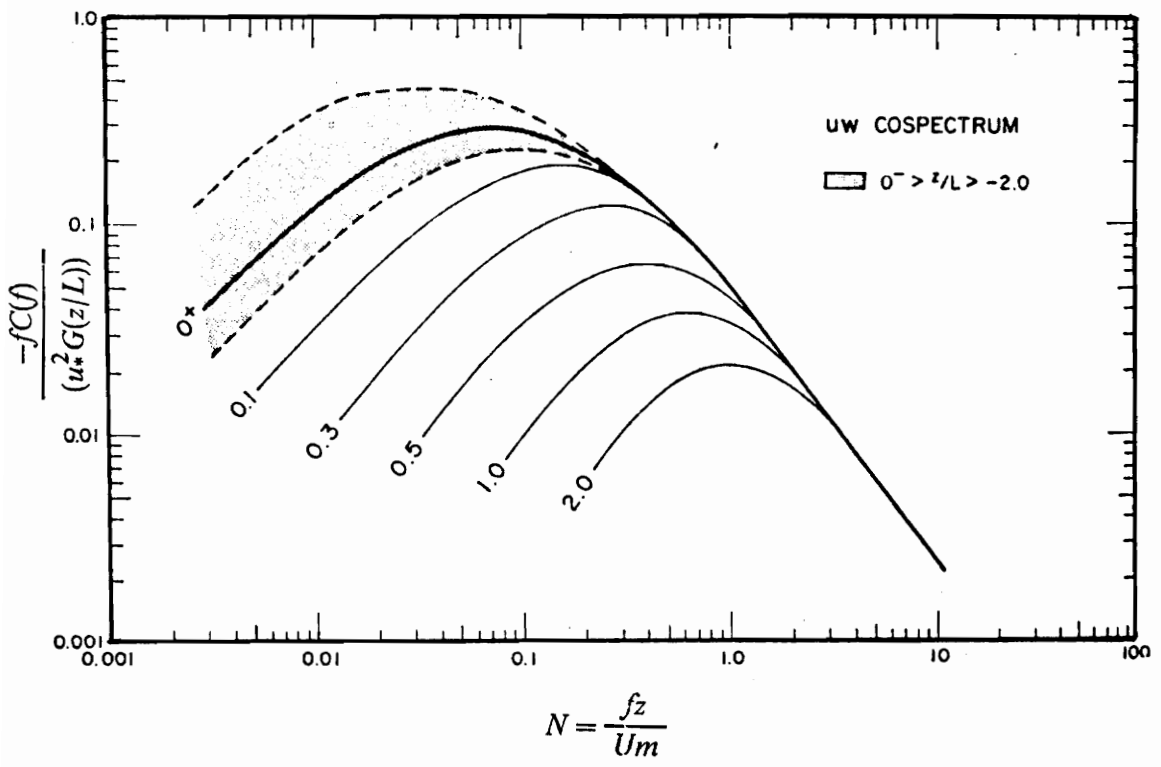


Figure 3. The uw cospectrum from Kaimal *et al.* (1972).

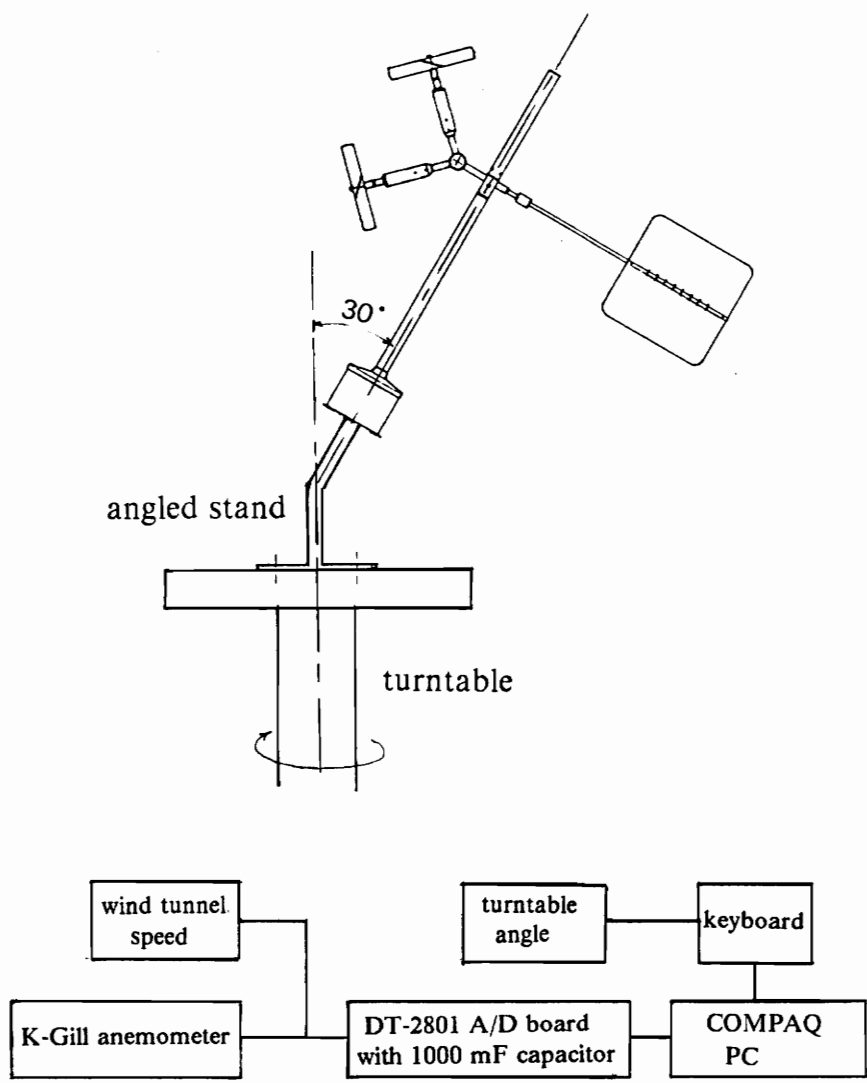


Figure 4. The calibration traverse system of the K-Gill anemometer.

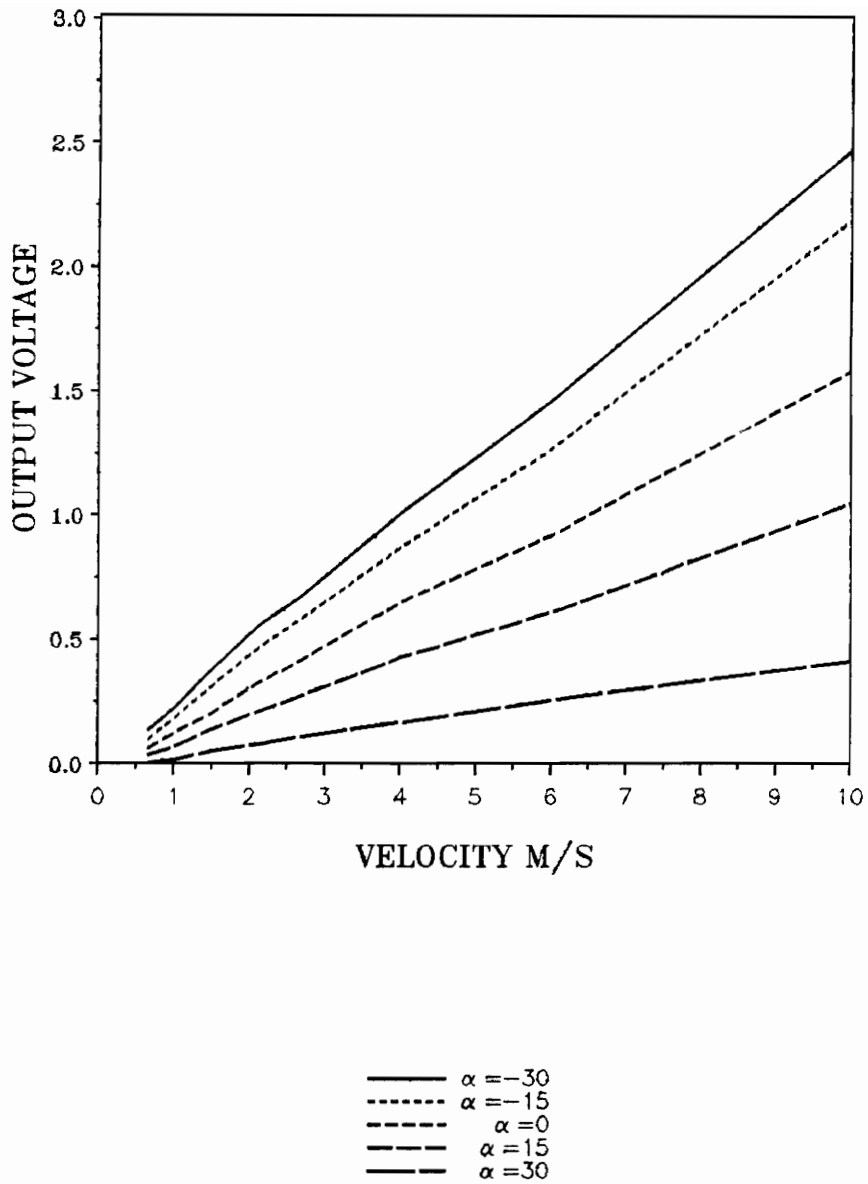
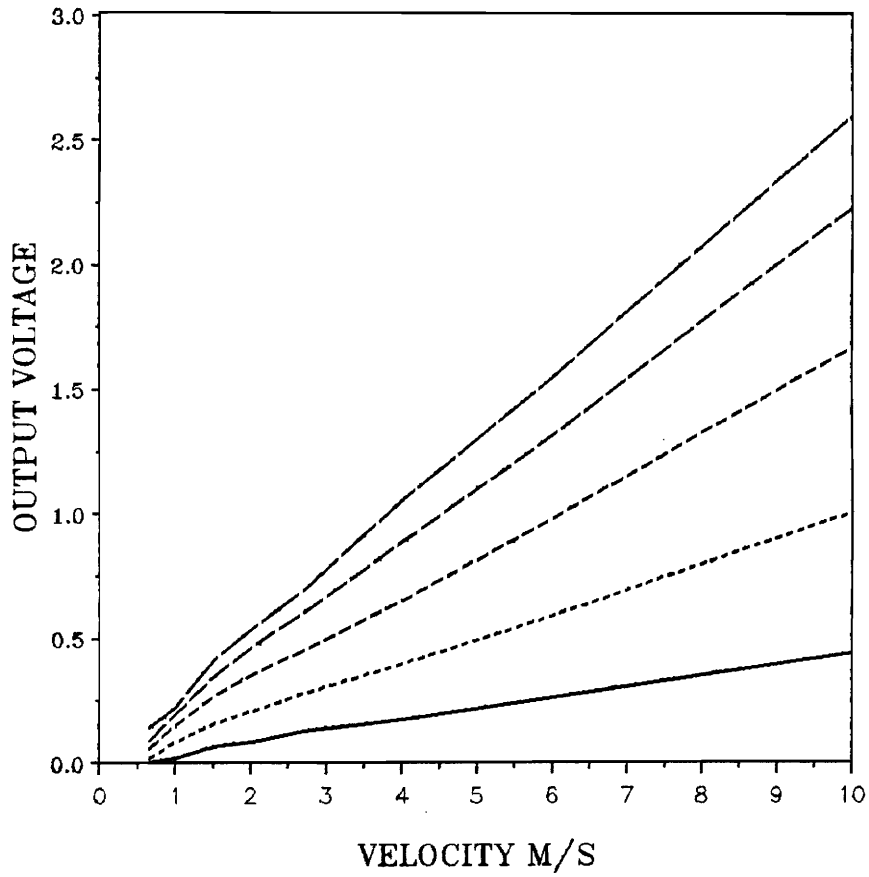


Figure 5. The output voltage of the upper propeller anemometer at different speeds and angles.



— $\alpha = -30$
 - - - $\alpha = -15$
 - - - $\alpha = 0$
 - - - $\alpha = 15$
 - - - $\alpha = 30$

Figure 6. The output voltage of the lower propeller anemometer at different speeds and angles.

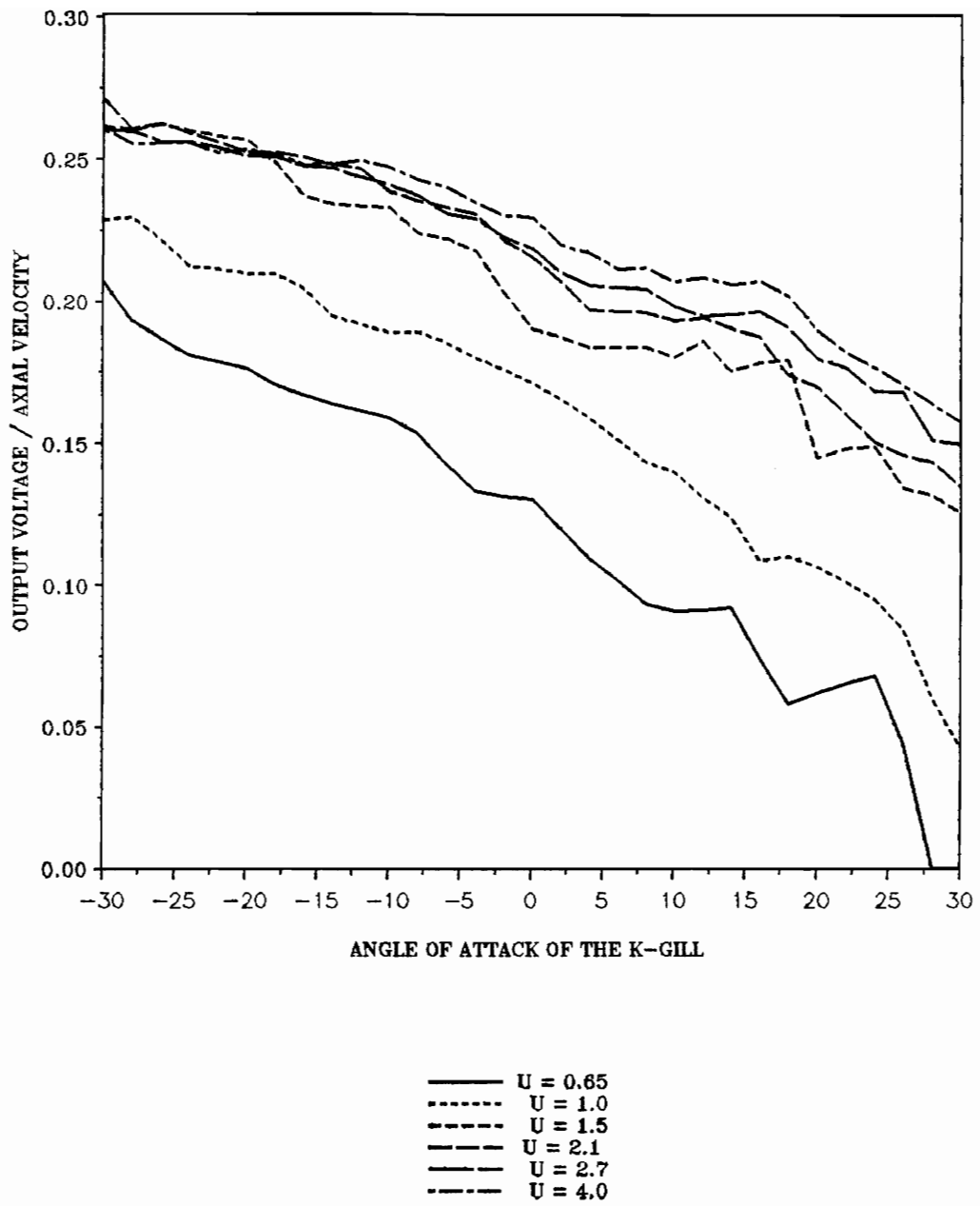


Figure 7. Comparisons of the angular response at different speeds.

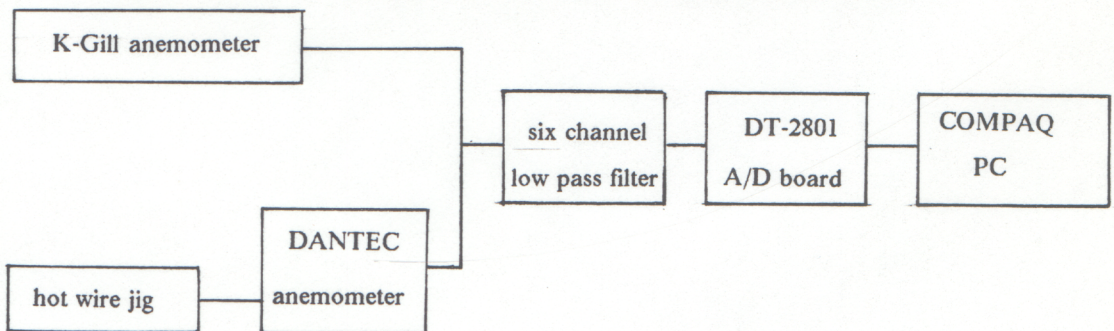


Figure 8. The set-up of the Field test.

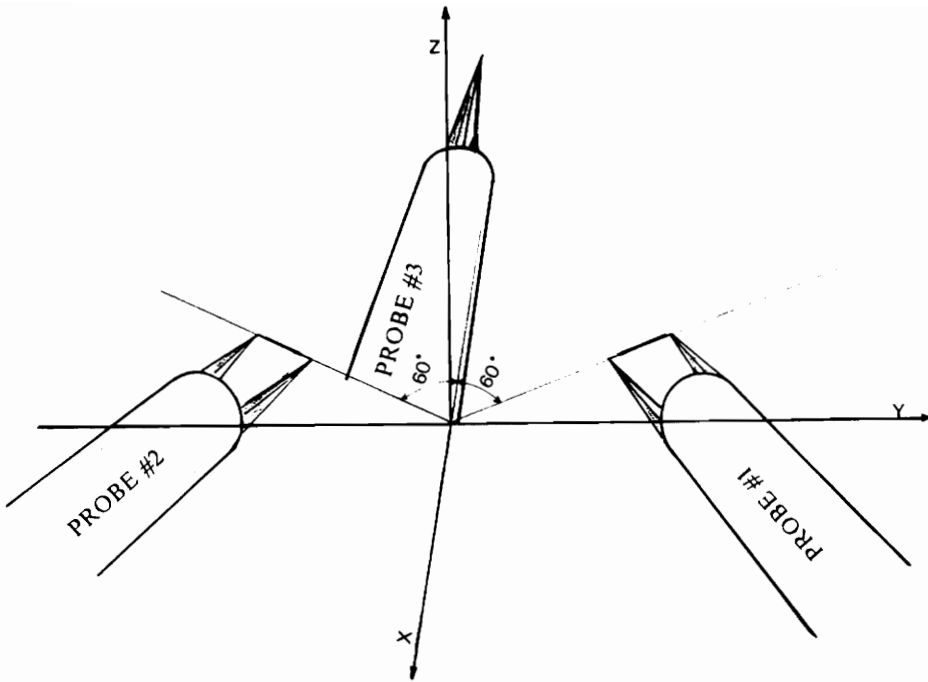
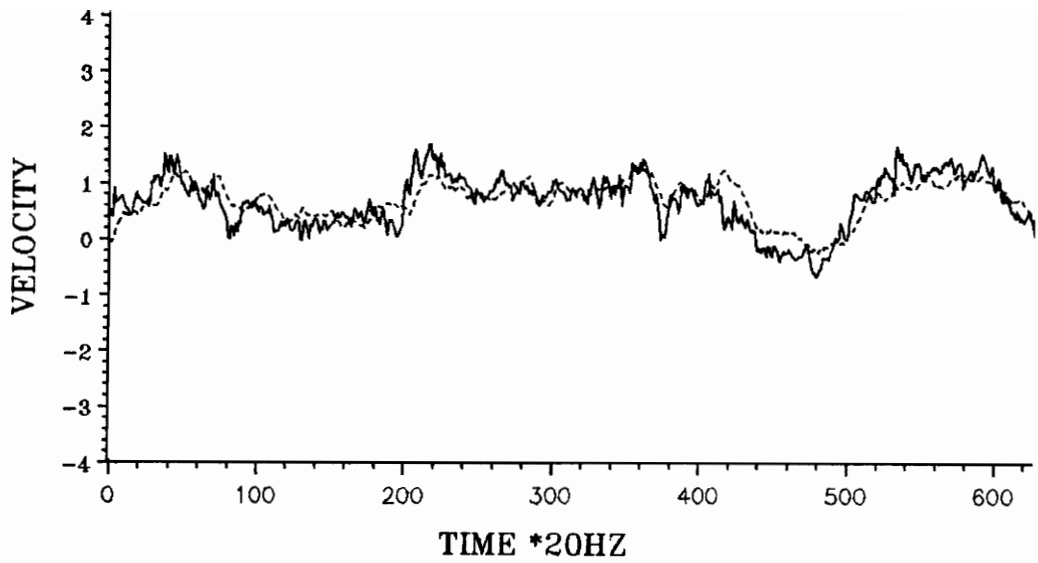


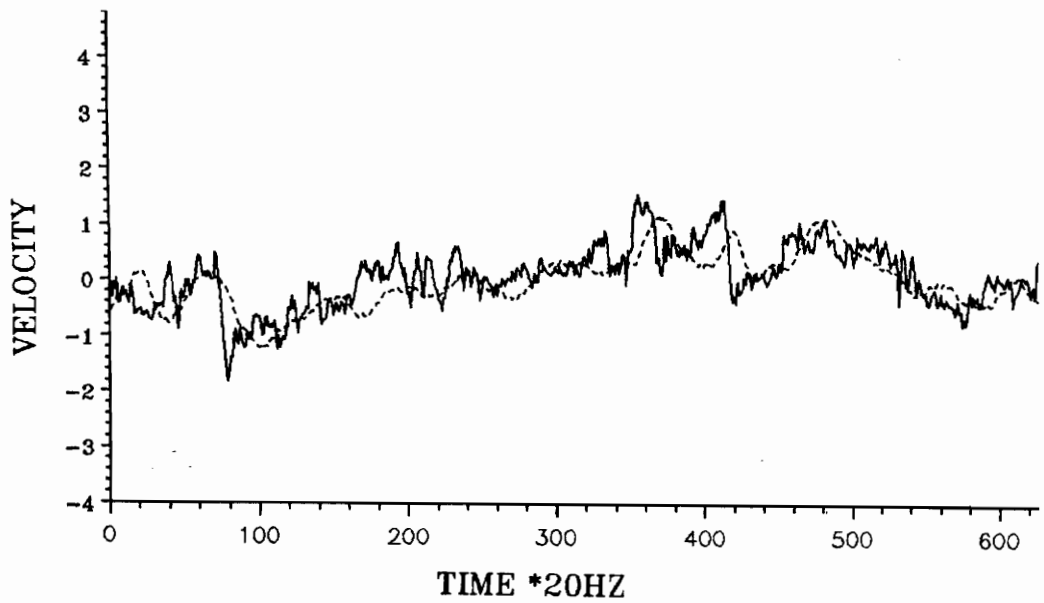
Figure 9. Hot-wire jig coordinate system and probe arrangement.



— solid line ---- hot wire output

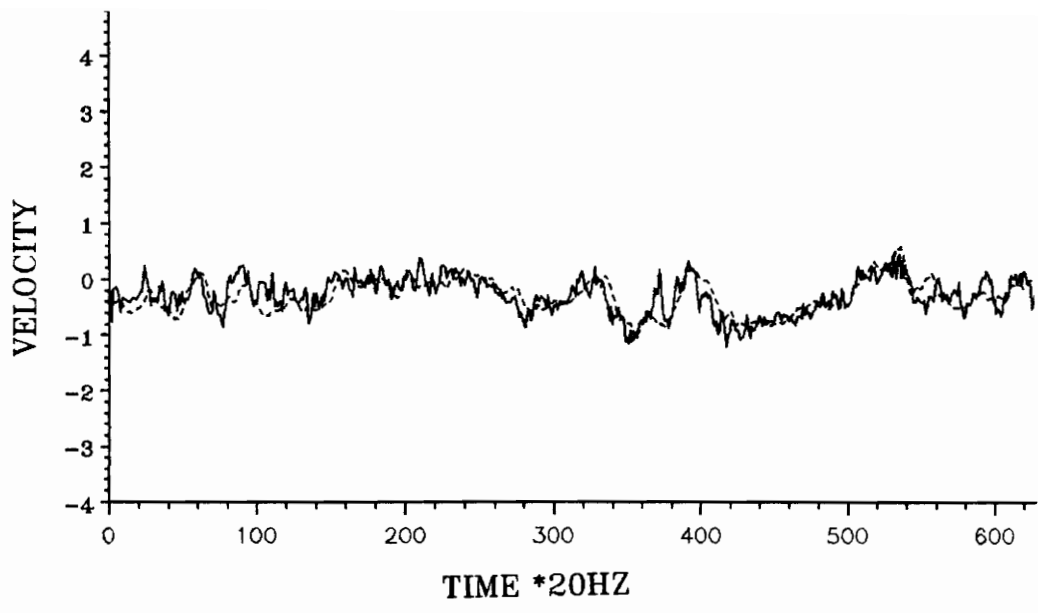
..... dot line ----- K-Gill output

Figure 10. Comparison of the u components from both hot-wire and K-Gill anemometer when the wind angle was close to 0 degrees.



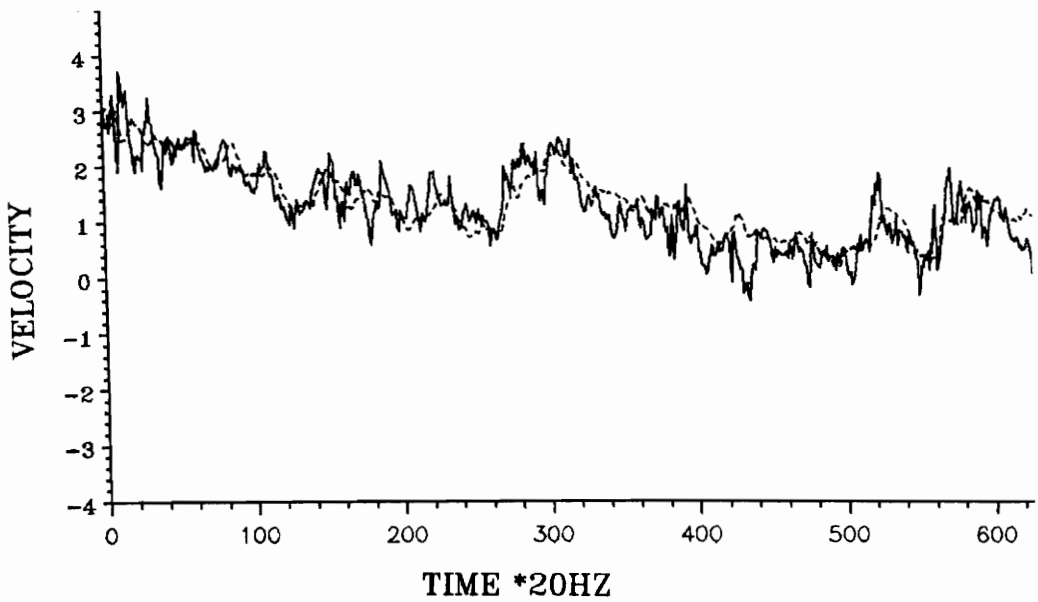
——— solid line ---- hot wire output
 dot line K-Gill output

Figure 11. Comparison of the v components from both hot-wire and K-Gill anemometer when the wind angle was close to 0 degrees.



——— solid line ---- hot wire output
 dot line K-Gill output

Figure 12. Comparison of the w components from both hot-wire and K-Gill anemometer when the wind angle was close to 0 degrees.



— solid line ---- hot wire output
- - - - dot line - - - - K-Gill output

Figure 13. Comparison of the u components from both hot-wire and K-Gill anemometer when the wind angle was about 30 degrees.

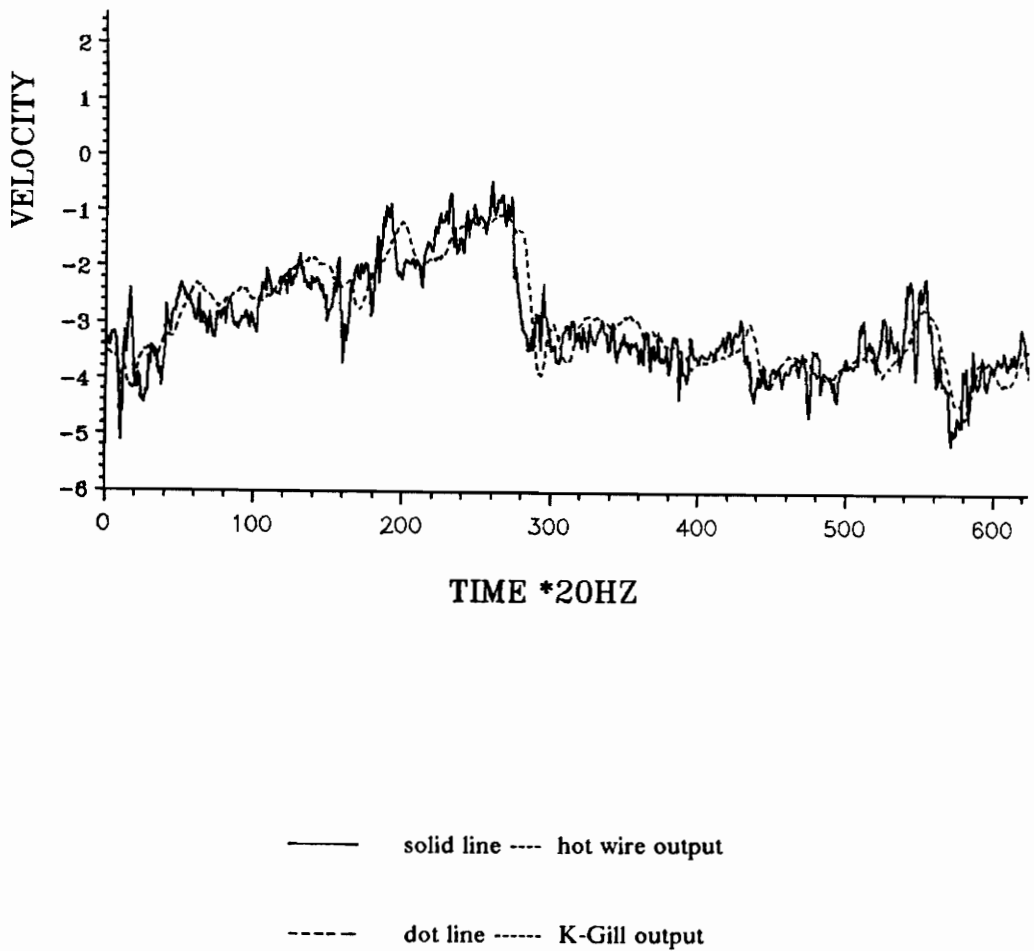
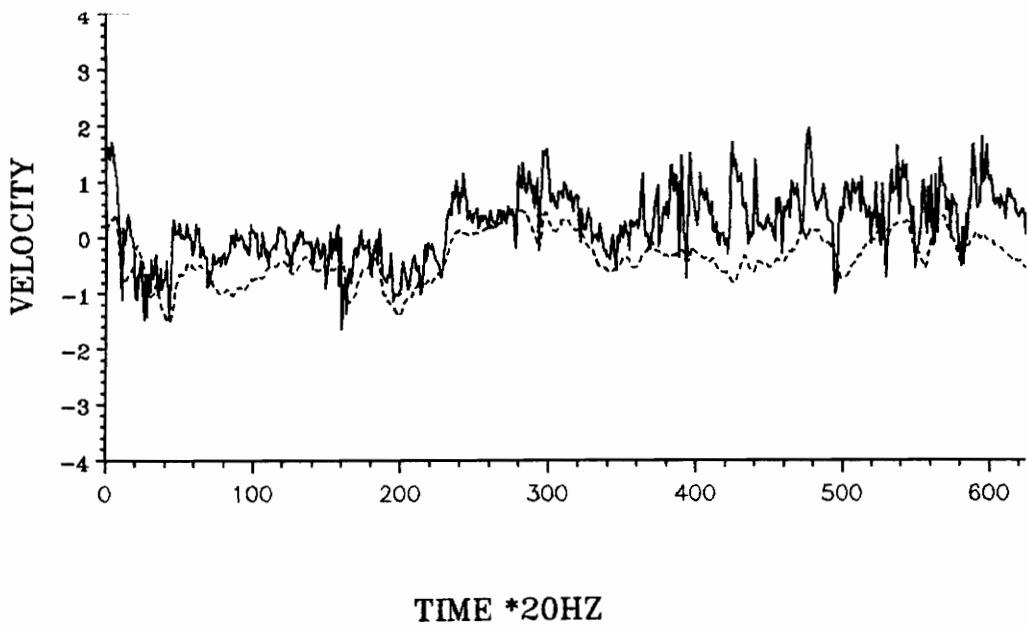
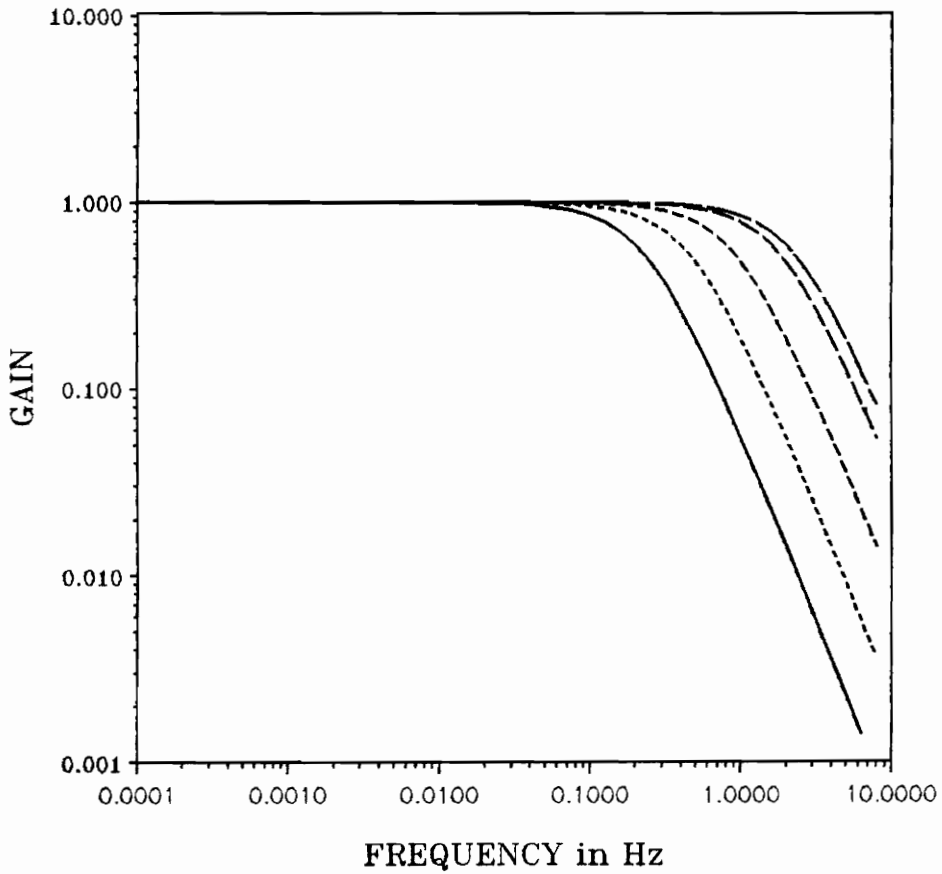


Figure 14. Comparison of the v components from both hot-wire and K-Gill anemometer when the wind angle was about 30 degrees.



—— solid line ---- hot wire output
----- dot line ----- K-Gill output

Figure 15. Comparison of the w components from both hot-wire and K-Gill anemometer when the wind angle was about 30 degrees.



——— U = 2.
 U = 4.
 - - - - U = 8.
 - · - · U = 18.
 - - - - U = 20.

Figure 16. Idealized frequency response of the K-Gill anemometer at different speeds.

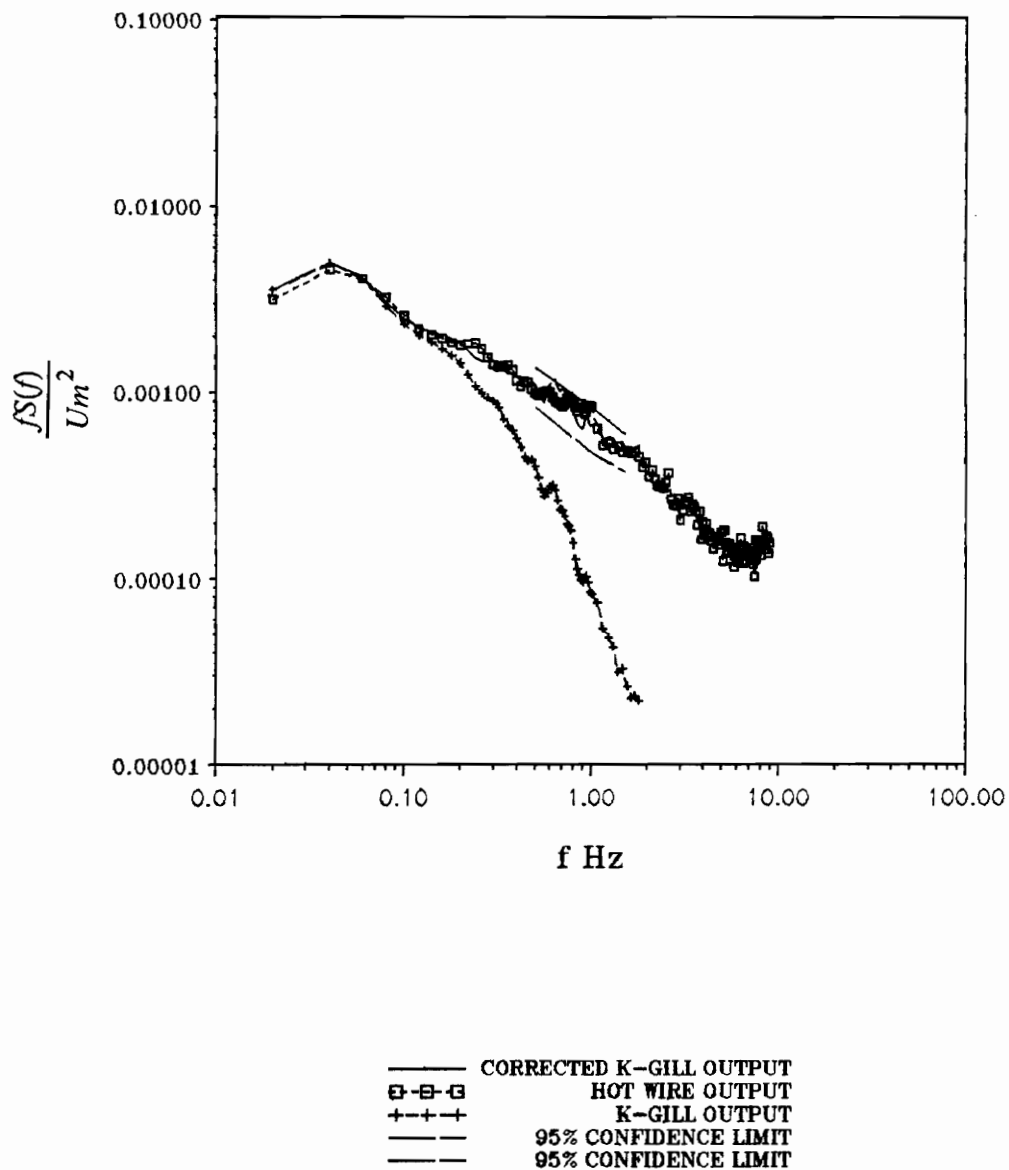


Figure 17. Comparison of the u spectra from different instruments and the corrected result for data set #1.

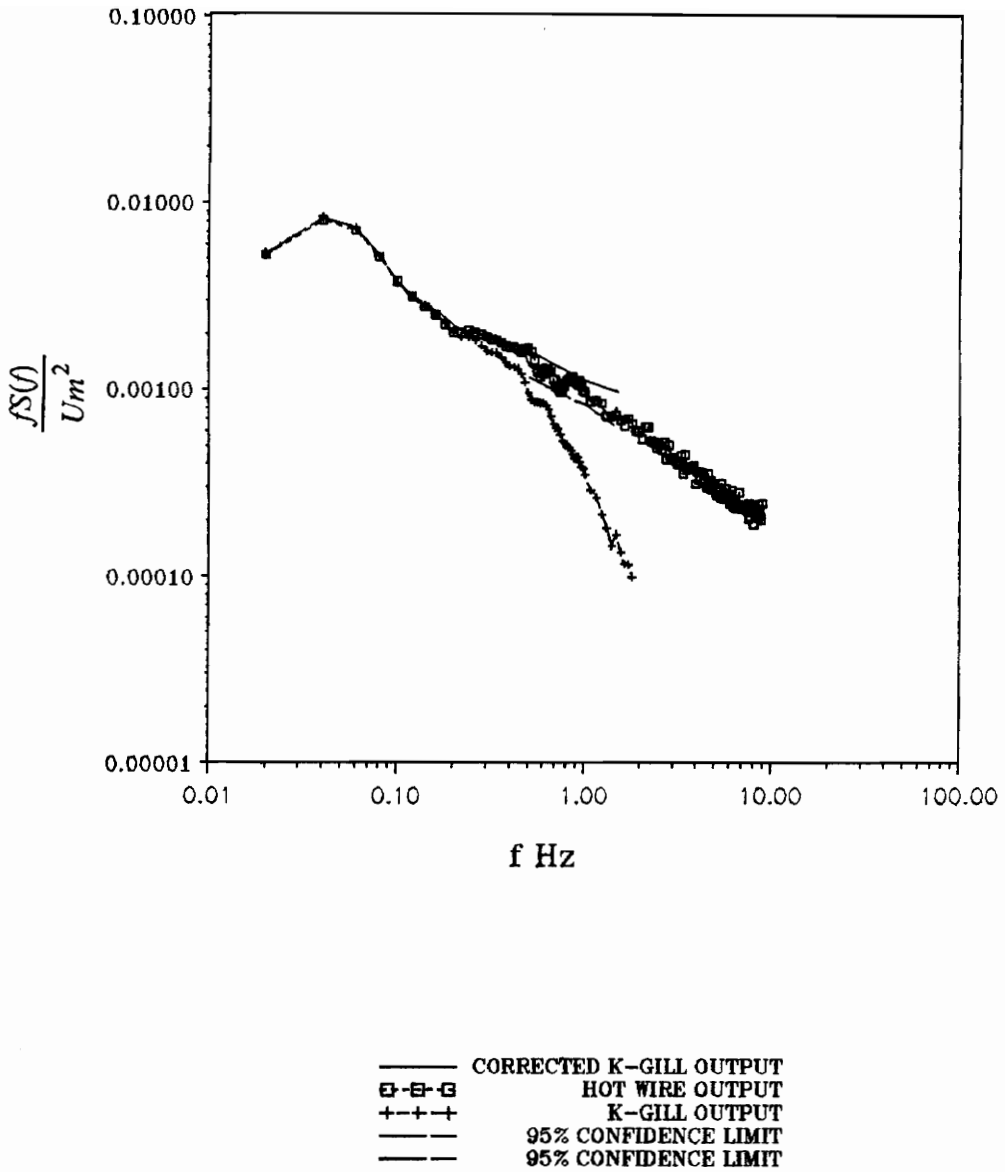


Figure 18. Comparison of the u spectra from different instruments and the corrected result for data set #2.

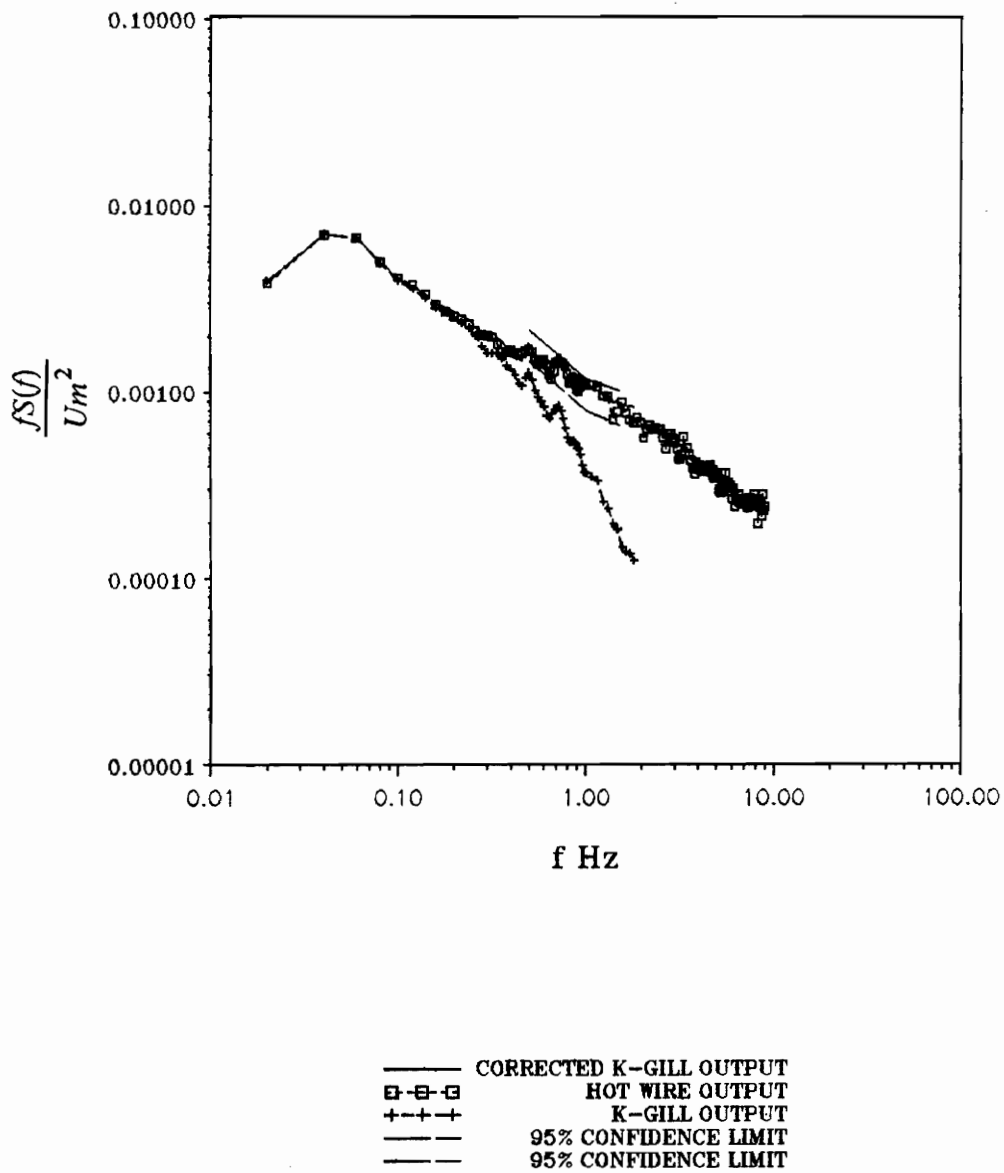


Figure 19. Comparison of the u spectra from different instruments and the corrected result for data set #3.

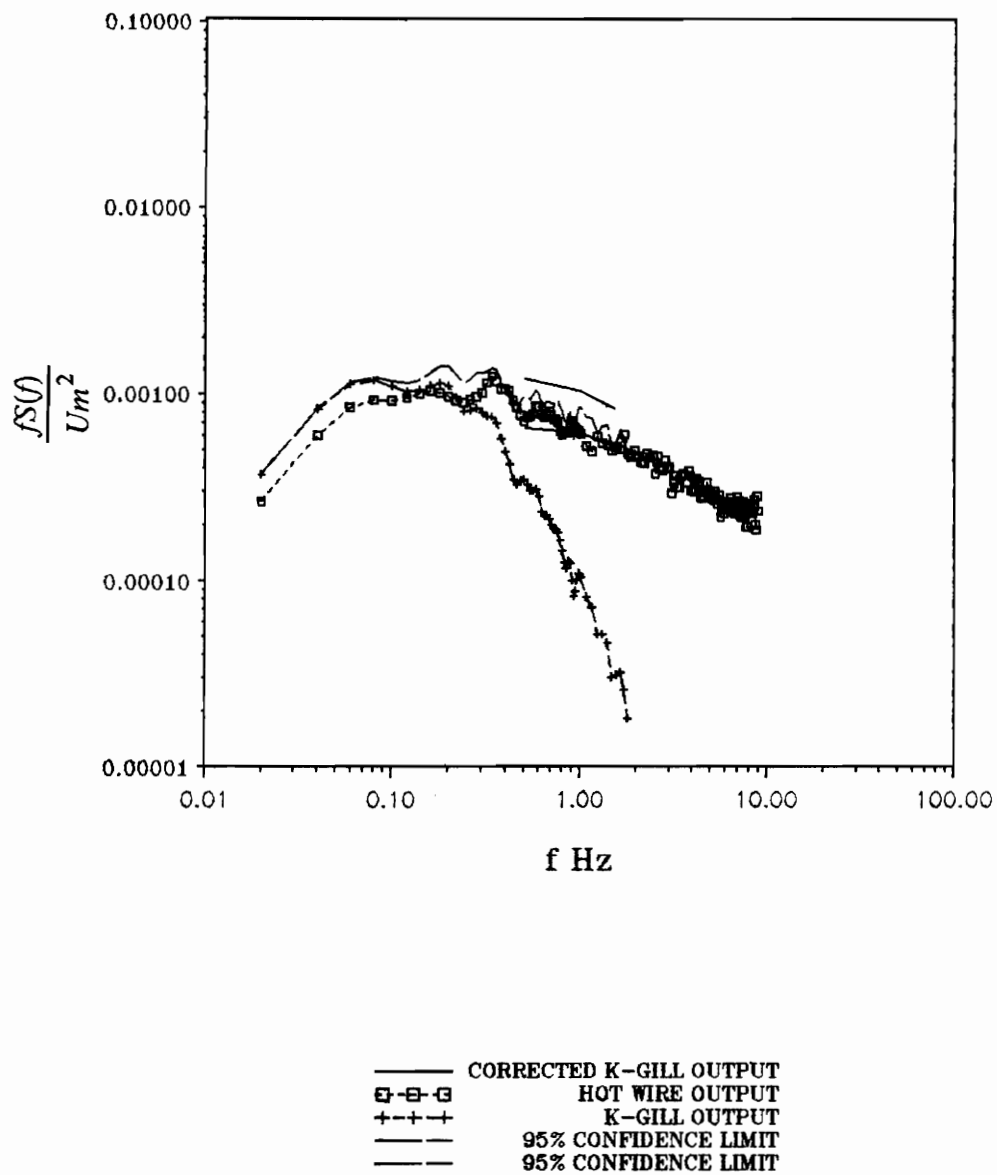


Figure 20. Comparison of the w spectra from different instruments and the corrected result for data set #1.

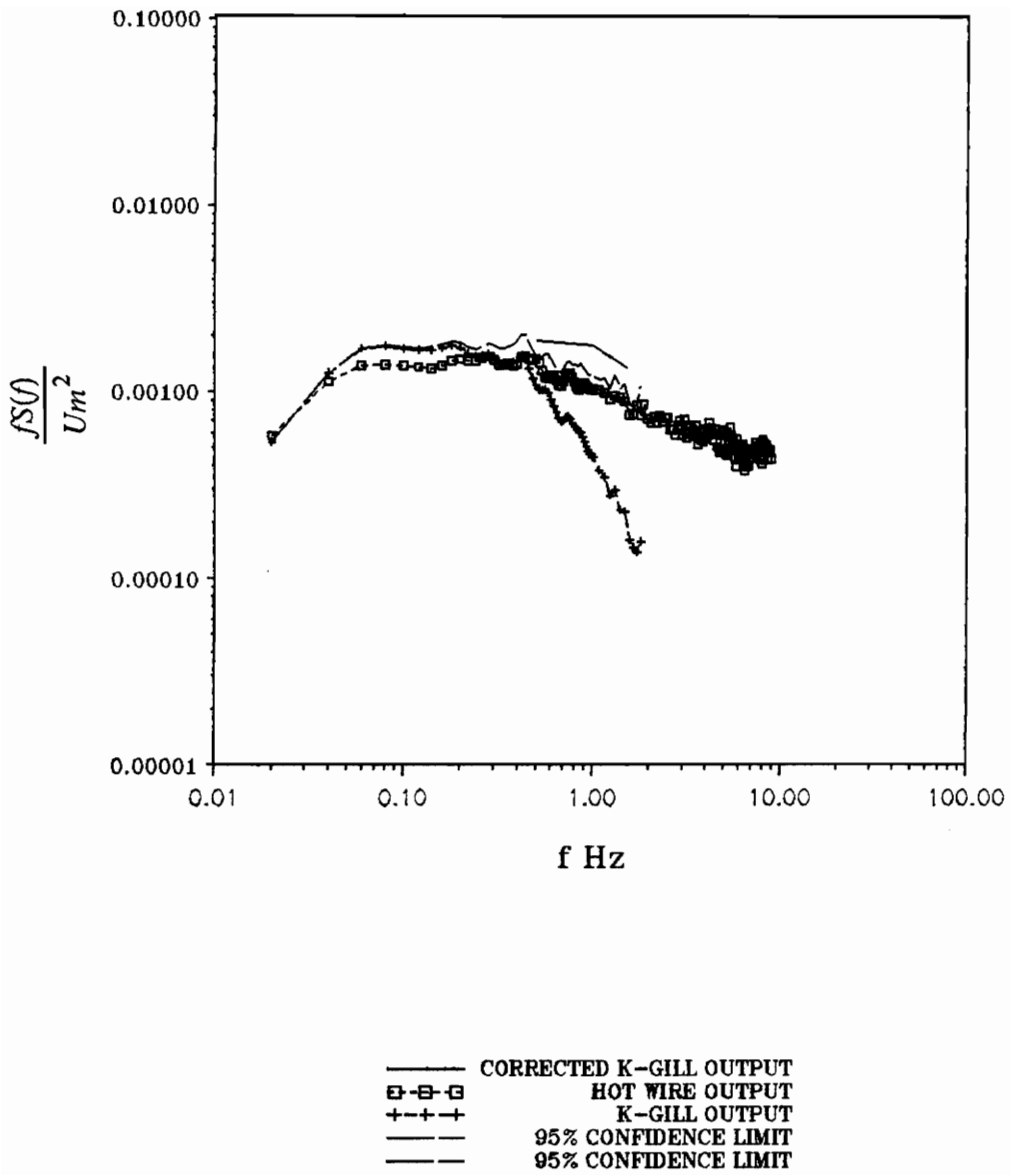


Figure 21. Comparison of the w spectra from different instruments and the corrected result for data set #2.

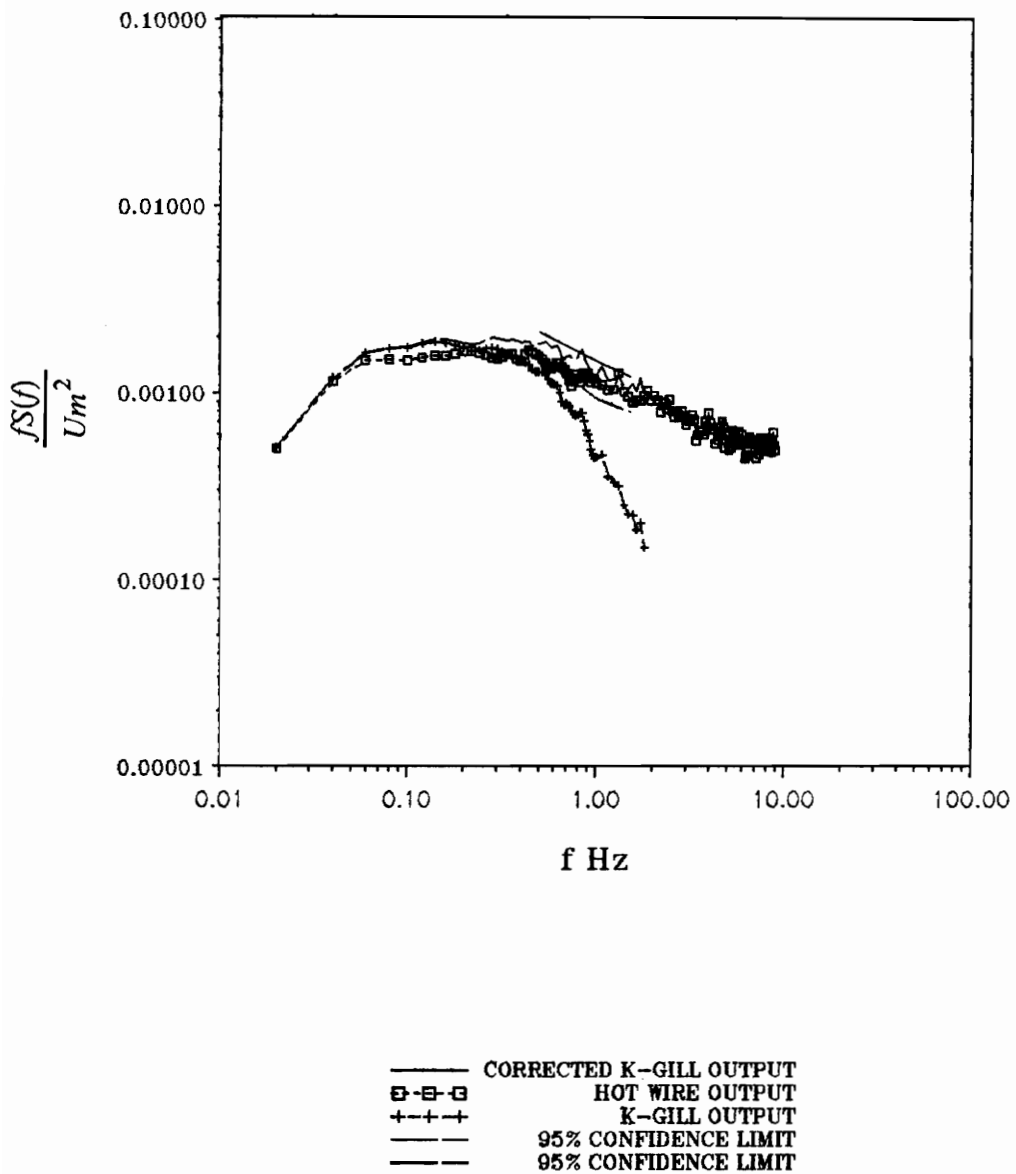


Figure 22. Comparison of the w spectra from different instruments and the corrected result for data set #3.

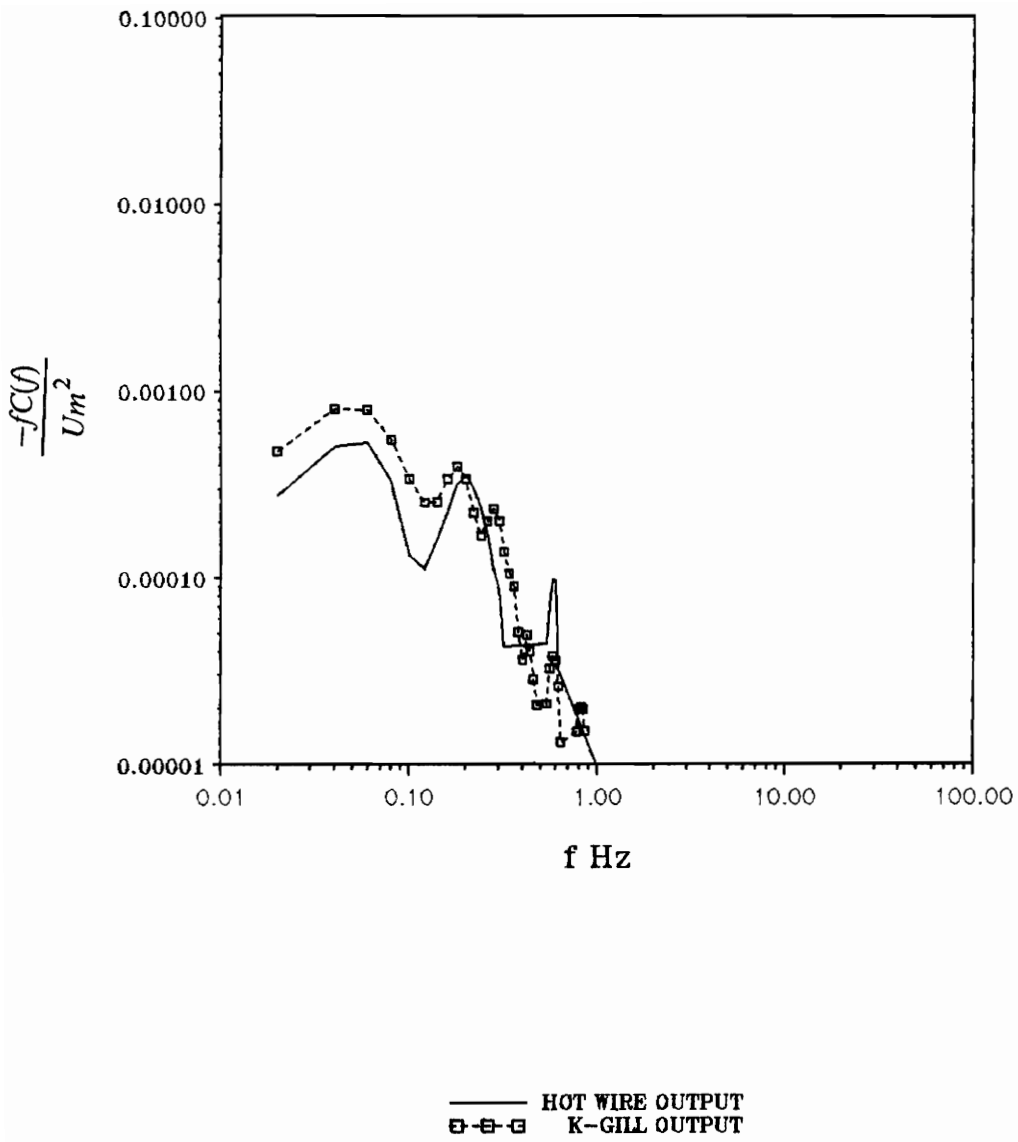
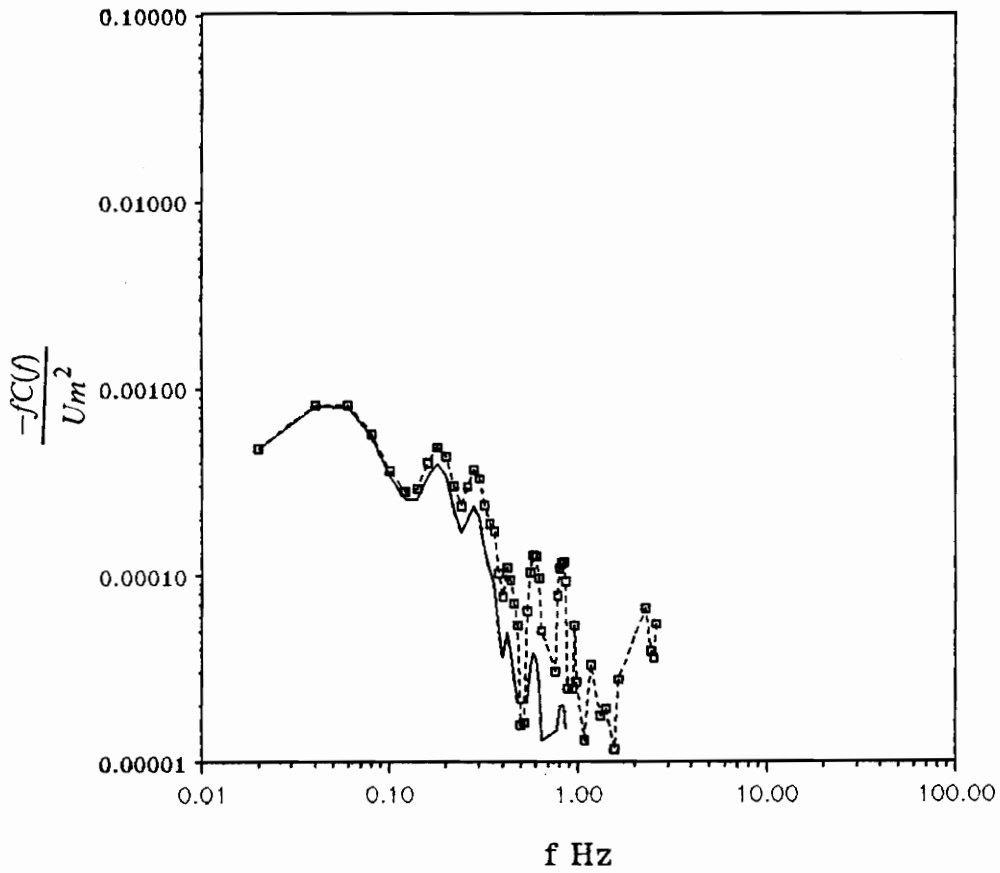
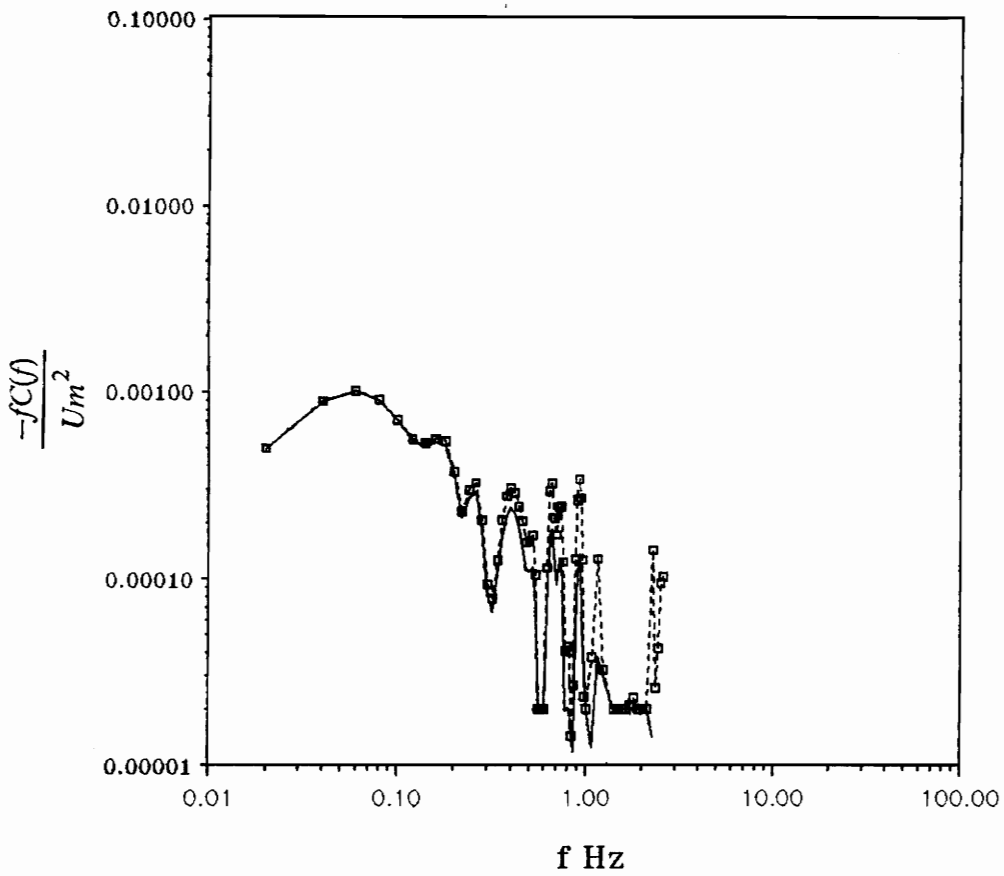


Figure 23. The uw cospectra from both hot-wire and K-Gill anemometers.



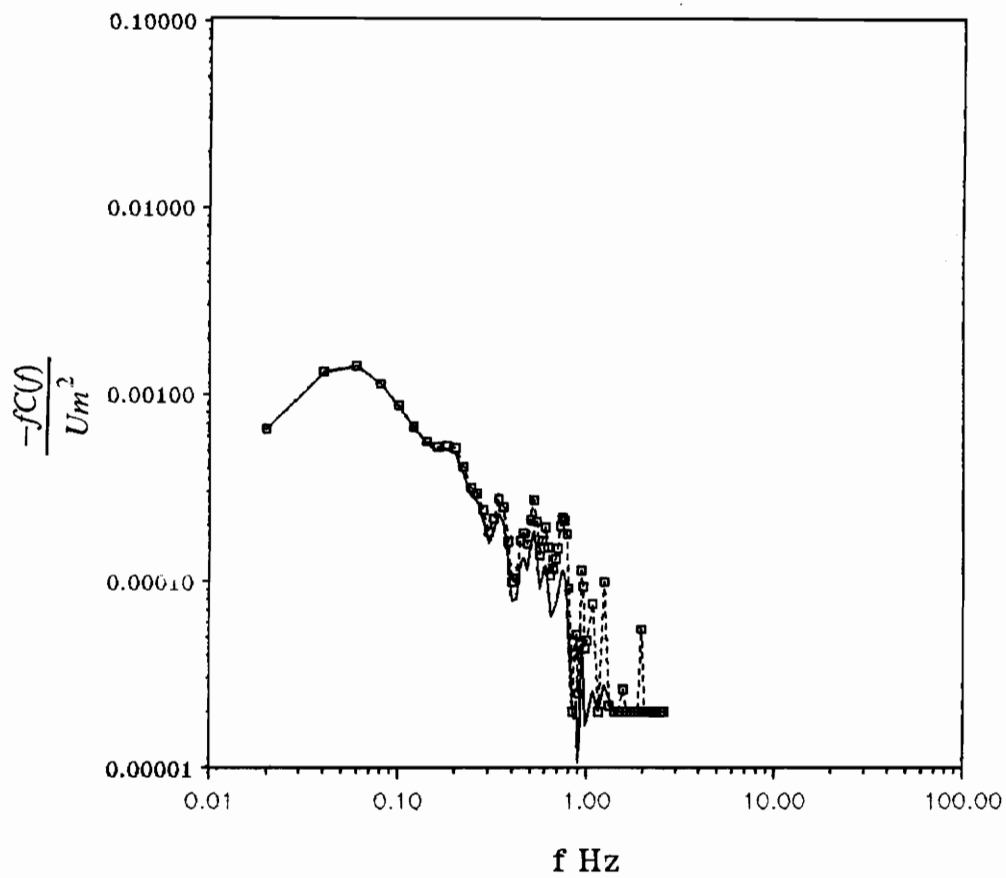
————— K-GILL OUTPUT
 □-□-□ CORRECTED K-GILL OUTPUT

Figure 24. Comparison of the uw cospectra from the K-Gill anemometer and the corrected result for data set #1.



————— K-GILL OUTPUT
 - - - - - CORRECTED K-GILL OUTPUT

Figure 25. Comparison of the uw cospectra from the K-Gill anemometer and the corrected result for data set #2.



———— K-GILL OUTPUT
 □-□-□ CORRECTED K-GILL OUTPUT

Figure 26. Comparison of the uw cospectra from the K-Gill anemometer and the corrected result for data set #3.

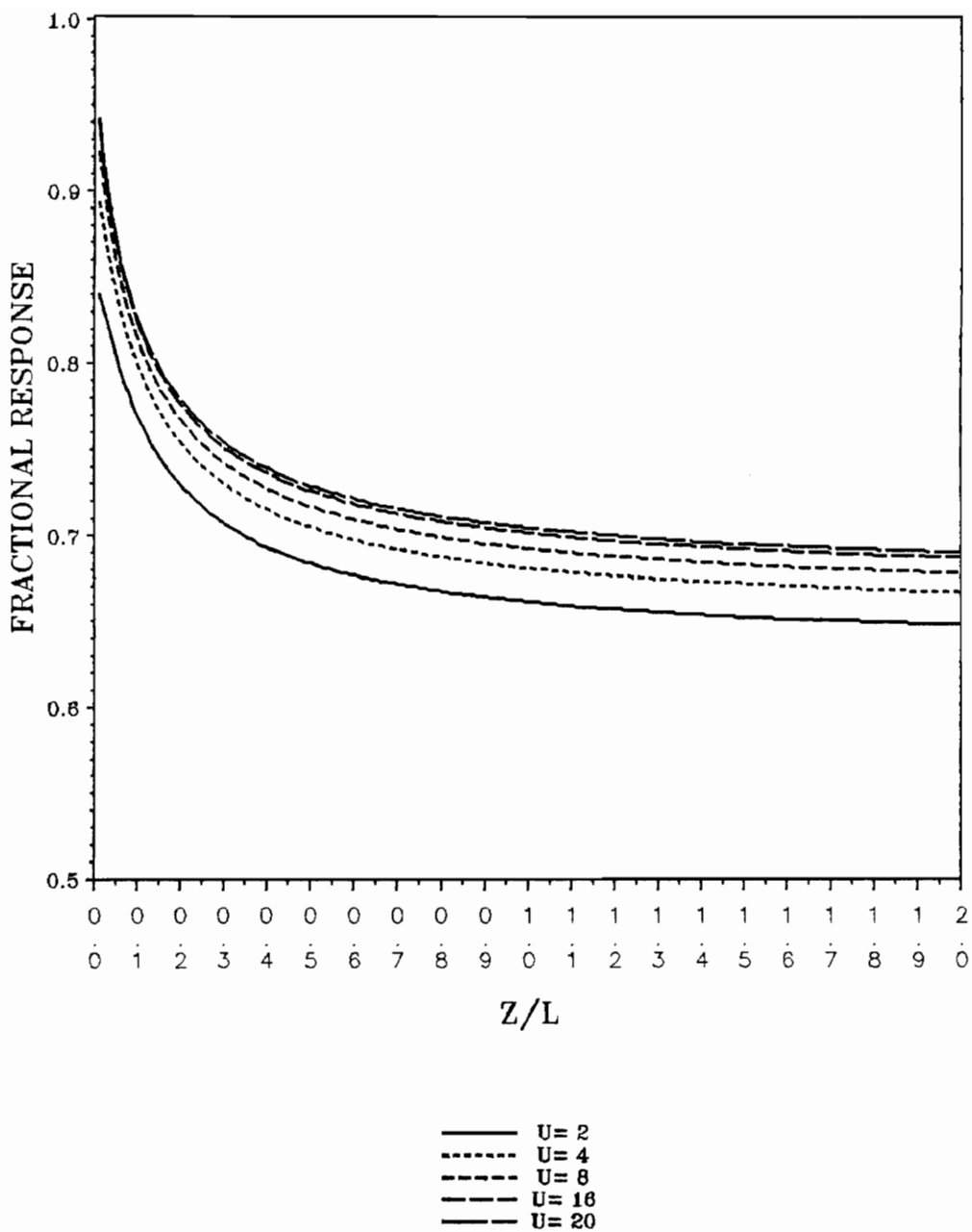


Figure 27. The fractional response of the u variance from the K-Gill anemometer.

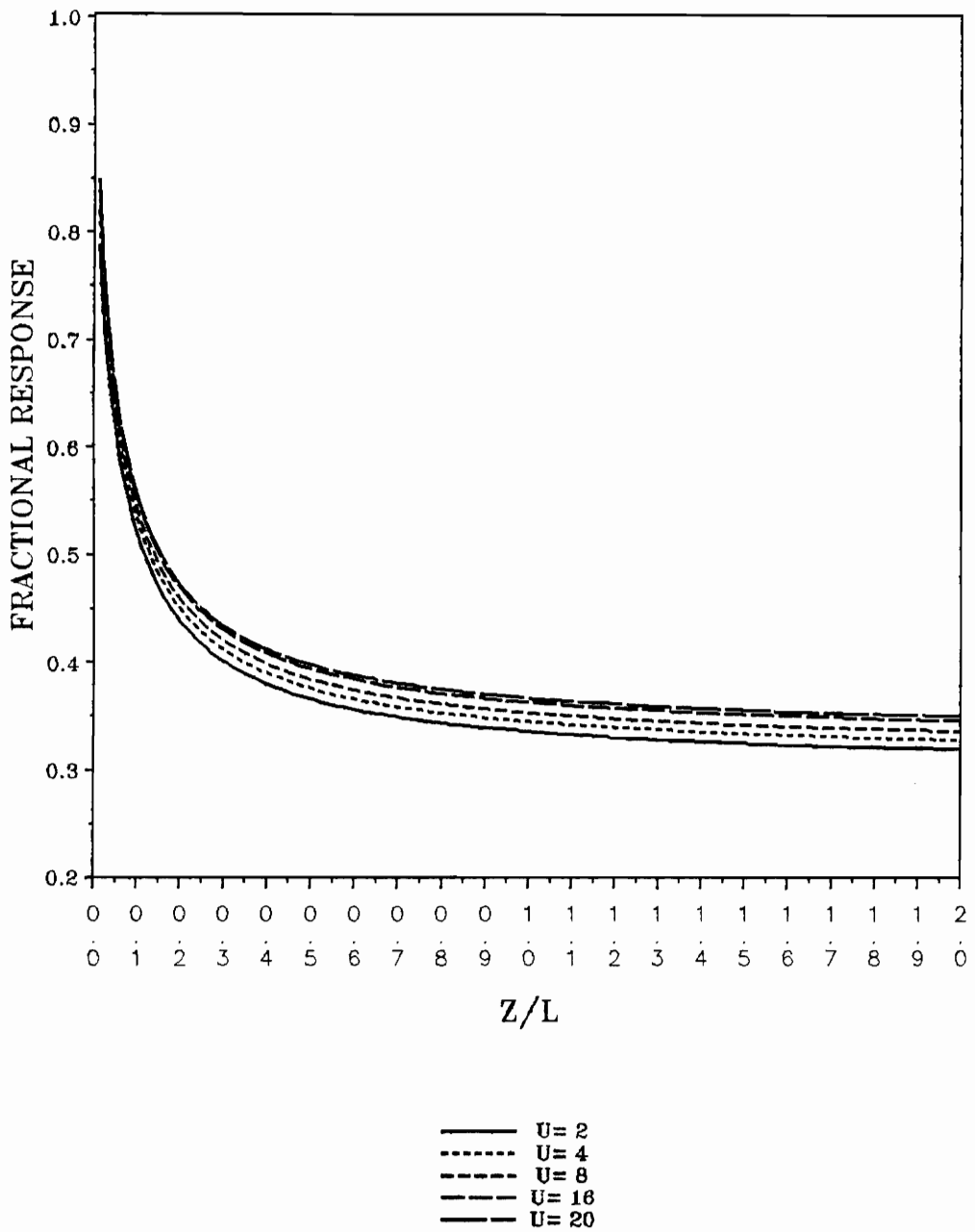


Figure 28. The fractional response of the w variance from the K-Gill anemometer.

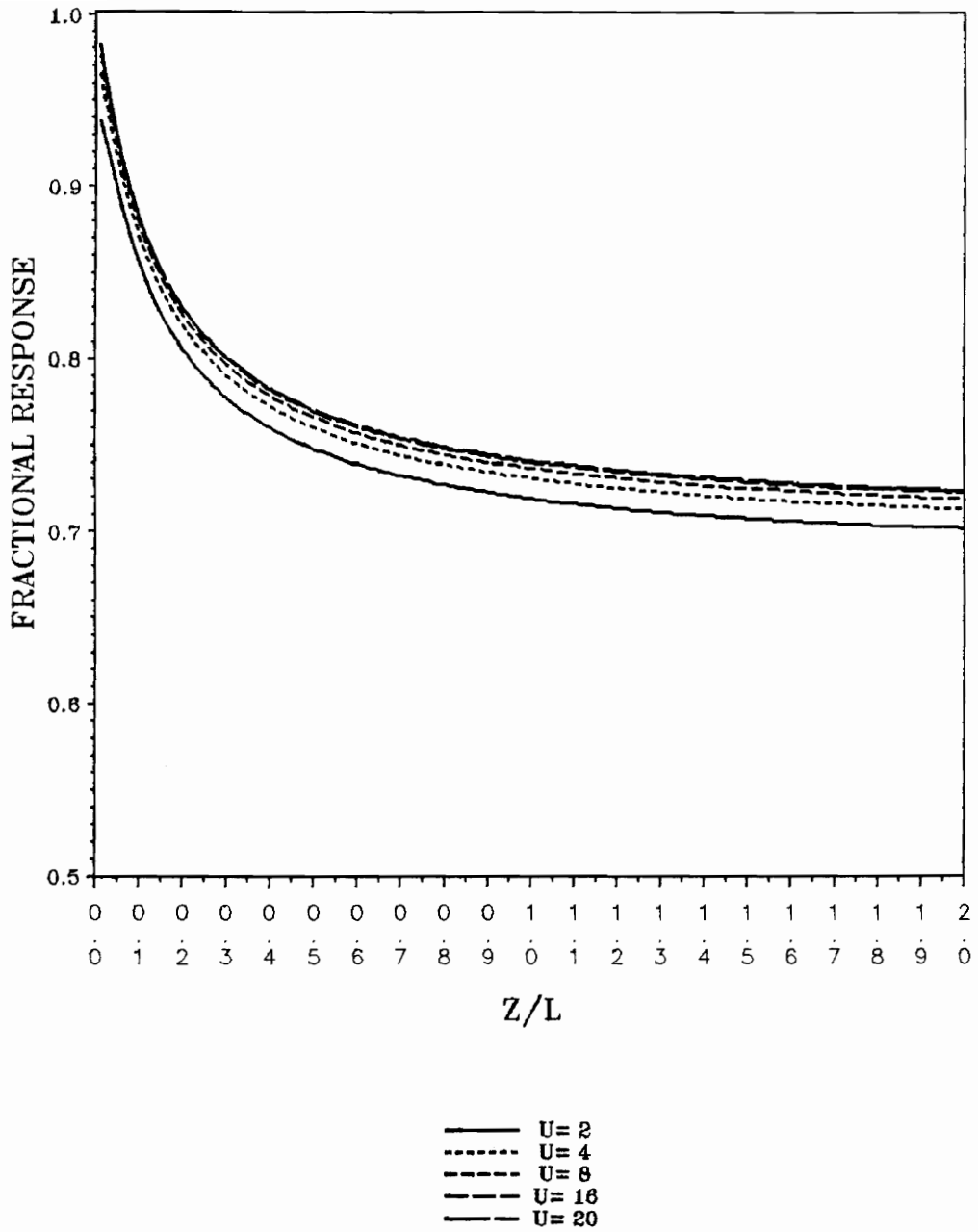


Figure 29. The fractional response of the uw covariance from the K-Gill anemometer.

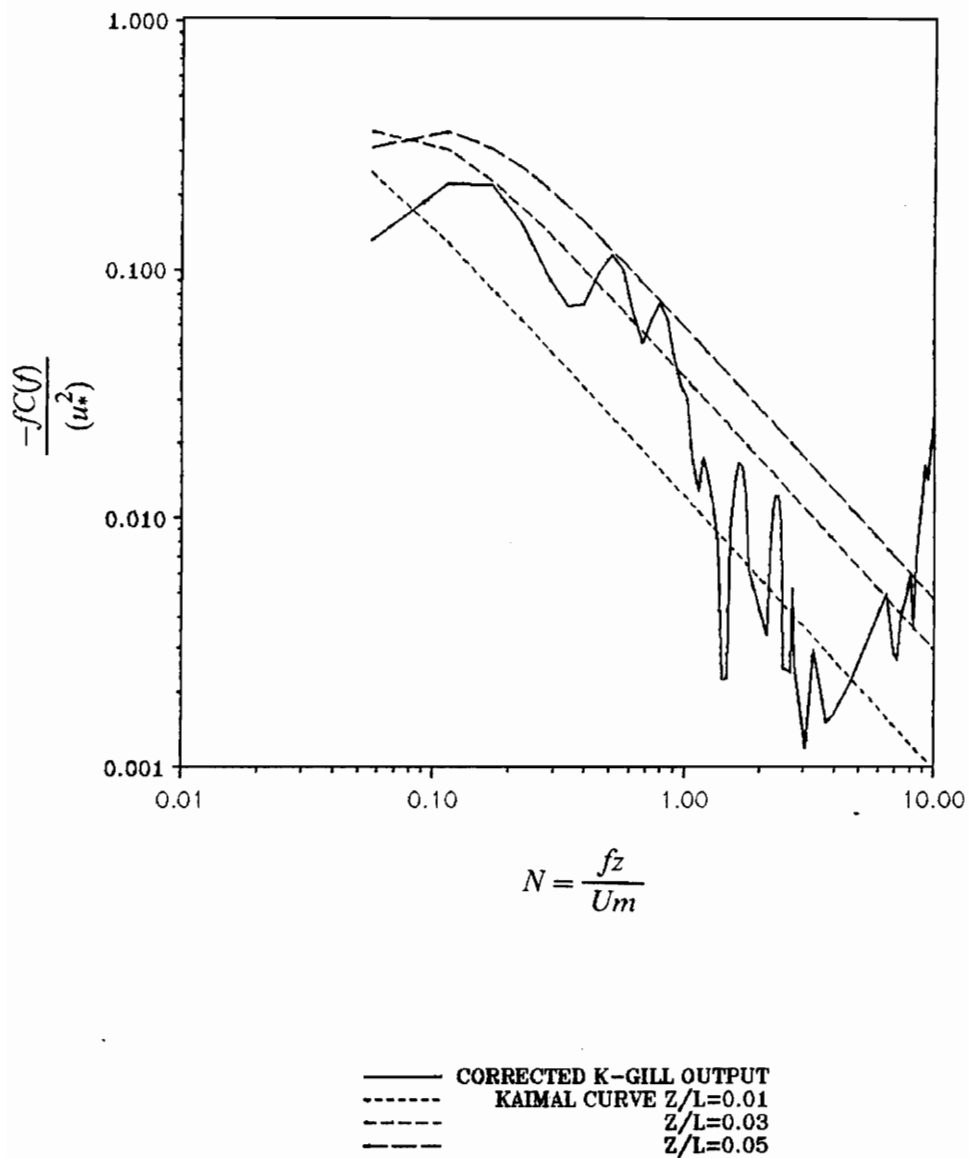


Figure 30. Comparison of the normalized cospectra at different stability conditions and Kaimal's result for data set #1.

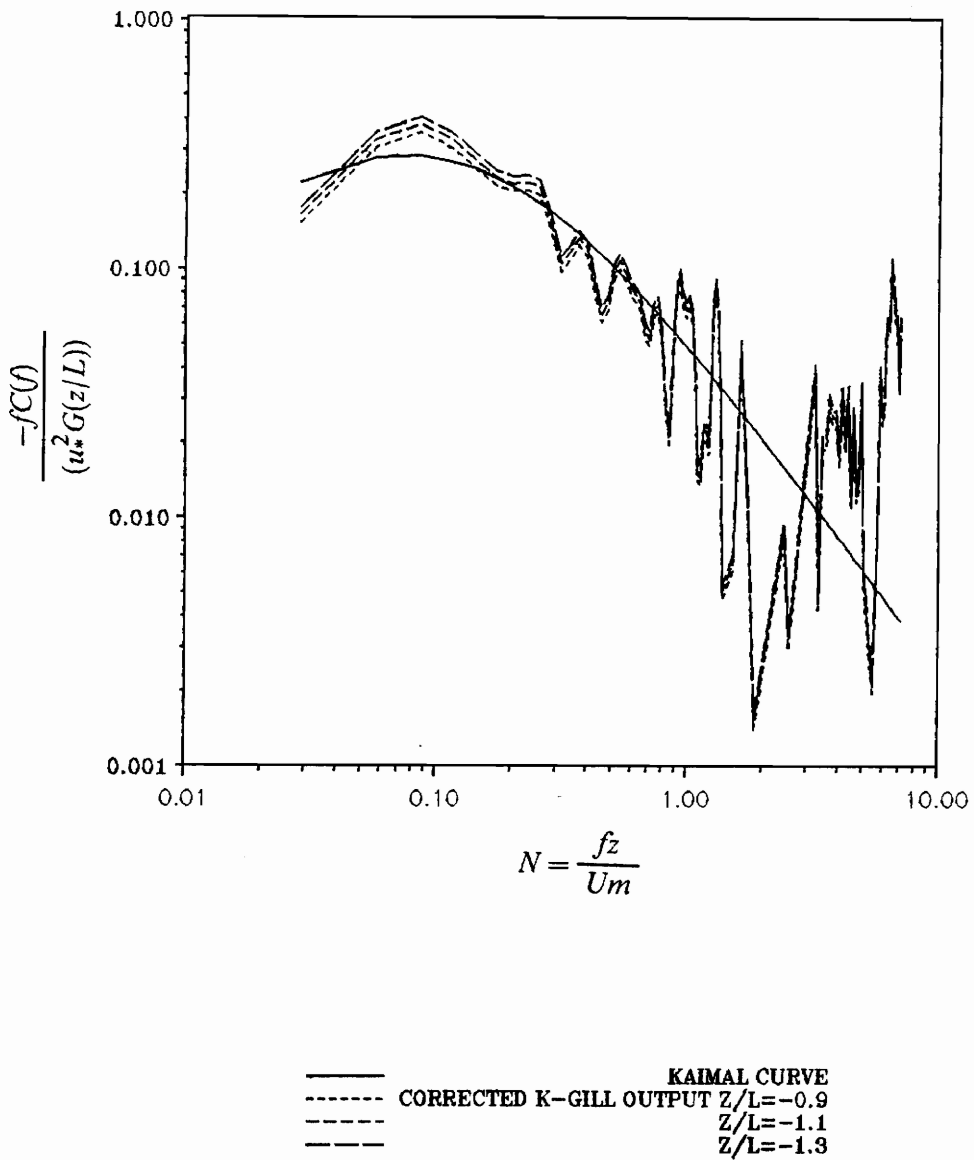


Figure 31. Comparison of the normalized cospectra at different stability conditions and Kaimal's result for data set #2.

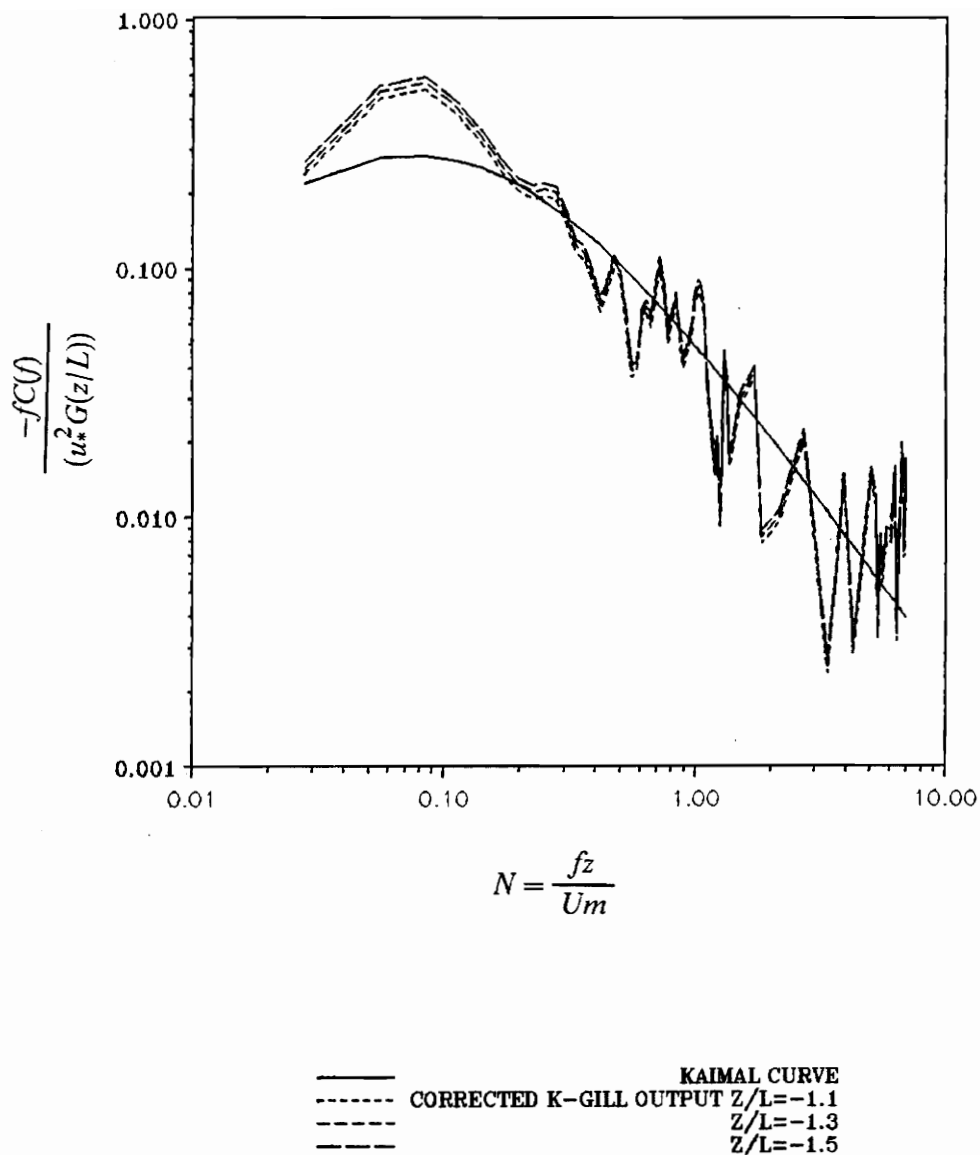


Figure 32. Comparison of the normalized cospectra at different stability conditions and Kaimal's result for data set #3.

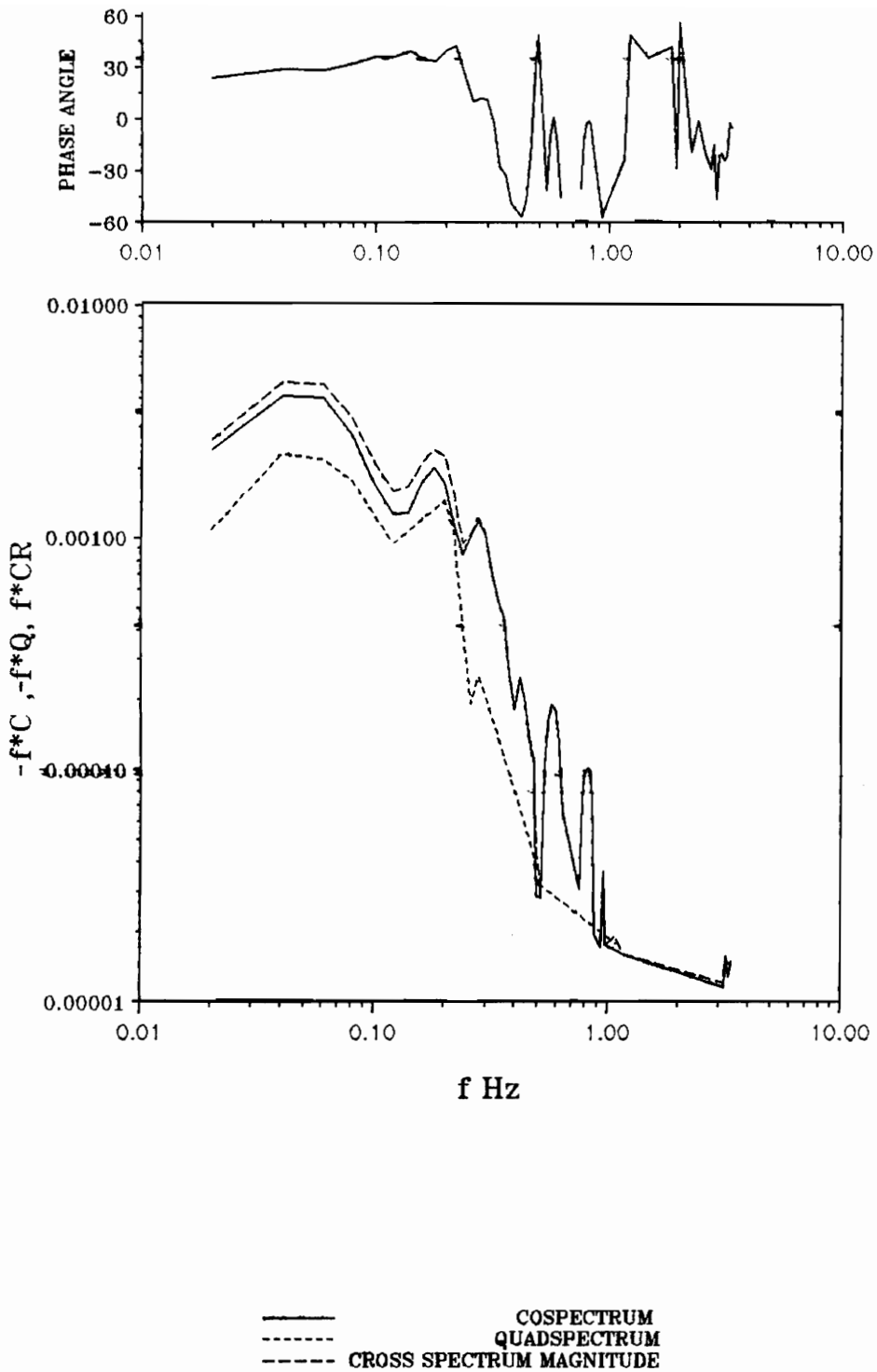


Figure 33. Comparison of the cospectrum, quadspectrum, magnitude of the cross spectrum, and the phase angle for data set #1.

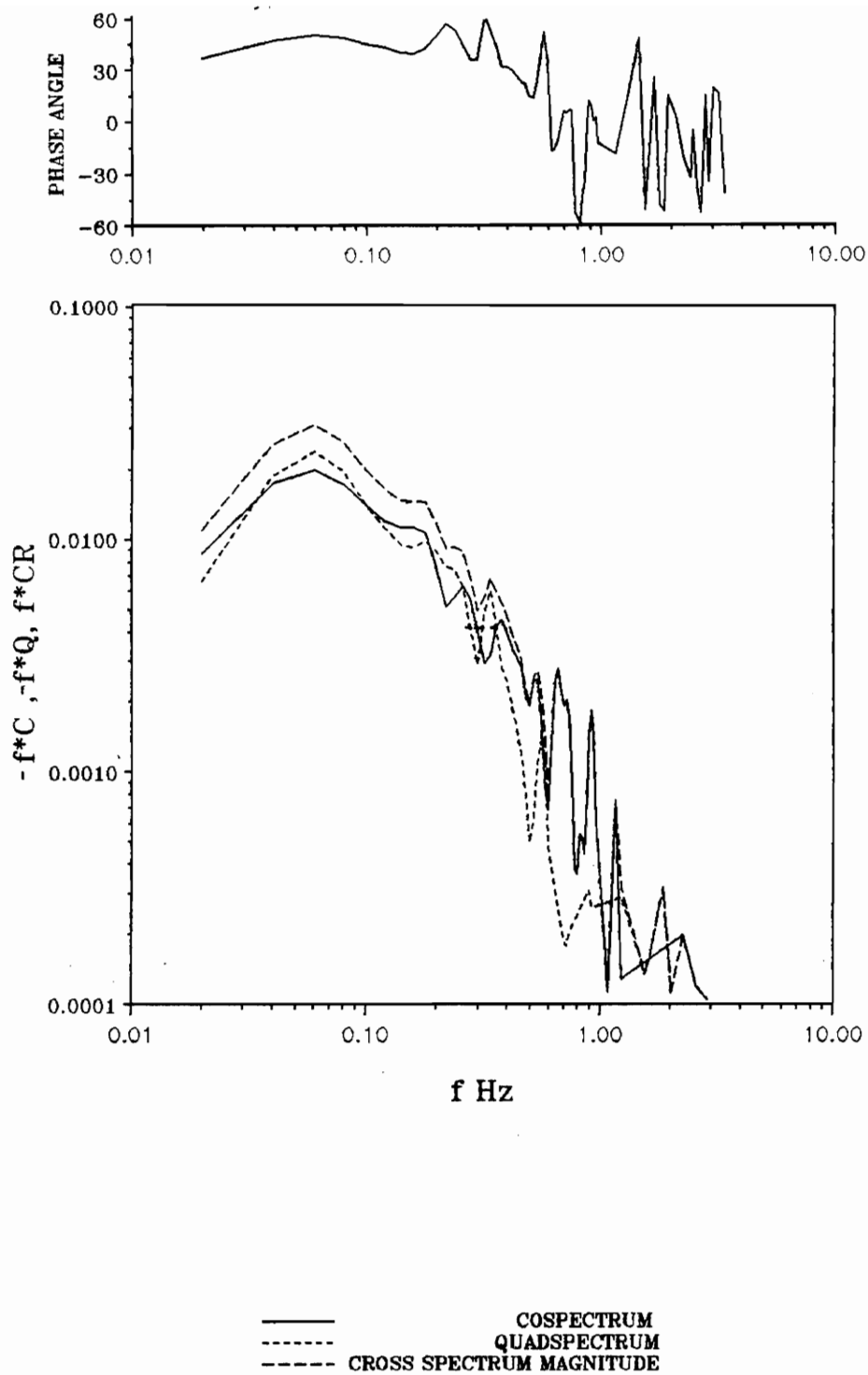


Figure 34. Comparison of the cospectrum, quadspectrum, magnitude of the cross spectrum, and the phase angle for data set #2.

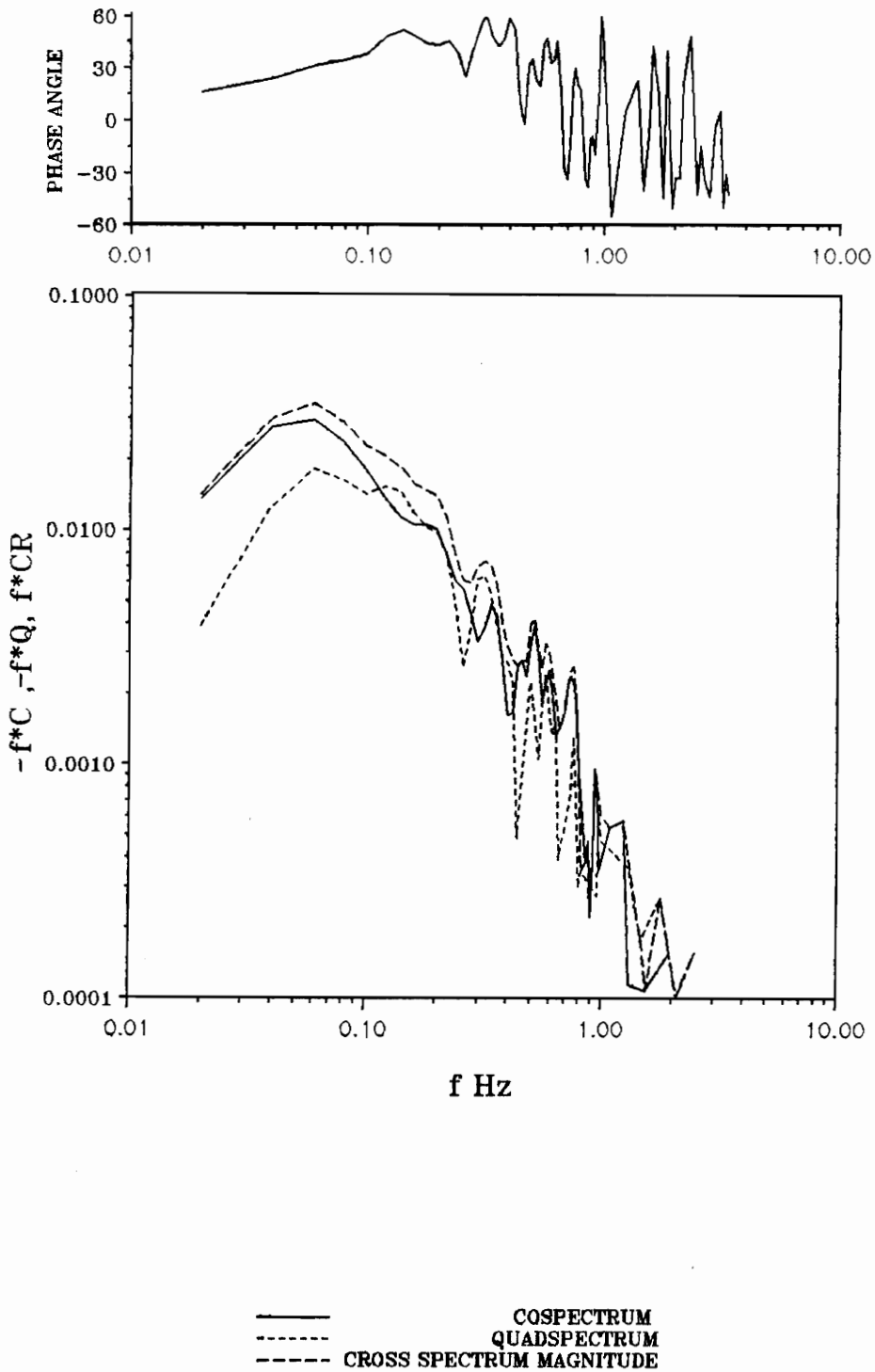


Figure 35. Comparison of the cospectrum, quadspectrum, magnitude of the cross spectrum, and the phase angle for data set #3.

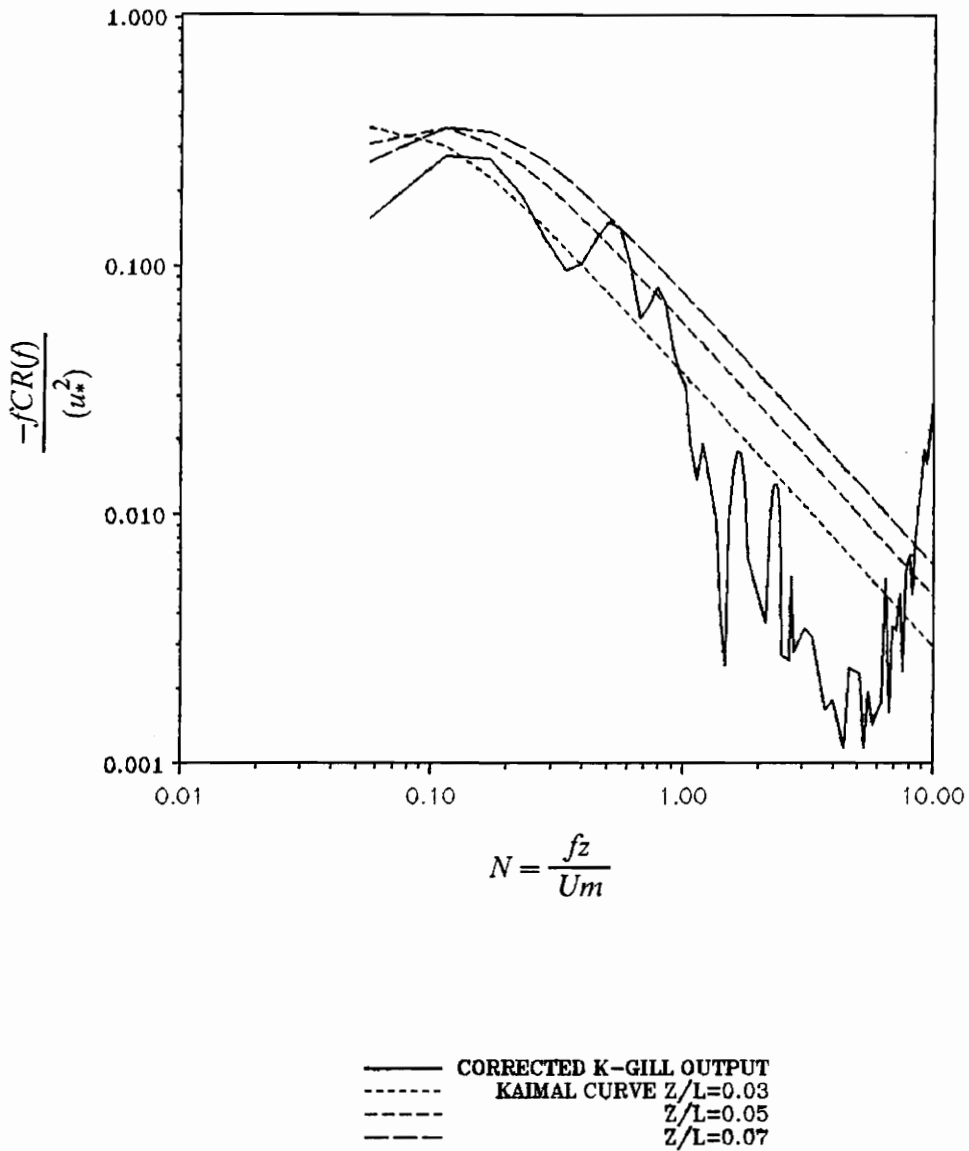


Figure 36. Comparison of the corrected normalized cospectra at different stability conditions and Kaimal's result for data set #1.

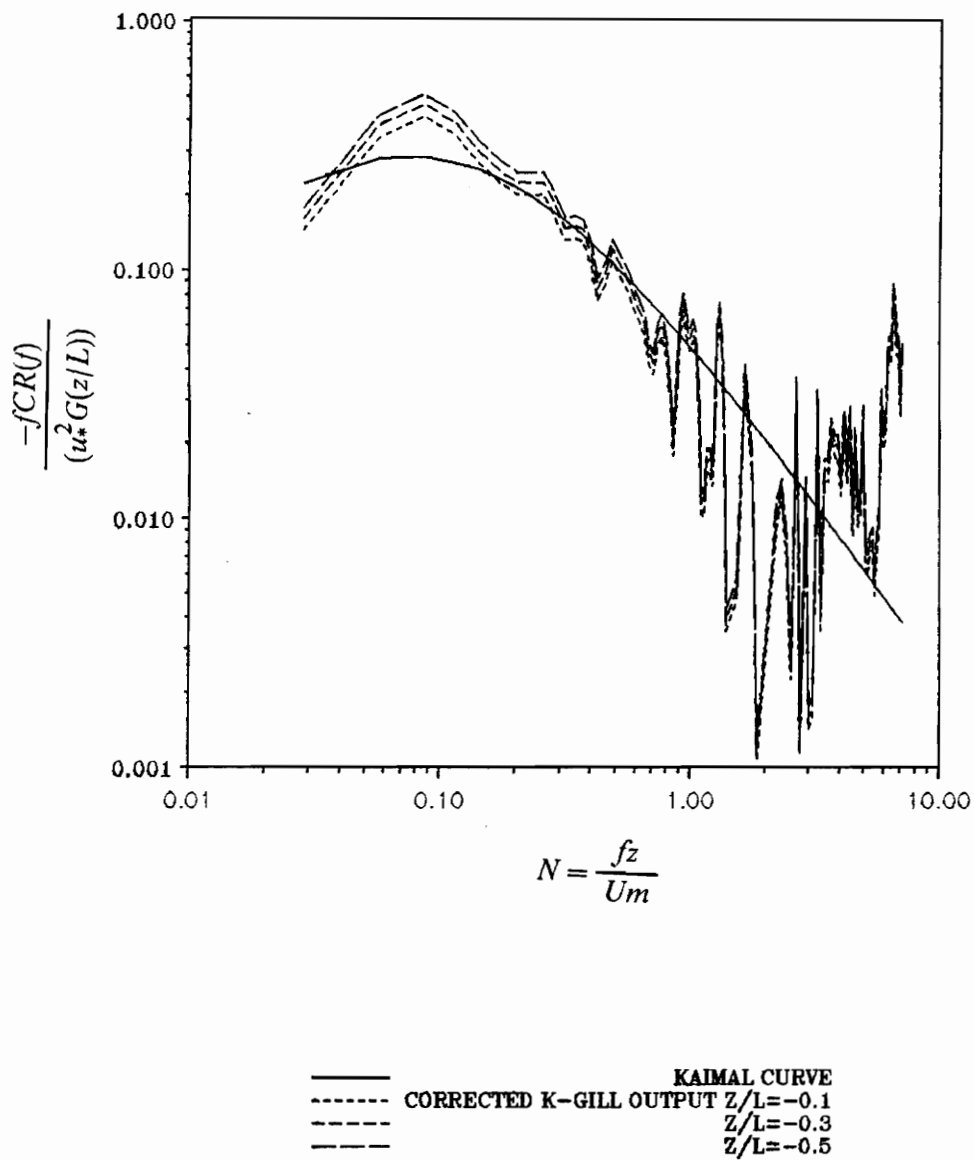


Figure 37. Comparison of the corrected normalized cospectra at different stability conditions and Kaimal's result for data set #2.

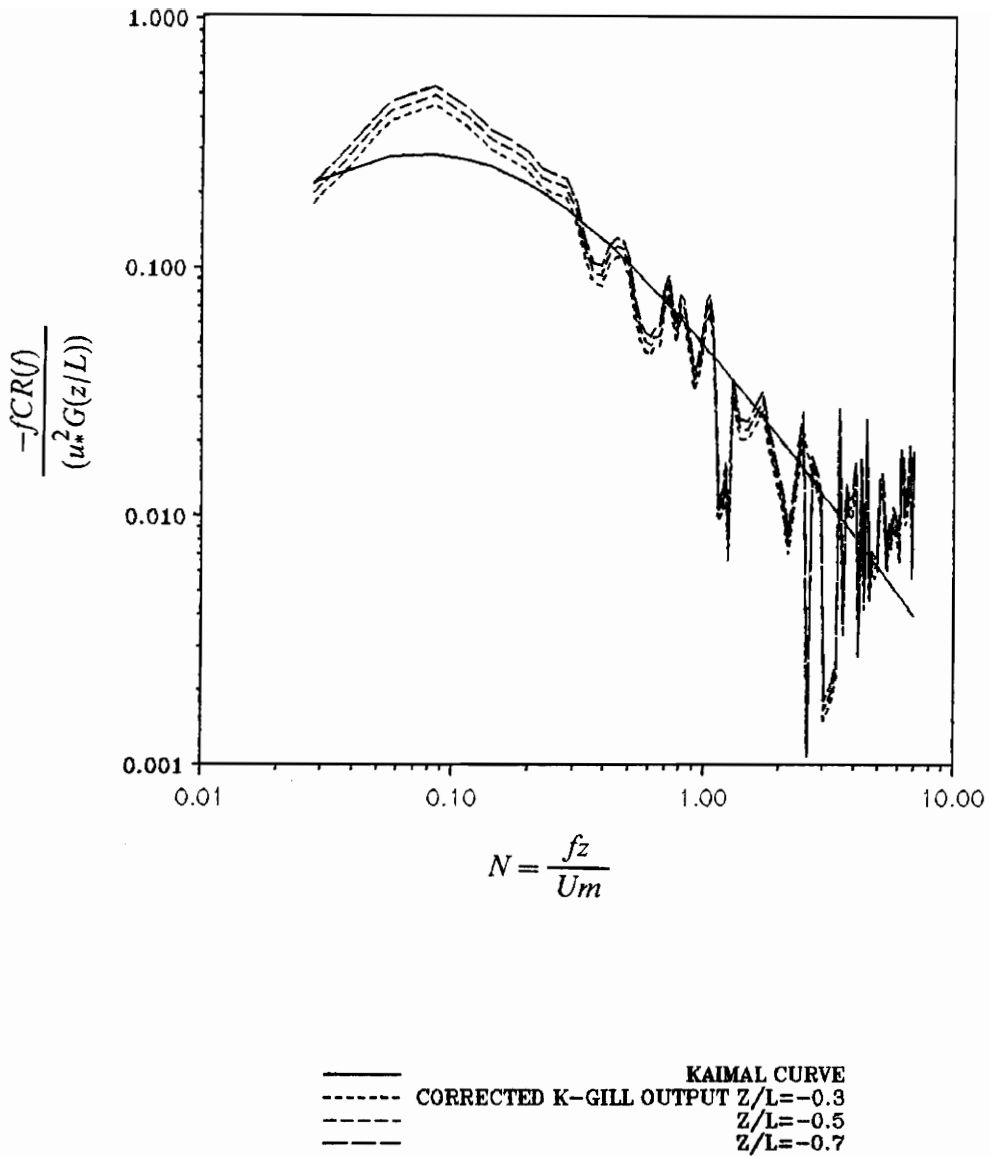


Figure 38. Comparison of the corrected normalized cospectra at different stability conditions and Kaimal's result for data set #3.

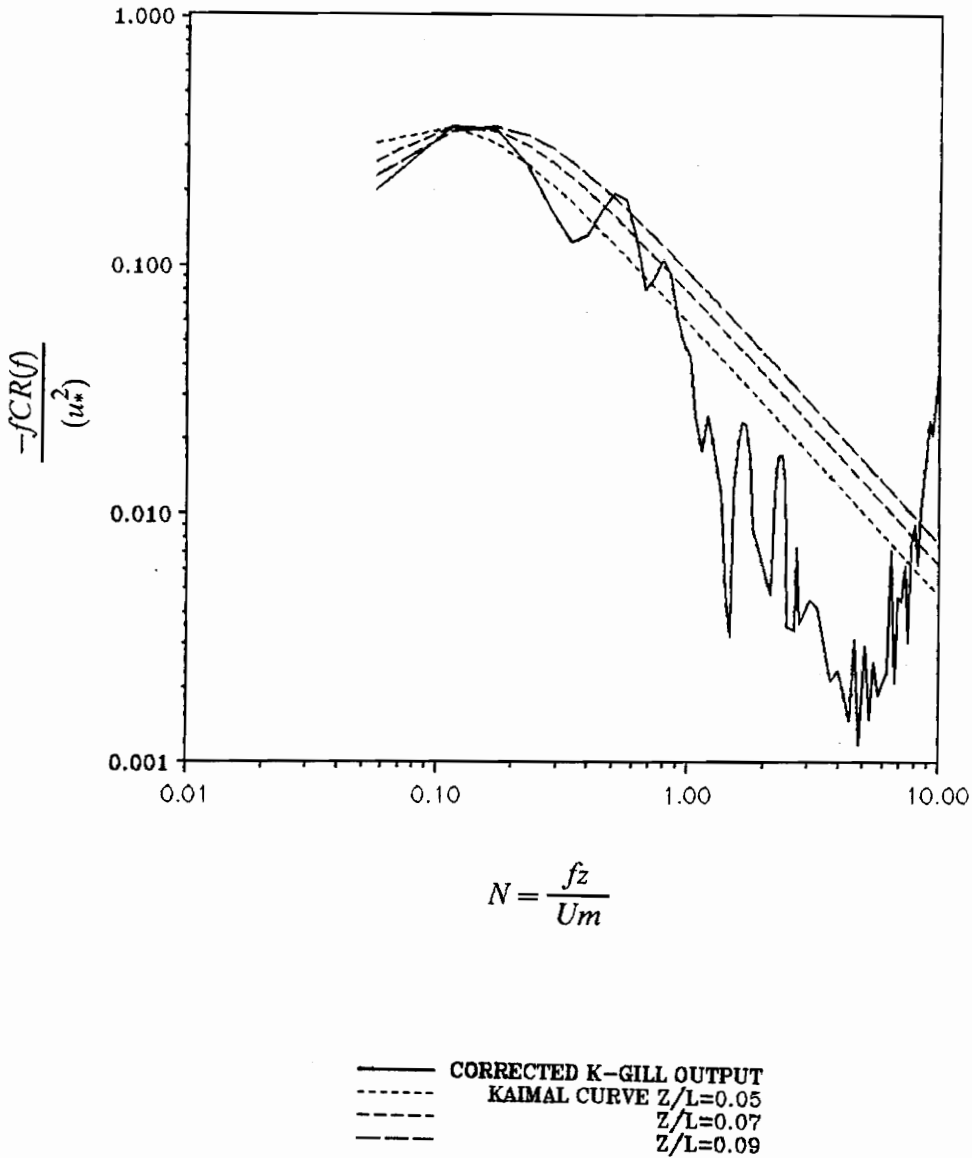


Figure 39. Comparison of the corrected normalized cospectra at different stability conditions and Kaimal's result for data set #1 with u_*^2 equals 0.0257.

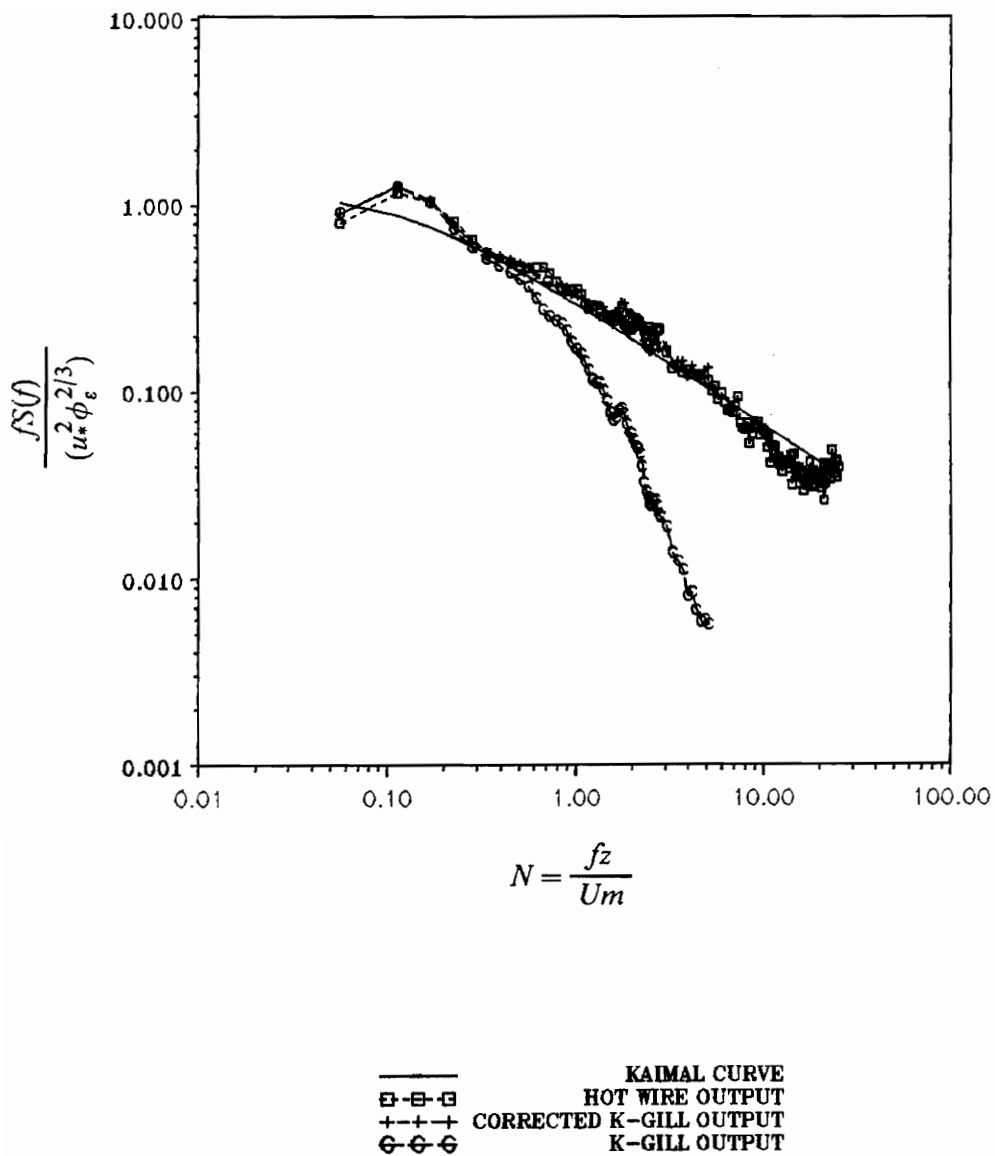


Figure 40. Comparison of the u spectra from measurement and from Kaimal *et al.* (1972) for data set #1.

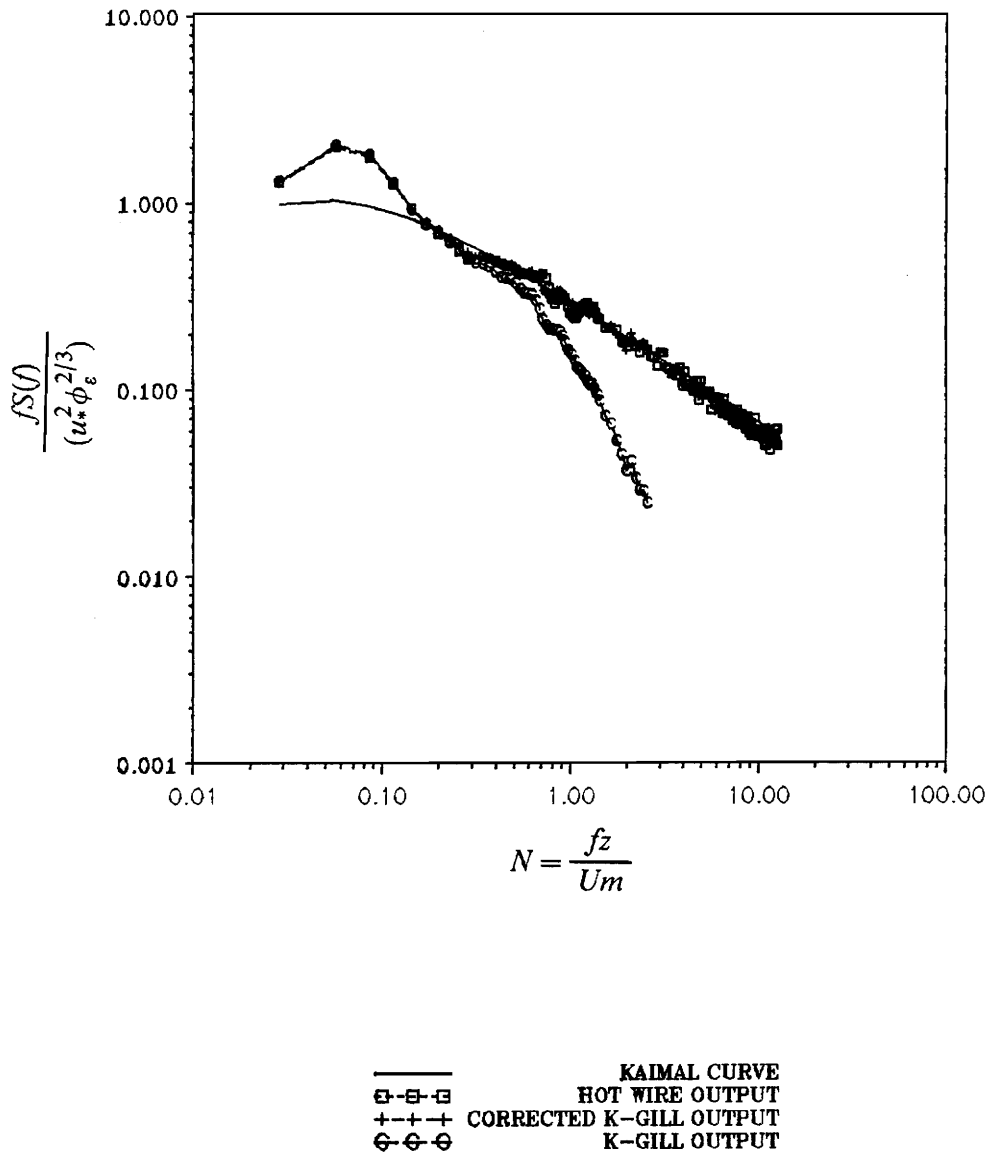


Figure 41. Comparison of the u spectra from measurement and from Kaimal *et al.* (1972) for data set #2.

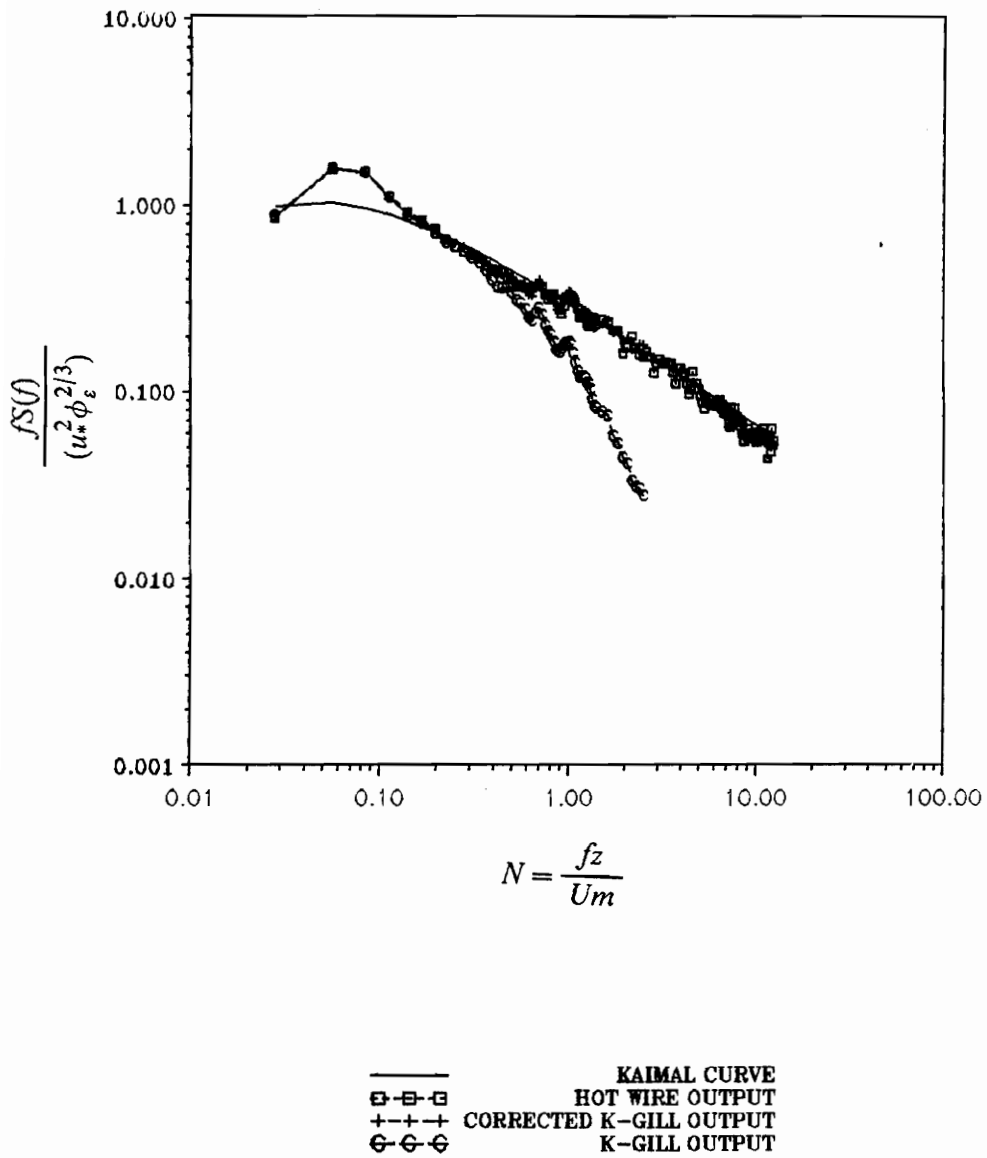


Figure 42. Comparison of the u spectra from measurement and from Kaimal *et al.* (1972) for data set #3.

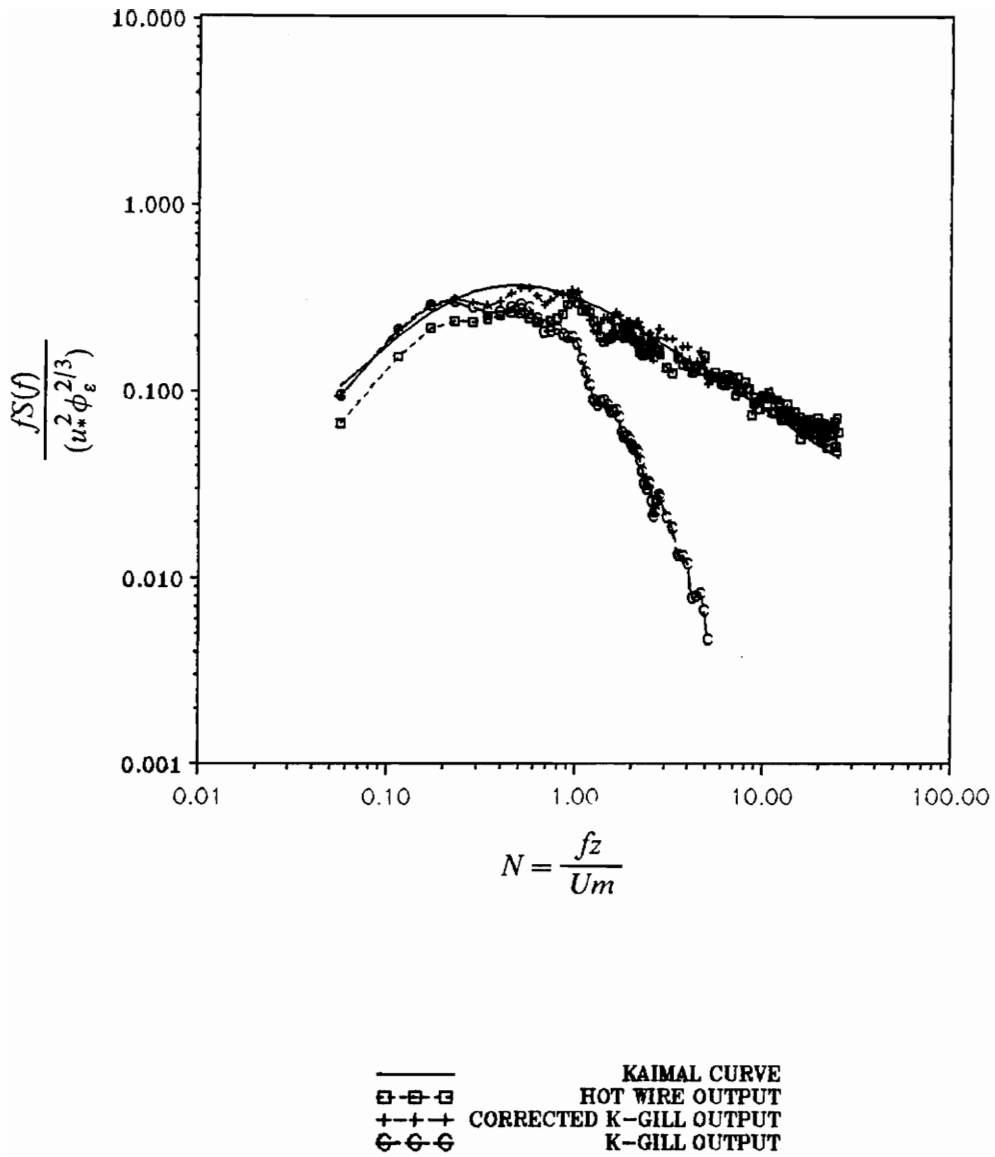


Figure 43. Comparison of the w spectra from measurement and from Kaimal *et al.* (1972) for data set #1.

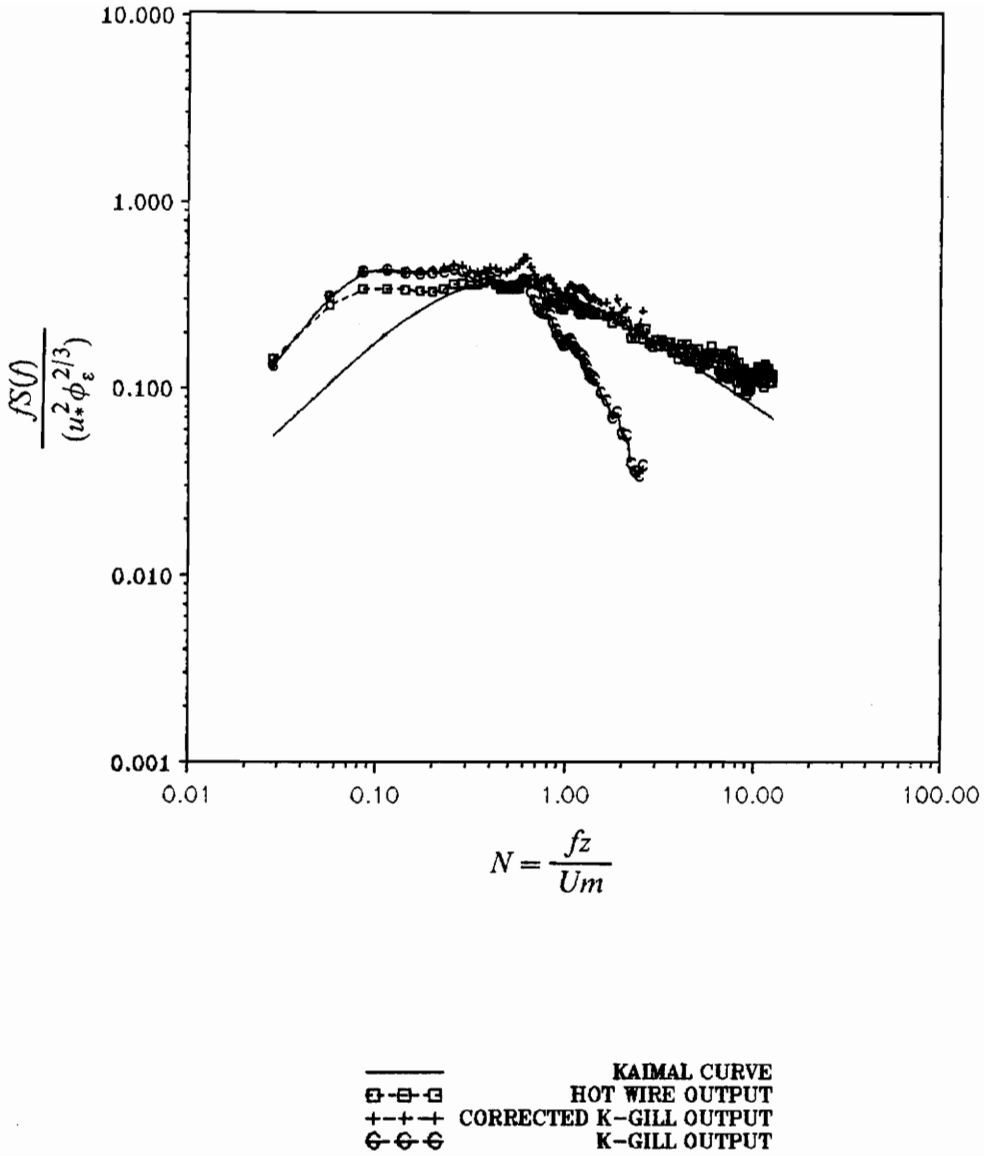


Figure 44. Comparison of the w spectra from measurement and from Kaimal *et al.* (1972) for data set #2.

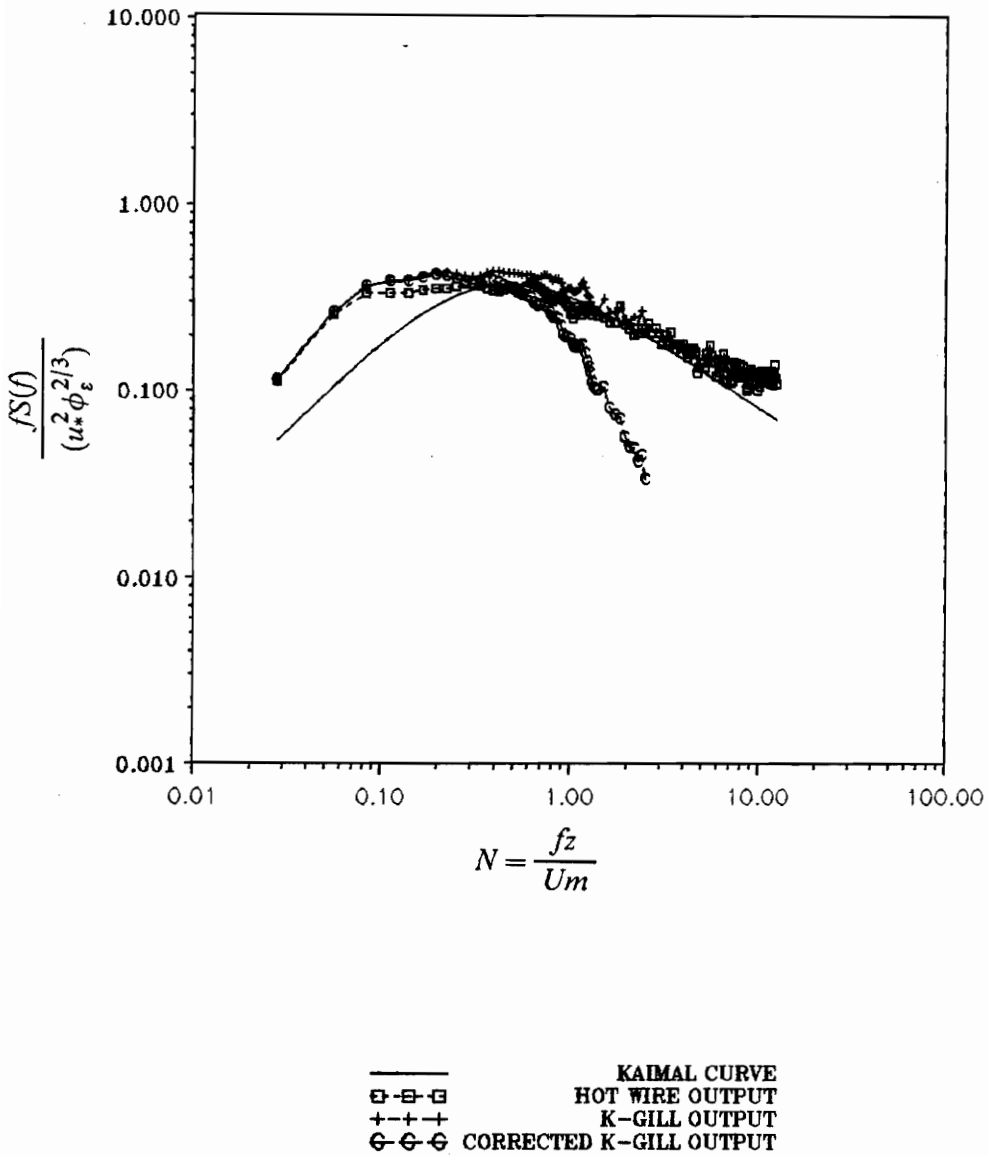


Figure 45. Comparison of the w spectra from measurement and from Kaimal *et al.* (1972) for data set #3.

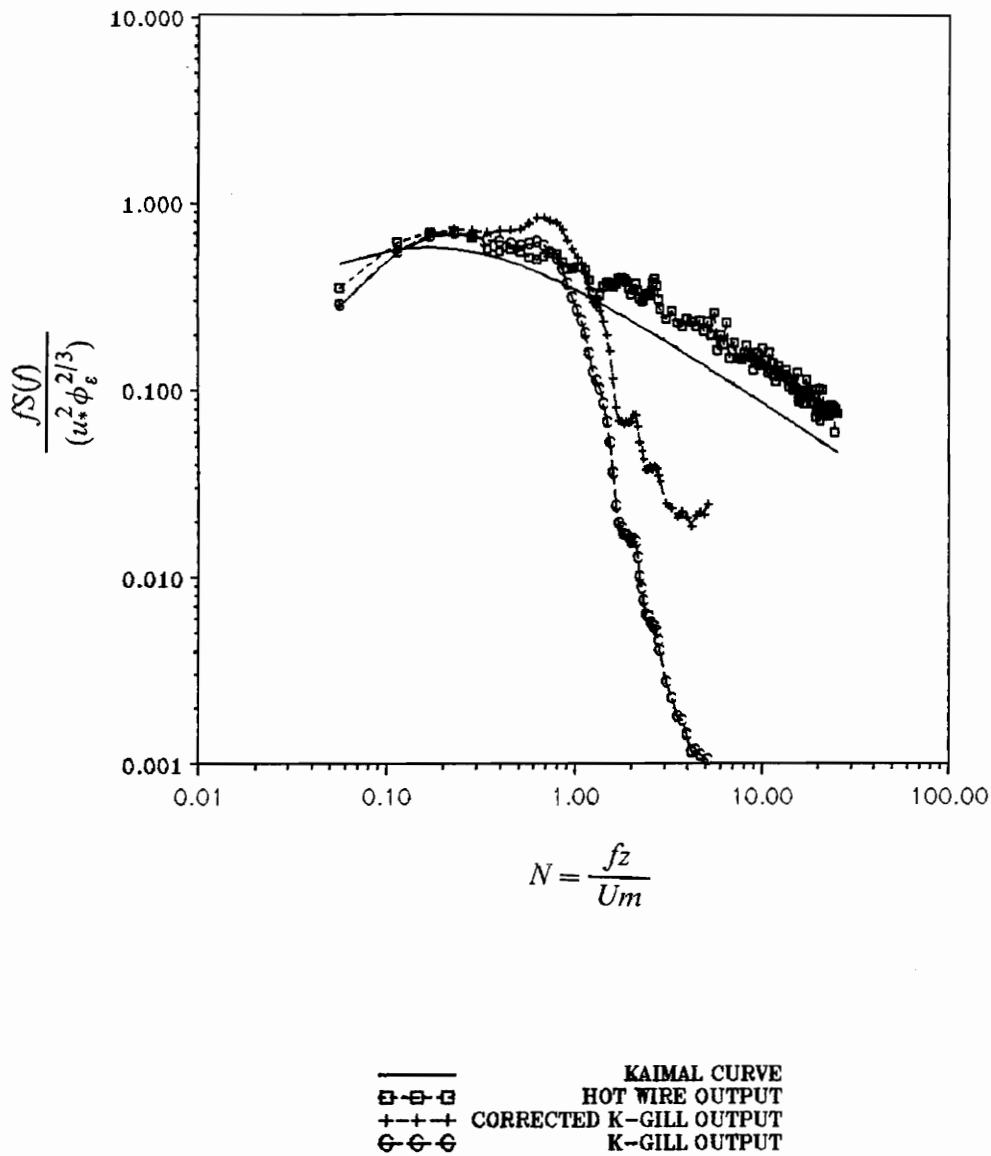


Figure 46. Comparison of the v spectra from measurement and from Kaimal *et al.* (1972) for data set #1.

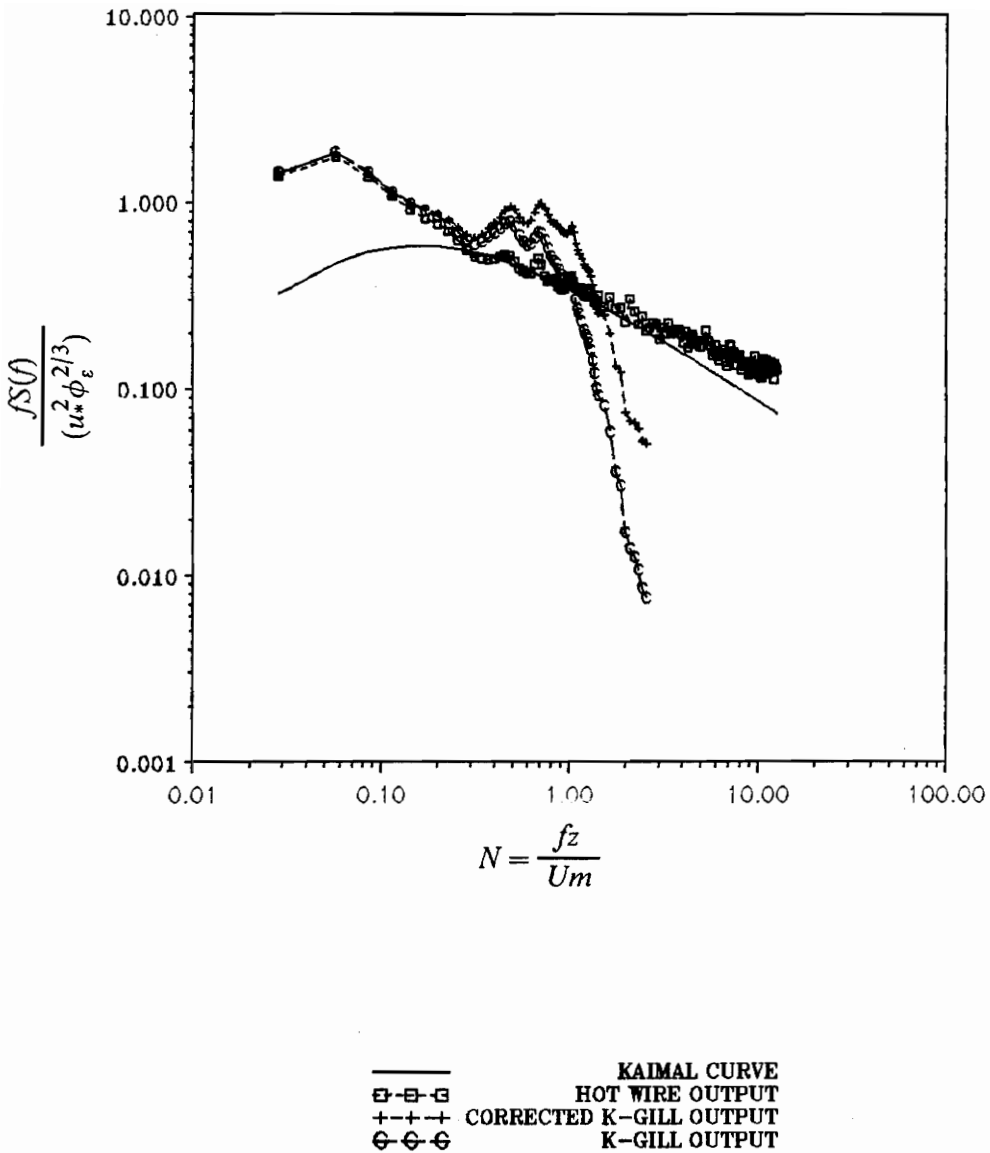


Figure 47. Comparison of the v spectra from measurement and from Kaimal *et al.* (1972) for data set #2.

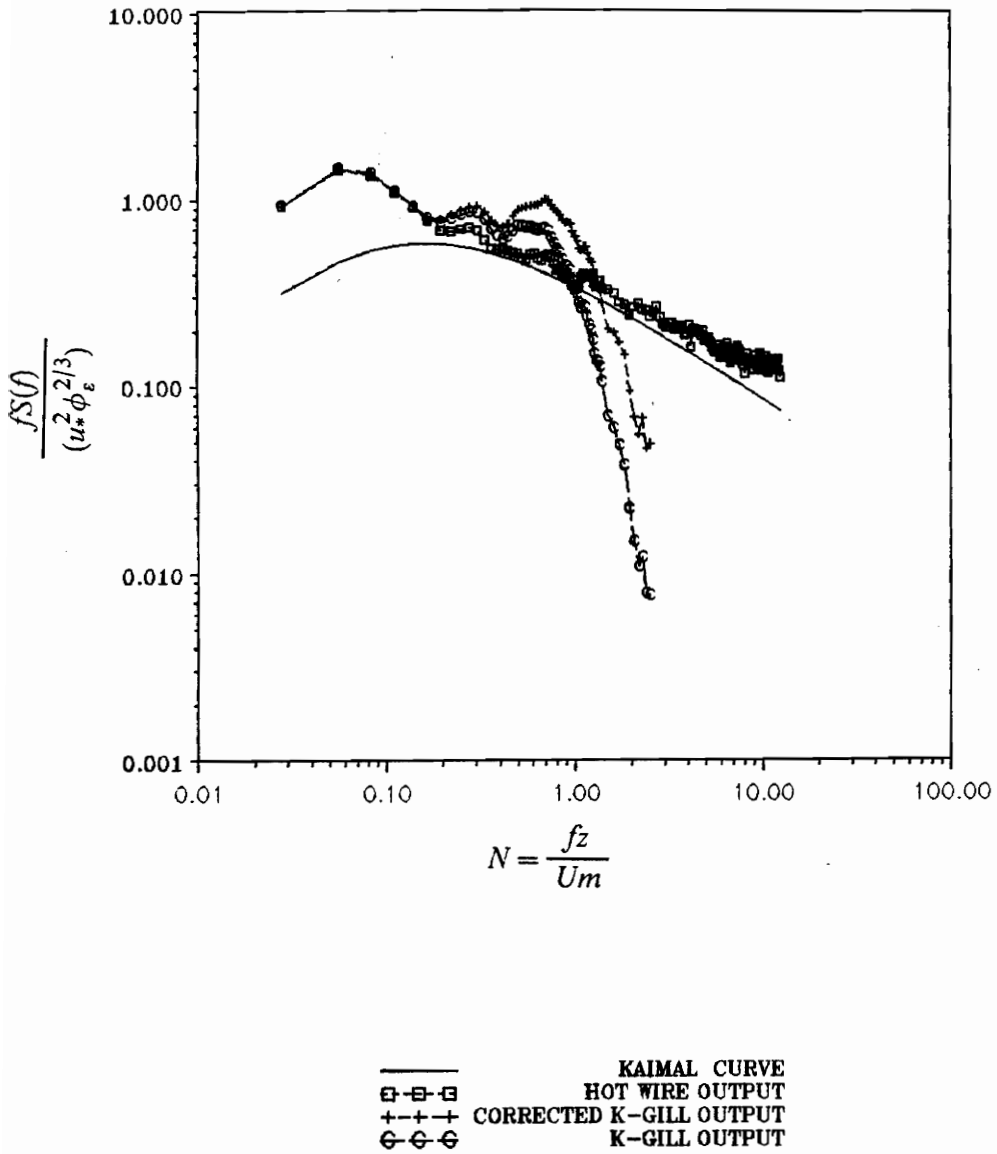


Figure 48. Comparison of the v spectra from measurement and from Kaimal *et al.* (1972) for data set #3.

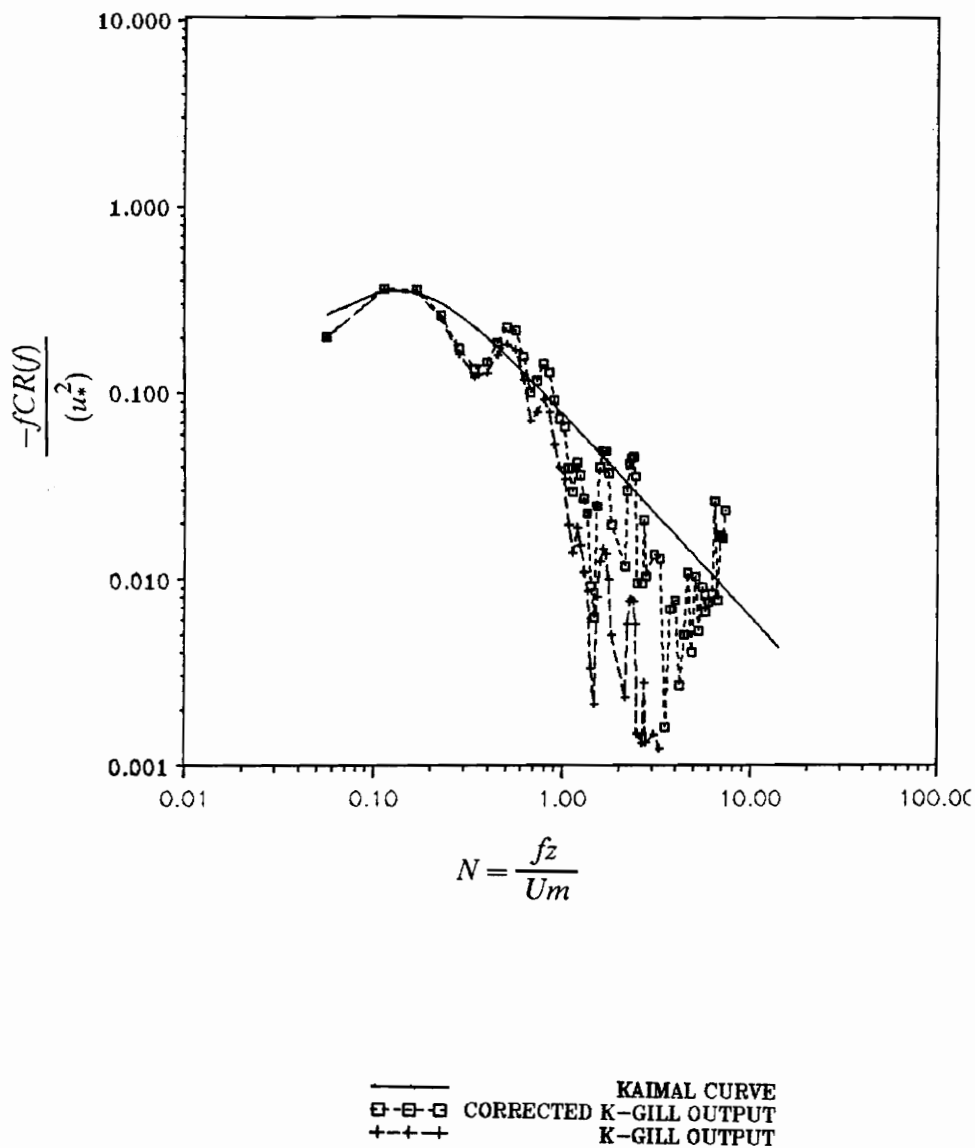


Figure 49. Comparison of the uw cospectra from measurement and from Kaimal *et al.* (1972) for data set #1.

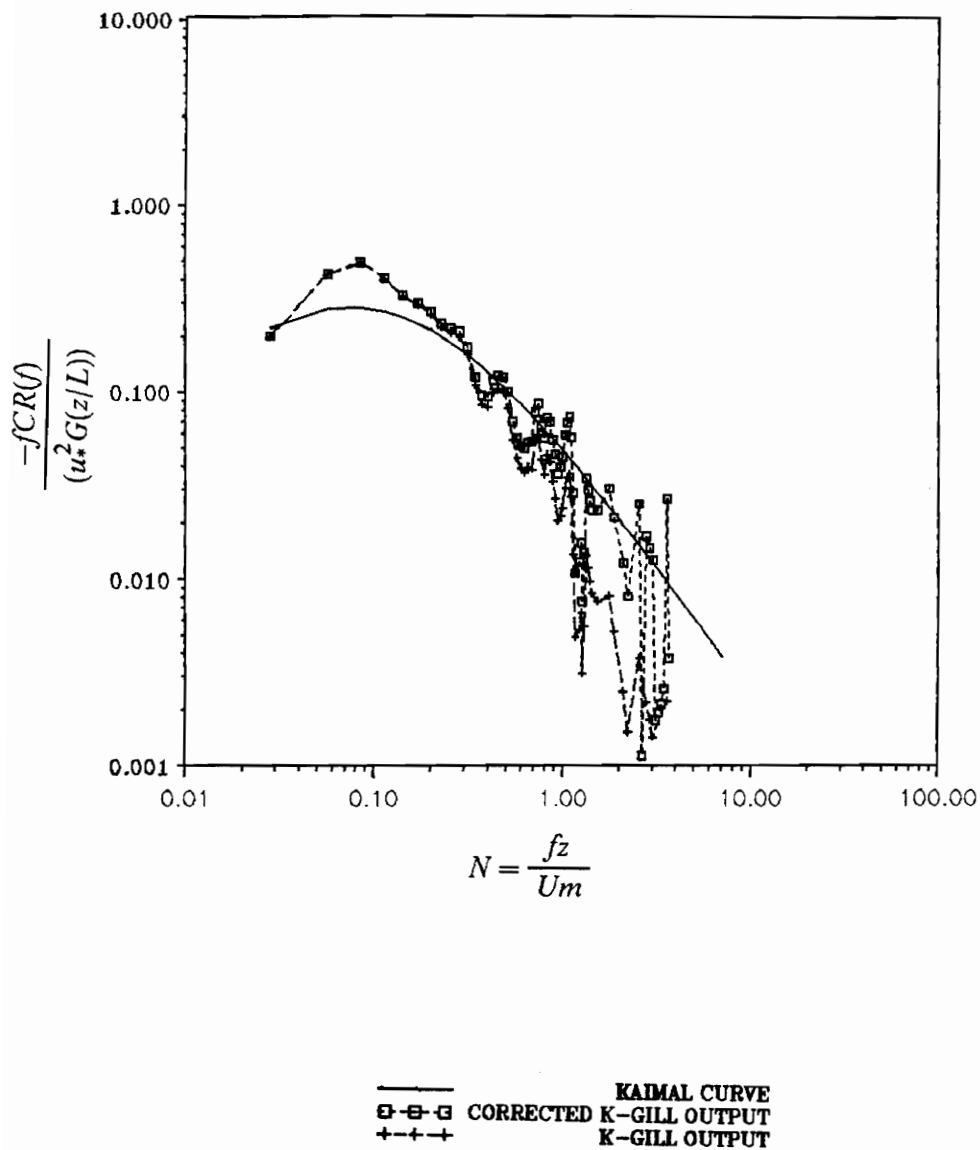


Figure 50. Comparison of the uw cospectra from measurement and from Kaimal *et al.* (1972) for data set #2.

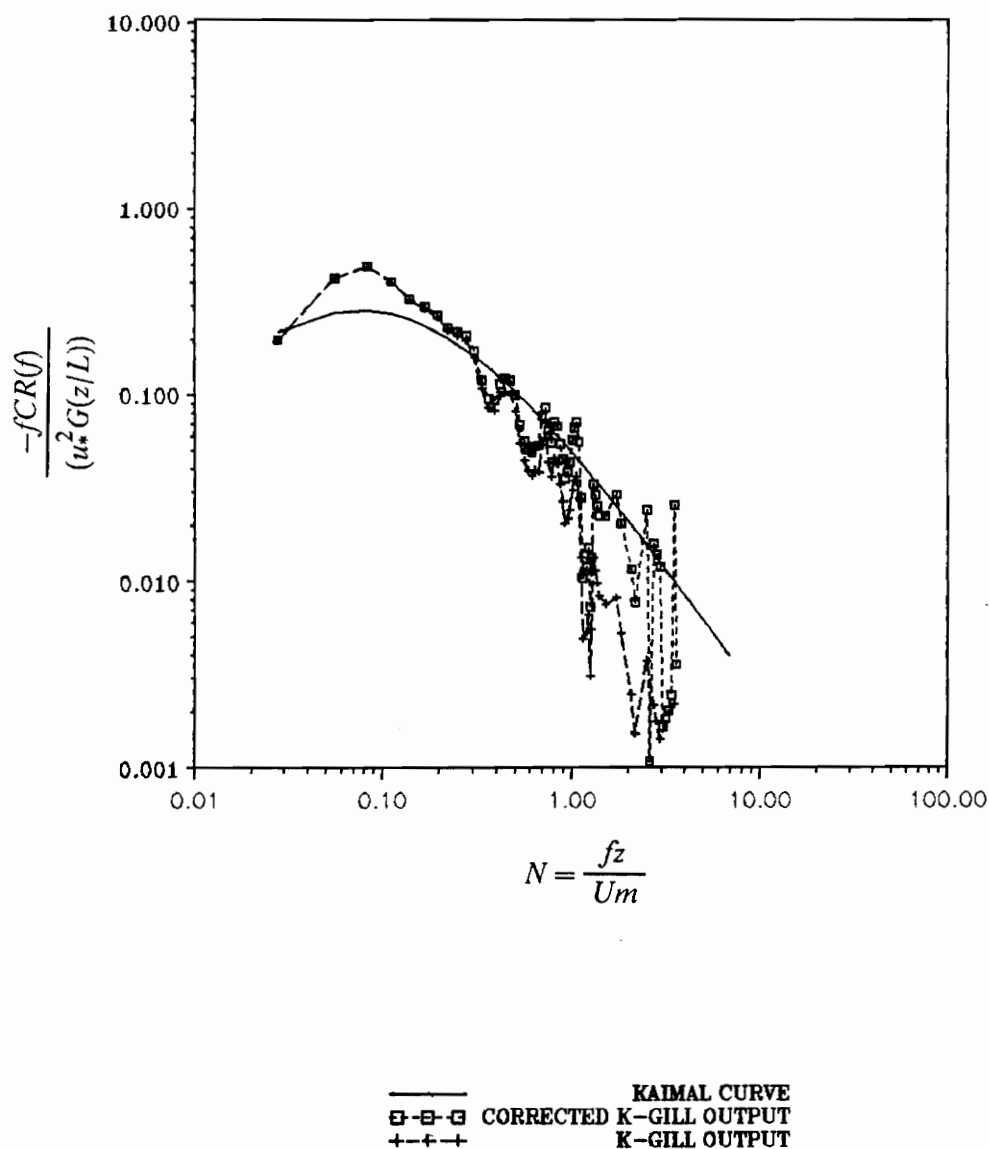


Figure 51. Comparison of the uw cospectra from measurement and from Kaimal *et al.* (1972) for data set #3.

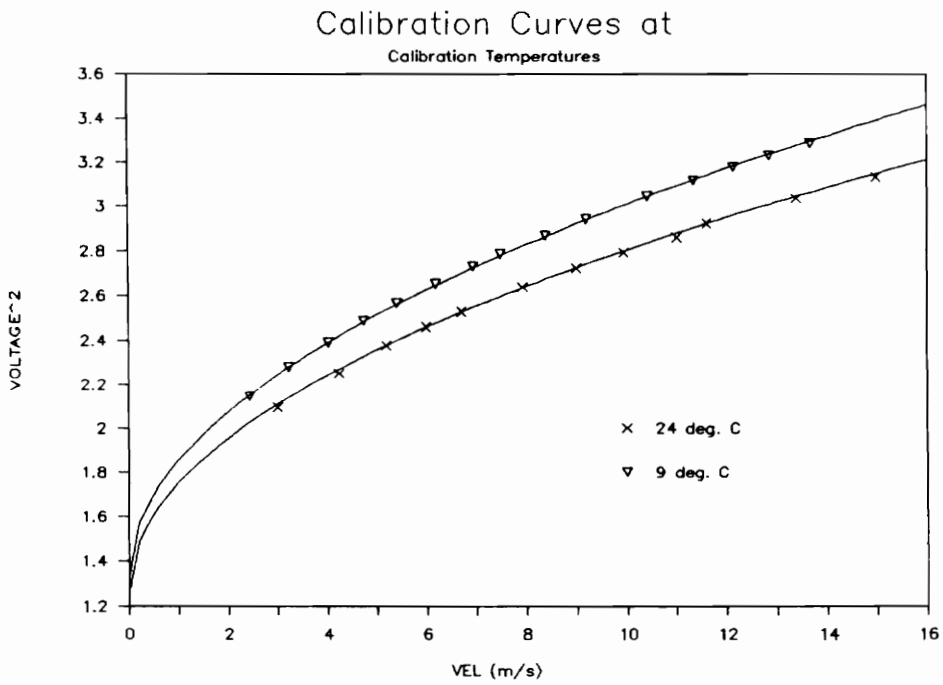


Figure A1. The calibrations of a hot-wire probe at different temperature.

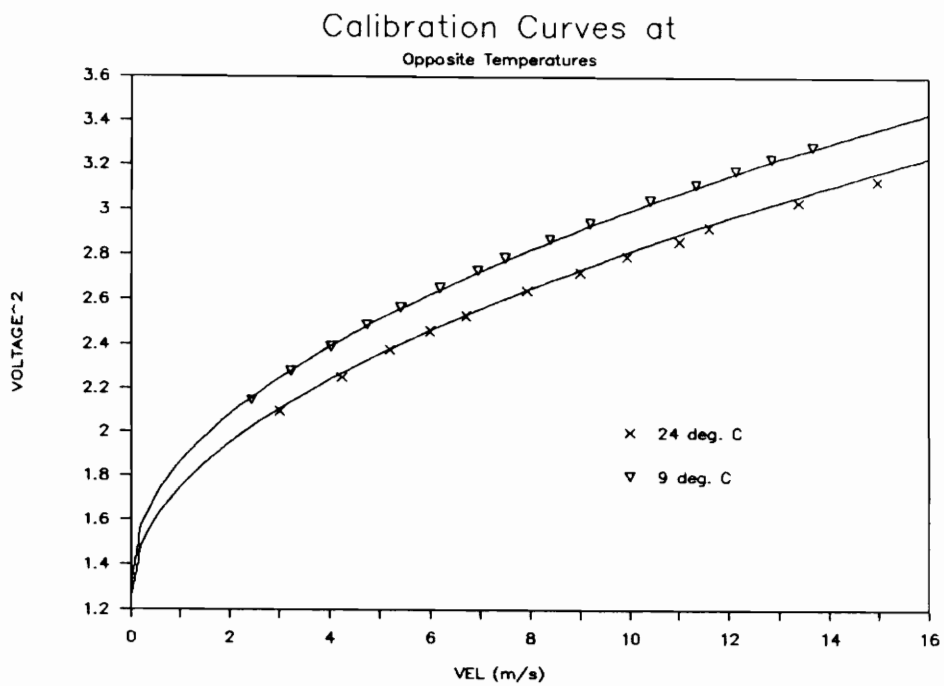


Figure A2. The temperature correction results at different temperature.

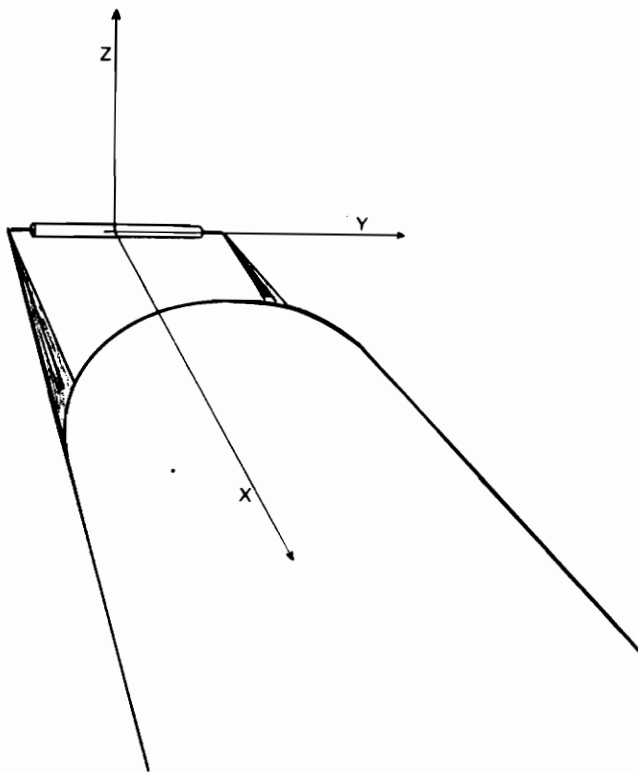


Figure A3. The wire coordinate system.

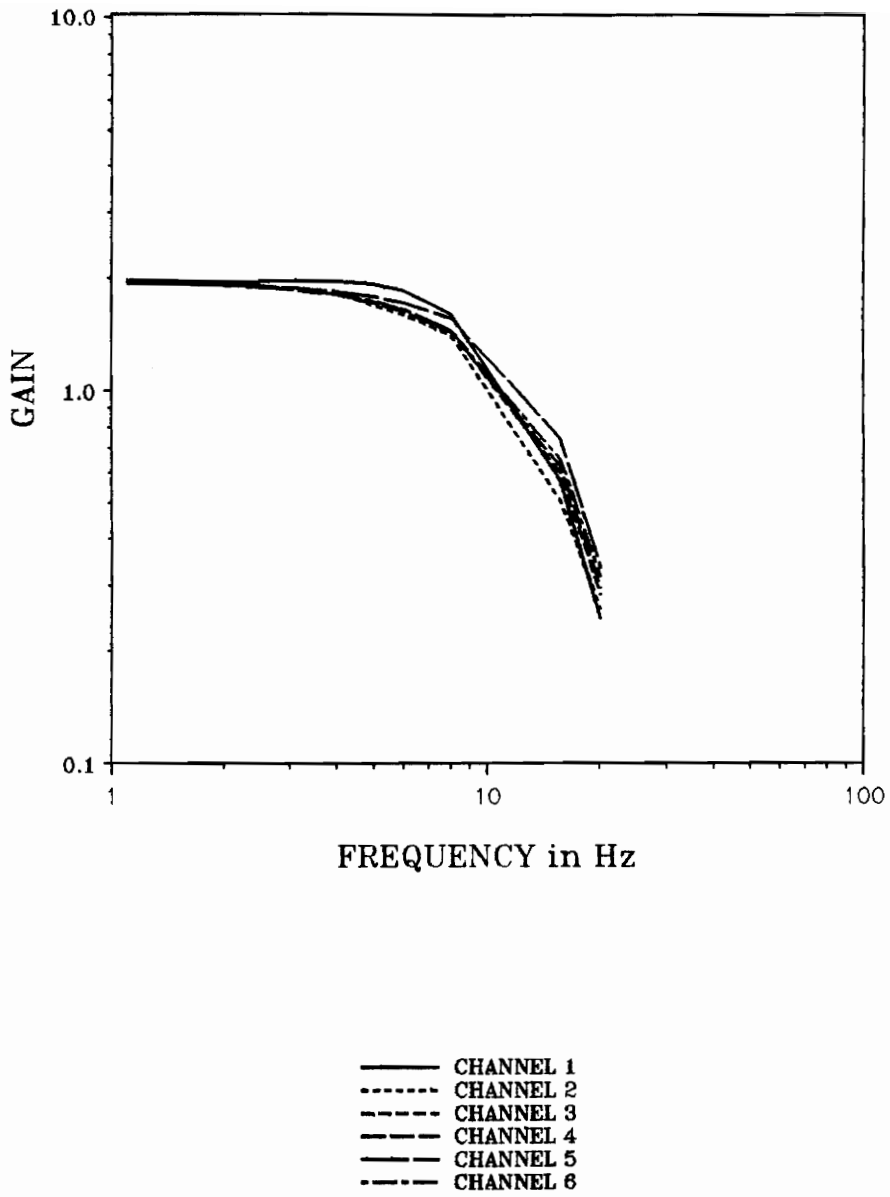


Figure A4. Frequency response of the four pole Bessel low pass filters.

Tables

Table 1 Error analysis of the K-Gill interpolation table

a. Error of the U component from the K-Gill table

α angle	Velocity in m/s							
	0.65	1.00	1.50	2.10	2.70	4.00	6.00	10.00
	error in %							
30.	16.53	1.70	0.63	0.04	0.02	0.01	-0.18	0.09
28.	12.09	3.16	0.66	-0.30	0.09	-0.11	0.06	0.11
26.	6.87	0.75	1.33	0.16	0.00	-0.49	0.03	0.07
24.	2.01	-0.74	0.80	0.18	-0.04	0.39	-0.21	-0.03
22.	-1.13	0.36	-0.45	0.02	-0.18	-0.25	0.15	0.08
20.	-4.23	0.08	0.99	-0.28	0.25	0.15	-0.65	0.03
18.	-5.89	1.01	0.86	0.96	0.20	0.66	0.62	0.40
16.	0.32	0.00	-0.16	-0.49	-0.23	-0.24	-0.78	-0.04
14.	-0.87	-0.42	-0.10	0.66	0.14	0.29	0.24	0.40
12.	0.46	-0.27	0.22	0.21	-0.01	0.08	-0.45	-0.24
10.	-0.91	-1.06	1.05	-0.27	0.03	0.25	0.21	0.20
8.	0.60	0.76	0.53	0.10	-0.22	0.16	-0.23	-0.03
6.	0.73	-0.30	0.61	-0.18	-0.09	-0.26	0.14	0.28
4.	-1.40	0.14	0.85	0.66	-0.15	0.07	-0.39	-0.18
2.	0.44	0.16	-0.04	0.25	0.34	0.02	0.21	0.35
0.	0.79	0.12	0.47	0.27	-0.45	0.01	-0.35	-0.18
-2.	0.10	0.13	-0.01	0.02	-0.04	-0.03	0.19	0.01
-4.	-0.21	0.05	-0.73	0.26	-0.19	0.34	-0.31	0.17
-6.	-0.15	0.20	0.06	0.27	-0.06	-0.31	0.02	0.26
-8.	-1.49	0.47	0.45	0.24	0.05	0.18	-0.08	-0.54
-10.	-1.80	0.09	0.04	-0.27	-0.08	0.14	0.00	0.51
-12.	0.11	-0.16	1.96	0.49	-0.22	0.12	-0.63	-0.10
-14.	2.05	-0.04	-0.21	0.46	-0.13	-0.11	0.03	0.09
-16.	0.98	-1.10	0.76	0.27	0.16	0.27	-0.12	0.17
-18.	-0.90	0.24	2.02	-0.11	0.05	0.30	-0.01	0.28
-20.	1.16	0.04	-1.08	0.29	-0.30	0.17	-0.19	-0.03
-22.	2.97	-0.22	0.79	0.03	0.08	-0.15	0.06	0.35
-24.	4.63	0.27	1.16	-0.11	-0.35	0.03	-0.80	-0.03
-26.	2.76	-0.21	-0.26	0.00	0.61	0.12	0.58	-0.02
-28.	-1.14	-0.88	0.16	0.29	-0.41	0.08	-1.16	0.04
-30.	5.49	-1.37	0.88	-0.01	-0.16	0.03	-0.08	-0.01

Table 1 Error analysis of the K-Gill interpolation table -- continued

b. Error of the W component from the K-Gill table

α angle	Velocity in m/s							
	0.65	1.00	1.50	2.10	2.70	4.00	6.00	10.00
	error in %							
30.	6.27	-2.09	0.30	-0.11	0.32	-0.05	0.25	-0.03
28.	8.54	-0.91	0.33	0.94	-0.13	0.14	0.25	0.03
26.	6.09	-0.94	-0.29	-0.63	0.28	-0.55	-0.30	-0.25
24.	3.65	0.10	-0.12	0.05	-0.12	-0.18	0.19	0.07
22.	0.72	0.74	-0.79	0.01	-0.17	0.07	-0.23	0.05
20.	-2.12	0.37	-0.02	0.11	0.60	-0.40	0.47	-0.08
18.	-2.82	0.42	-0.04	0.19	-0.13	0.07	0.20	0.09
16.	0.95	-0.07	0.58	-0.87	0.12	0.06	0.63	-0.01
14.	0.09	0.67	0.00	0.16	-0.05	0.20	-0.20	-0.06
12.	0.48	0.14	-0.08	-0.58	0.08	-0.38	0.35	0.19
10.	-1.01	-0.31	-0.18	0.13	-0.08	-0.21	-0.17	-0.20
8.	0.00	0.53	0.75	0.12	-0.14	0.07	0.03	-0.17
6.	1.07	-0.31	-0.36	-0.33	0.42	-0.50	-0.07	0.05
4.	0.00	0.28	-0.79	-0.40	-0.19	-0.03	0.03	-0.25
2.	0.56	0.23	0.09	0.12	0.41	0.10	0.04	-0.07
0.	-0.32	0.00	1.13	-0.19	-0.43	-0.03	0.12	0.11
-2.	0.17	-0.05	0.37	-0.17	0.31	0.03	-0.10	0.05
-4.	0.48	-0.01	-0.25	1.35	0.20	-0.06	0.15	0.09
-6.	0.06	0.32	0.02	0.51	-0.20	0.11	0.06	0.11
-8.	0.45	1.12	0.10	-0.04	-0.48	-0.19	0.00	0.17
-10.	-0.54	-0.09	0.61	0.35	0.12	0.58	0.19	-0.09
-12.	-1.28	0.22	0.01	-0.06	0.46	-0.12	-0.79	0.05
-14.	-1.95	-0.21	0.15	0.29	0.18	0.07	0.39	0.02
-16.	0.34	1.94	-0.16	-0.20	-0.35	-0.10	-0.26	-0.12
-18.	-0.31	1.04	-0.52	0.43	-0.19	-0.13	-0.16	-0.01
-20.	-3.21	0.43	1.41	-0.03	0.10	0.31	0.03	0.00
-22.	-5.82	-0.15	0.66	0.16	-0.18	0.02	0.06	0.05
-24.	-7.37	-0.19	-0.35	0.46	-0.16	0.02	-0.36	-0.04
-26.	-5.98	-0.53	0.48	0.09	-0.31	0.10	0.18	0.10
-28.	5.33	1.33	-0.07	-0.06	-0.05	0.07	-0.21	0.07
-30.	12.45	0.71	0.37	0.12	-0.17	0.03	-0.20	0.01

Table 2 Calibration accuracy of the hot-wire system in voltage and velocity components

RMS error in velocity components (percent)

Vel. components	error in %
U component	11.103
V component	8.327
W component	11.814

RMS error in voltage (percent)

Probe No.	error in %
Probe #1	0.93
Probe #2	1.11
Probe #3	1.05

Table 3 Mean wind vectors and variances for different data sets

	Data Set	No.1	No.2	No.3
HOT WIRE JIG	Um =	3.4375	6.9830	7.0453
	$\gamma =$	0.692	-1.944	6.465
	$\alpha =$	-5.767	-1.135	-0.969
	$\sigma_u =$	0.171	1.120	1.062
	$\sigma_w =$	0.053	0.338	0.395
	$-\overline{uw} =$	0.013	0.042	0.070
K-GILL	Um =	3.179	6.3327	6.4746
	$\gamma =$	4.288	7.417	12.910
	$\alpha =$	-2.006	1.253	0.954
	$\sigma_u =$	0.137	0.867	0.829
	$\sigma_w =$	0.034	0.244	0.263
	$-\overline{uw} =$	0.021	0.117	0.138

Table 4 Distance constant and frequency constants for different data sets

Data Set		No.1	No.2	No.3
Mean velocity	U_m	3.179	6.3327	6.4746
Frequency const.	f_1	0.3751	0.7481	0.7693
Distance const.	l	1.3488	1.3473	1.3395

Table 5 u_*^2 estimates

a. Neutral condition

Data set	No.1	No.2	No.3
Mean velocity	3.179	6.3327	6.4746
	value of u_*^2		
Measured – \overline{uw}	0.0219	0.1184	0.1408
Dissipation Method	0.0472	0.1618	0.1876
$\frac{\sigma_w}{u_*}$ Relation	0.0257	0.1813	0.1959

b. Stability correction results³

Data Set	No.1		
	value of u_*^2		
Measured – \overline{uw}	0.0220	0.0226	0.0230
Dissipation Method	+10%	Min.	-10%
	0.041	0.036	0.033
Stability Index z/L	0.01	0.03	0.05

Data Set	No.2		
	value of u_*^2		
Measured – \overline{uw}	0.1184	0.1184	0.1184
Dissipation Method	+10%	Min.	-10%
	0.1135	0.1054	0.0986
Stability Index z/L	-0.7	-0.9	-1.1

Data Set	No.3		
	value of u_*^2		
Measured – \overline{uw}	0.1408	0.1408	0.1408
Dissipation Method	+10%	Min.	-10%
	0.0859	0.0808	0.0764
Stability Index z/L	-1.1	-1.3	-1.5

³ For the dissipation method, the minimum (Min.) difference condition and $\pm 10\%$ point of the minimization process are shown. The fractional response corrections for the second and third data sets are neutral condition values.

Table 5 u_*^2 estimation -- continued

c. Consider the magnitude of the cross spectrum

Data Set	No.1		
	value of u_*^2		
Measured $-\overline{uw}$	0.0226	0.0228	0.0237
Dissipation Method	+ 10%	Min.	-10%
	0.036	0.033	0.031
Stability Index z/L	0.03	0.05	0.07
Data Set	No.2		
	value of u_*^2		
Measured $-\overline{uw}$	0.1184	0.1184	0.1184
Dissipation Method	+ 10%	Min.	-10%
	0.1518	0.1358	0.1235
Stability Index z/L	-0.1	-0.3	-0.5
Data Set	No.3		
	value of u_*^2		
Measured $-\overline{uw}$	0.1408	0.1408	0.1408
Dissipation Method	+ 10%	Min.	-10%
	0.1575	0.1432	0.1317
Stability Index z/L	-0.3	-0.5	-0.7
$u_*^2 = 0.0257$			
Data set	No.1		
	value of u_*^2		
Measured $-\overline{uw}$	0.0226	0.0228	0.230
Stability Index z/L	0.05	0.07	0.09

Table A1 Calibration results of the hot-wire jig system

	No.1	No.2	No.3
Probe serial No.	D649	M662	8370
A_0	5.66	6.25	5.52
B_0	2.14	1.69	2.15
n	0.511.	0.574	0.494
a_k	0.203	0.175	0.148
b_k	-0.0069	-0.0014	0.0016
K_1	1.127	1.196	1.108

Table A2 Calibration uncertainty of the U components in percent

Yaw angle	Velocity in m/s							
	2.2	3.6	5.1	6.4	8.7	11.0	12.9	
		uncertainty in %						
-60	-1.3	8.1	0.2	1.0	1.6	1.0	1.9	
-45	-10.1	6.0	-3.5	-5.6	1.9	-1.3	0.9	
-30	5.5	9.5	-9.6	-6.5	-12.3	-7.1	-3.2	
-15	4.4	13.2	-12.0	-0.5	-1.7	-5.2	-3.4	
0	3.6	11.8	-10.6	0.3	-0.9	-4.6	-2.6	
15	5.2	11.1	2.7	0.1	-4.0	-5.3	-5.2	
30	1.5	6.6	-12.4	-6.8	-4.3	-6.5	-6.9	
45	-2.3	2.3	-12.7	-7.5	-6.7	-8.7	-9.8	
60	-7.1	-4.9	-8.4	-7.8	-9.6	-9.4	-11.8	

Table A3 Calibration uncertainty of the V components in percent

Yaw angle	Velocity in m/s						
	2.2	3.6	5.1	6.4	8.7	11.0	12.9
	uncertainty in %						
-60.	3.1	11.0	-3.3	-9.8	-2.2	-5.8	-2.2
-45.	24.1	23.6	2.0	-3.1	-0.5	-2.9	-0.4
-30.	13.1	23.9	2.0	-0.4	11.7	1.5	1.6
-15.	15.6	16.7	4.7	5.6	2.2	0.1	-0.5
0.	4.9	6.9	2.7	4.4	0.9	-0.9	-0.7
15.	-2.3	-2.1	1.1	1.0	0.1	-1.4	-0.5
30.	-5.0	-7.3	0.5	-0.7	-1.6	-1.1	-1.3
45.	-6.7	-11.8	3.0	-1.0	-2.8	-3.1	-4.0
60.	-9.9	-19.6	8.0	-0.3	-7.5	-4.5	-7.6

Table A4 Calibration uncertainty of the W components in percent

Yaw angle	Velocity in m/s uncertainty in %						
	2.2	3.6	5.1	6.4	8.7	11.0	12.9
-60.	2.1	-4.9	1.8	-0.7	-8.7	0.0	-1.4
-45.	-46.6	-34.0	-20.2	-17.0	-13.9	-10.7	-9.2
-30.	-19.7	-29.6	-17.2	-15.0	-28.9	-15.1	-11.7
-15.	-15.5	-15.3	-11.5	-11.4	-8.8	-6.1	-4.5
0.	-3.5	-2.9	-5.0	-2.8	-2.3	-0.1	1.0
15.	1.8	3.1	3.4	2.5	2.5	4.9	5.4
30.	4.1	6.6	-3.4	0.4	4.5	7.1	7.4
45.	6.7	1.3	-2.3	2.1	6.7	6.9	7.3
60.	1.2	5.4	17.4	13.5	-1.6	6.6	-8.2

Table A5 Error estimation for the angular offset

Relative error in percent for one degree off in yaw angle

yaw angle	velocity components		
	U	V	W
-60.0	-0.97	0.36	-3.04
-45.0	-0.46	-3.97	-1.76
-30.0	-0.01	-2.60	-1.02
-15.0	0.43	-1.62	-0.48
0.0	0.94	-0.97	-0.02
15.0	1.60	-0.46	0.45
30.0	2.58	-0.01	0.99
45.0	4.05	0.43	1.73
60.0	0.36	0.94	3.01

Relative error in percent for one degree off in roll angle

yaw angle	velocity components		
	U	V	W
-60.0	0.00	0.36	0.09
-45.0	0.00	0.13	0.03
-30.0	0.00	0.04	0.01
-15.0	0.00	0.01	0.00
0.0	0.00	0.00	0.00
15.0	0.01	0.00	0.00
30.0	0.04	0.00	0.01
45.0	0.13	0.00	0.03
60.0	0.36	0.00	0.09

Vita

The author was born on February 20, 1963 in Taiwan R.O.C. He earned his B.S. degree in Naval Architecture Engineering from National Taiwan University, Taipei, Taiwan R.O.C. in June 1985. Upon graduation, he joined the ROC Navy for two years service. After discharging from the Navy, he worked as a research assistant in the Department of Naval Architecture National Taiwan University until he joined the Aerospace and Ocean Engineering Department, VPI & SU in 1988.